Master's thesis

NTNU
Norwegian University of Science and Technology
Faculty of Information Technology and Electrical Engineering
Department of Mathematical Sciences

Hans Julian Halvorsen

Reduced Order Modelling of Component Based Analysis for Stokes Flow

Master's thesis in Physics and Mathematics
Supervisor: Trond Kvamsdal
August 2021

NTNU
Norwegian University of
Science and Technology

Hans Julian Halvorsen

Reduced Order Modelling of Component Based Analysis for Stokes Flow

Master's thesis in Physics and Mathematics
Supervisor: Trond Kvamsdal
August 2021

Norwegian University of Science and Technology
Faculty of Information Technology and Electrical Engineering
Department of Mathematical Sciences

NTNU
Norwegian University of
Science and Technology

Abstract

A parameter dependent version of the Stokes Partial Differential Equation (PDE) is considered, with the goal of modelling flow in arbitrary pipe systems. The pipe systems are created from sub-domains called components or archetypes. The Stokes equation is solved locally on each archetype using a Mixed Finite Element Method (FEM) with quadrilateral Taylor-Hood elements, and the Galerkin Reduced Basis (RB) method is used with the Proper Orthogonal Decomposition (POD) algorithm to create a Reduced Order Model (ROM) for each archetype. The ROM approach reduces the complexity of the linear system governing each archetype from $\sim 10^4$ degrees of freedom (dofs) to ~ 50 dofs, thus the linear system can be solved for any new choice of parameters in real-time, with minimal loss of accuracy ($\sim 10^{-3}$ measured in both the L^2 norm and the H^1 semi-norm). When connecting two archetypes, a least-squares fit is performed on the solution at the outlet boundary nodes of the first archetype, and used as a lifting function for the following archetype inlet boundary. The pressure of the preceding archetype is shifted to match the pressure at the inlet of the following archetype.

The approach is found to be very effective when considering complex pipe systems, with the relative change in volume flow from the first inlet to the final outlet staying below 10^{-3}, even with systems consisting of up to 30 components. The full system is usually solved in ~ 1 second, where an equivalent Full Order Model (FOM) would have more than 10^5 dofs. Especially constructing new complex systems is shown to be very efficient, as it only requires one to specify what components to use and the parameter values for those components.

One limitation of this approach is also discovered. When dealing with bifurcating pipes, there is no way to retroactively change the pressure gradient of the previous archetype, resulting in incorrect flow rates following the bifurcations. Thus this approach is limited to single-outlet systems. `Click this link` to access the code.

Sammendrag

En parameteravhengig versjon av Stokes Partielle Differensialligning (PDE) undersøkes, med et mål om å modellere flyt i et villkårlig rørsystem. Rørsystemet bygges opp av subdomener kalt komponenter eller erketyper. Stokes ligning løses lokalt på hver erketype ved bruk av en Blandet Endelige Elementers Metode (FEM) med firkantede Taylor-Hood elementer, og Galerkins Reduserte Basis (RB) metode benyttes sammen med en algoritme for Ekte Ortogonal Dekomposisjon (POD) for å lage en Redusert Ordens Modell (ROM) for hver erketype. Bruken av ROM reduserer kompleksiteten til det lineære ligningssystemet som gjelder for hver erketype fra $\sim 10^4$ frihetsgrader (dofs) til ~ 50 dofs, hvilket gjør at det lineære ligningssystemet kan løses for alle nye valg av parametere i sanntid, med minimalt tap av nøyaktighet ($\sim 10^{-3}$ målt i både L^2 norm og H^1 semi-norm). Når to erketyper sammenkobles, gjøres en minste-kvadrats tilpasning på løsningen i rand-nodene ved utløpet til den første erketypen, som igjen benyttes som løfte-funksjon for den etterfølgende erketypens innløpsrand. Trykket i den første erketypen løftes slik at det sammenfaller med trykket ved innløpet til den etterfølgende erketypen.

Denne fremgangsmåten viser seg å være veldig effektiv når komplekse rørsystem undersøkes, med en relativ endring i volumstrøm fra første innløp til siste utløp på under 10^{-3}, selv i systemer konstruert fra opp til 30 komponenter. Det fulle systemet lar seg typisk løse på ~ 1 sekund, hvor en ekvivalent Full Ordens Modell (FOM) ville hatt over 10^5 dofs. Særlig det å konstruere nye komplekse systemer viser seg å være veldig effektivt, da det kun krever at en spesifiserer hvilke komponenter som skal brukes og parameterverdiene for disse komponentene.

En begrensning med denne fremgangsmåten blir også oppdaget. Når en benytter forgrenende rør, så er det ingen mulighet for å retroaktivt endre trykkgradienten til den foregående erketypen, noe som resulterer i uriktige flyt-rater etter forgreningen. Dermed er fremgangsmåten begrenset til rørsystemer med ett utløp. `Trykk på denne lenken` for å få tilgang til all kode.

Acknowledgements

This thesis was written at a time when the entire world was in lockdown, making it an even lonelier process than normally. Thus I would like to thank all those who've kept me sane through these trying times, both online and in real life.

I want to thank my girlfriend Anna for motivating me and pushing me through the tougher days. We've spent way more time at home together than either of us could have imagined last year, and I applaud you for keeping up with me through my lockdown-tantrums. Writing this thesis would have been a lot harder without you.

I would also like to thank my supervisor, Professor Trond Kvamsdal, who has guided me through both the specialization project and this Master's thesis. His genuine excitement for this subject has inspired me, and I strongly appreciate his ability to educate and convey information. He has patiently followed my progress, and encouraged me every step of the way.

Thank you to Abdullah Abdulhaque and Vasileios Tsiolakis both for helping me when i was stuck in a well of numerical bugs, your combined efforts helped me realise my missteps and guided me back on to the bug-free path.

A special thanks goes to Vegard Gjerde Buset, whom I've been working closely with on most major projects through my time at NTNU. He works with unparalleled tempo; Some would say he's the Warholm of productivity. Thank you for everything!

In addition, I would like to thank Vegard Kolaas for all the interesting discussions and for spurring my interest in chess. Thank you to my closest friends Jesper, Emil, and Ole for your support and for keeping me entertained, you're all absolute mad-lads.

Last but not least, I am grateful to my mother Liv, my father Knut, and my sister Lisa for giving me an exceptional upbringing. I would not be where I am today without all of you.

Contents

Acronyms

dofs degrees of freedom. 1, 8, 22, 76

FE Finite Element. 13

FEM Finite Element Method. 1, 9, 10, 13

FOM Full Order Model. 1, 8, 9, 16, 17, 26, 27, 39, 41, 42, 44, 45, 48, 49, 51, 52, 54, 55, 57, 58, 60, 62–69, 76

LBB Ladyzhenskaia-Babuška-Brezzi. 9, 22, 26

PCA Principal Component Analysis. 16

PDE Partial Differential Equation. 1, 8, 9, 11, 15

POD Proper Orthogonal Decomposition. 1, 8, 9, 16, 17, 27, 39, 41, 44, 48, 51, 54, 57, 60–62, 68, 69

RB Reduced Basis. 1, 5, 9, 16, 17, 27, 61

ROM Reduced Order Model. 1, 8, 9, 17, 26, 39–69, 76

SVD Singular Value Decomposition. 16, 27

Nomenclature

$(\boldsymbol{u}, p)$ The solution pair: Velocity and pressure

$3 \cdot N_r$ The dimension of the RB space

$[B_x, B_y]$ The divergence matrix of dimension $N_p \times (2 \cdot N_u)$, constructed from the bilinear forms $b_x(\cdot,\cdot).b_y(\cdot,\cdot)$

$\bar{\Omega}$ The closure of Ω, that is $\bar{\Omega}_i = \Omega_i \cup \Gamma_{i,I} \cup \Gamma_{i,W} \cup \Gamma_{i,O}$

$\boldsymbol{\Phi}_{\Omega_i}(x, y, \boldsymbol{\mu}_i)$ The parametric map from the initial geometrical configuration archetype i to geometrically altered archetype i

$\boldsymbol{g}$ The function describing the boundary datum, $\boldsymbol{g} = [g_x, g_y]^T$

$\boldsymbol{J_\Phi}$ The Jacobian of the parametric map $\boldsymbol{\Phi}_{\Omega_i}(x, y, \boldsymbol{\mu}_i)$

$\boldsymbol{n}$ The outwards-pointing normal vector

$\boldsymbol{p}_h$ The high-fidelity discrete approximation to the velocity

$\boldsymbol{p}_r$ The reduced order discrete approximation to the pressure

$\boldsymbol{u}_{x,h}$ The high-fidelity discrete approximation to the x-velocity

$\boldsymbol{u}_{x,r}$ The reduced order discrete approximation to the x-velocity

$\boldsymbol{u}_{y,h}$ The high-fidelity discrete approximation to the y-velocity

$\boldsymbol{u}_{y,r}$ The reduced order discrete approximation to the y-velocity

Δ The Laplace operator, $\Delta = \frac{\partial^2}{\partial x_1^2} + \cdots + \frac{\partial^2}{\partial x_n^2}$

δ_{ij} The Kronecker delta

$\frac{\partial}{\partial x_i}$ The partial differential operator

$\Gamma_{j,\mathrm{I}}$ The inlet boundary of archetype j. Non-homogeneous Dirichlet

$\Gamma_{j,\mathrm{O}}$ The outlet boundary of archetype j. Homogeneous Neumann

$\Gamma_{j,\mathrm{W}}$ The walls boundary of archetype j. Homogeneous Dirichlet

$\gamma_{x,q}(\boldsymbol{\mu})$ The affine function of $b_{x,q}(\cdot,\cdot)$

$\gamma_{y,q}(\boldsymbol{\mu})$ The affine function of $b_{y,q}(\cdot,\cdot)$

$\mathcal{M}_h$ The set of all high-fidelity solutions

$\mathcal{P}$ The set of all possible input parameters

$\mathcal{Q}$ The pressure space, $\mathcal{Q} = L^2(\Omega)$

$\mathcal{Q}_h$ A finite-dimensional subspace of $\mathcal{Q}$

$\mathcal{T}_h$ The partition of $\mathcal{V}_h$

$\mathcal{V}$ The velocity space, $\mathcal{V} = [H^1_{\Gamma_D}(\Omega)]^2$

$\mathcal{V}_h$ A finite-dimensional subspace of $\mathcal{V}$

$\boldsymbol{\mu}_i$ The parameter vector of archetype i

$\boldsymbol{\mu}_{\mathrm{g}}$ The geometric parameters in $\boldsymbol{\mu}_i$, that is the parameters that affect the geometry of archetype i

∇ The Nabla operator, $\nabla = [\frac{\partial}{\partial x_1}, \ldots, \frac{\partial}{\partial x_n}]^T$

Ω_i The domain of archetype i

ψ_i One of the right-singular vectors of the snapshot matrix

ψ_i The i-th basis function of the space $\mathcal{V}_h$

$\mathbb{R}$ The real numbers

σ_i One of the singular values of the snapshot matrix

σ_i^2 One of the eigenvalues of the correlation matrix

$\theta_q(\boldsymbol{\mu})$ The affine function of $a_q(\cdot,\cdot)$

$\varepsilon_{\mathrm{POD}}$ The tolerance for the error of the reduced basis solution

φ_i The i-th basis function of the space $\mathcal{Q}_h$

ζ_i One of the left-singular vectors of the snapshot matrix

A The stiffness matrix of dimension $N_u \times N_u$, constructed from the bilinear from $a(\cdot,\cdot)$

$a(\cdot,\cdot)$ One of the bilinear forms of the Galerkin formulation

$a_q(\cdot,\cdot)$ the q-th integral of the bilinear form $a(\cdot,\cdot)$

$b_x(\cdot,\cdot)$ One of the bilinear forms of the Galerkin formulation

$b_y(\cdot,\cdot)$ One of the bilinear forms of the Galerkin formulation

$b_{x,q}(\cdot,\cdot)$ the q-th integral of the bilinear form $b_x(\cdot,\cdot)$

$b_{y,q}(\cdot,\cdot)$ the q-th integral of the bilinear form $b_y(\cdot,\cdot)$

C The correlation matrix

f The function describing the source term

K The total number of elements, the cardinality of $\mathcal{T}_h$

L^p The Lebesgue space of order p

N_n The number of snapshots/solutions chosen from $\mathcal{M}_h$

N_p The dimension of the space $\mathcal{Q}_h$

N_u The dimension of the space $\mathcal{V}_h$

q Any test function in $\mathcal{Q}$

Q_2/Q_1 The quadrilateral Taylor-Hood element with a biquadratic velocity basis and a bilinear pressure basis

Q_a The number of integrals making up the bilinear form $a(\cdot,\cdot)$

Q_b The number of integrals making up the bilinear form $b(\cdot,\cdot)$

q_h Any test function in $\mathcal{Q}_h$

r_{gx} The x-component of the lifting function, $r_{gx} = \mu_a g_x(\boldsymbol{\mu}_g)$ on Γ_I, 0 else

r_{gy} The y-component of the lifting function, $r_{gy} = \mu_a g_y(\boldsymbol{\mu}_g)$ on Γ_I, 0 else

$S = U\Sigma Z^T$ The Singular Value Decomposition of the snapshot matrix

S The snapshot matrix of dimension $N_h \times N_n$

v Any test function in $\mathcal{V}$

v_h Any test function in $\mathcal{V}_h$

$W^{1,2} = H^1 = \mathcal{V}$ The Sobolev space of interest

1 Introduction

The use of computer simulations in the early stages of engineering projects is by 2021 the standard in almost any project. It saves plenty of resources to first construct a digital model before developing any prototypes. However, especially in large-scale projects, constructing these digital models can be very time-consuming [1]. First it is necessary to create a discrete representation of the desired system, which also captures its essential properties. This requires one to create gigantic meshes, which is then used to approximate the behaviour of the system according to either one or several governing partial differential equations (PDEs) [2]. To obtain accurate approximations, one needs to solve a large system of equations, typically with millions of degrees of freedom (dofs). In addition, these problems typically depend on several different parameters, such as heat conductivity, pressure, the geometrical structures of the system, and so forth. Naively one would have to re-solve the problem every time a parameter is changed, or even reconstruct the entire mesh if the parameter affects the geometry of the system.

This is where the concept of Reduced Order Modelling (ROM) comes into play. The idea is to reduce the complexity of the Full Order Model (FOM) such that for any new parameter value, the problem can be solved much more efficiently with a only a slight decrease in accuracy. Essentially the system of equations is rewritten in such a way that it only depends affinely on the parameters, as well as reducing the complexity of the system with techniques such as Proper Orthogonal Decomposition (POD). This ensures minimal loss of accuracy, and enables the user to solve the reduced system in real-time for any new choice of parameters.

Since ROM enables the user to solve complex parameter-dependent PDEs in real-time, the method is utilized in a variety of problems, such as PDE-constrained optimization, optimal control problems, and inverse problems [3]. Such problems arise in (but not limited to) fluid mechanics [2], neuroscience [4], renewable energy [5], neural networks [6] [7], chemical engineering [8], and digital twins [9]. In this thesis we will focus on the use of ROM in the field of digital twins.

A digital twin is in many ways similar to the digital models used in prototype development. But unlike a digital prototype, the purpose of a digital twin is to monitor and control the behaviour of the asset or system it represents in real-time. There are mainly two types of digital twins: physics-based and data-driven [10]. However the two can also be combined in many different ways, commonly referred to as a hybrid twin [11]. In a data-driven twin, different sensors capture changes in the real world system, and the digital twin is updated accordingly. If the digital twin is physics-based, it is governed by one or several parameter-dependent PDEs, and the digital twin can be controlled by changing these parameters. In this thesis we will focus on a purely physics-based twin.

One of the main advantages of a digital twin compared to similar monitoring systems is its adaptability. Consider a situation where multiple similar assets needs monitoring. Even if the assets initially are almost identical from a manufacturing point of view, the wear and tear of time will require all sorts of repairs and component changes. A single static monitoring system will fail to capture the unique changes in the properties of each asset, resulting in sub-optimal control of the assets. However with a digital twin system, the unique changes in each asset could be accounted for, ensuring optimal control of each asset.

There are however some challenges that comes with the use of a digital twin [12]. Maintaining the digital twin of just one asset can be comprehensive, where for example extensive structural damage or changes in the asset could require one to rebuild the entire mesh. This may prove to be too time-consuming in larger systems with hundreds of physical assets [13]. To simplify the management of all the unique digital twins, a component-based approach can be used. Instead of representing each asset as one unique complete model, each model is constructed from a library of components called archetype components. Each archetype component can be altered by adjusting several local parameters, to change its geometrical shape and inherent properties.

For each archetype, a ROM is created, and thus the governing PDEs can be solved locally on each archetype in real-time given any choice of parameters. Thus, if a part of the real asset gets damaged or replaced, one would simply update or replace the corresponding archetype component on the digital twin. Essentially each digital twin is constructed as a combination of flexible LEGO-blocks.

In this paper we will investigate the use of component-based ROM to construct arbitrary systems of pipelines, where the pipe-flow is governed by the Stokes-equation [14] [15] [16] [17]. To construct the ROMs, the Galerkin Reduced Basis (RB) method will be used. This involves computing a number of high-fidelity approximations for a small set of possible parameter values using the FOM, called snapshots. These snapshots are then used to create a much less complex model, the ROM, while still maintaining high accuracy.

Following the introduction, the second section provides a brief introduction to the most essential underlying mathematical concepts. Using the Poisson equation as an example, we introduce the weak formulation, the Lax-Milgram Theorem for uniqueness and stability, and the Finite Element Method (FEM). We then show how to create a ROM using the Galerkin RB method and the Proper Orthogonal Decomposition (POD) algorithm.

In the third section we introduce the problem at hand. We show how the Stokes equation relates to the Navier-Stokes equation, and obtain the weak formulation of our specific problem. We then introduce the Taylor-Hood element, a special class of elements well suited for mixed FEM problems. After defining the basis functions and presenting the Gaussian quadrature used for numerical integration, we utilise theory and concepts from Section 2 to discretize the equation. The uniqueness and stability of the resulting linear system is discussed, and the Ladyzhenskaia-Babuška-Brezzi (LBB) inf-sup condition is introduced. Finally we reduce the linear system and obtain the ROM.

All the archetypes are presented in the fourth Section, along with their parameters, lifting functions, affine functions and bilinear forms. Our approach for connecting the archetypes are discussed in Section 5, before we present the results and some noteworthy observations in Section 6.

2 Underlying mathematical concepts

The construction of a digital twin relies on several mathematical concepts. The physics of the model are based on solving discretized PDEs; we assume that the reader has a conceptual understanding of said PDEs. In the first subsection we introduce some important definitions from functional analysis, which are used frequently throughout this paper. In the second subsection we introduce the most common approach for discretizing PDE's, the Finite Element Method (FEM). The method is explained by using the rather trivial Poisson equation as an example. In the final subsection we introduce the Galerkin Reduced Basis (RB) method and show how to construct the ROM from the FOM using Proper Orthogonal Decomposition (POD).

2.1 Function spaces

In this section we will introduce some useful concepts from functional analysis. This is necessary to understand the techniques used in the FEM.

For convenience sake, we will only consider the real numbers. Let Ω be our domain of interest, $\Omega \subset \mathbb{R}^n$. A function $u : \Omega \mapsto \mathbb{R}$ is defined to be integrable if its integral converges absolutely, i.e.

$$\int_\Omega |u| \, d\Omega < \infty. \tag{2.1}$$

For $p \geq 1$, define the space of p-integrable functions as

$$L^p(\Omega) := \Big\{ u : \Omega \mapsto \mathbb{R}; \int_\Omega |u|^p \, d\Omega < \infty \Big\}, \tag{2.2}$$

i.e. the space of all functions that maps from Ω to $\mathbb{R}$ given that the integral of its p-th power converges absolutely [18]. It can be proven that L^p is a complete space for each $p \in [1, \infty]$ [19]. In the special case where $p = 2$, $L^2(\Omega)$ is associated with an inner-product and the induced norm

$$\langle u, v \rangle_{L_2} = \int_\Omega uv \, d\Omega, \quad ||u||_{L^2} = \langle u, u \rangle_{L^2}^{1/2} = \Big(\int_\Omega u^2 \, d\Omega \Big)^{1/2}. \tag{2.3}$$

$L^2(\Omega)$ is thus a complete inner product space, also known as a Hilbert space. It can be shown that it is also the only Hilbert space among all the L^p-spaces [20]. From this we can define the Sobolev space $W^{k,p}(\Omega)$, with $p = 2$:

$$W^{k,2}(\Omega) := \Big\{ u \in L^2(\Omega); D^\alpha u \in L^2(\Omega), \forall |\alpha| \leq k \Big\}, \quad D^\alpha u = \frac{\partial^{|\alpha|} u}{\partial x_1^{\alpha_1} \dots \partial x_n^{\alpha_n}}, \quad |\alpha| = \sum_{i=1}^{n} \alpha_i, \tag{2.4}$$

i.e. one requires that all partial derivatives of u up to order k is p-integrable. For $p = 2$, the notation $W^{k,2} = H^k$ will be used. In the problem considered later in this thesis, only first-order derivatives are needed, that is $k = 1$:

$$W^{1,2}(\Omega) = H^1(\Omega) := \Big\{ u \in L^2(\Omega); \nabla u \in L^2(\Omega) \Big\}. \tag{2.5}$$

This is indeed also a Hilbert space, with the inner-product and norm

$$\langle u, v \rangle_{H^1} = \int_\Omega uv + \nabla u \nabla v \, d\Omega, \quad ||u||_{H^1} = \langle u, u \rangle_{H^1}^{1/2} = \Big(\int_\Omega u^2 \, d\Omega + \int_\Omega |\nabla u|^2 \, d\Omega \Big)^{1/2} = \big(||u||_{L^2}^2 + |u|_{H^1}^2 \big)^{1/2}, \tag{2.6}$$

where $|u|_{H^1}$ is known as the H^1 *semi-norm*. Finally, let Γ_D be the part of the boundary of Ω with Dirichlet boundary conditions, i.e. $u|_{\Gamma_D} = g$, where g is some function or constant describing the Dirichlet boundary condition. Define $H^1_{\Gamma_D}(\Omega)$ as

$$H^1_{\Gamma_D}(\Omega) := \Big\{ u \in H^1(\Omega); u|_{\Gamma_D} = g \Big\}, \tag{2.7}$$

that is the space of functions in H^1 with known values on the Dirichlet part of the boundary. $H^1(\Omega)$ and $L^2(\Omega)$ are the spaces of interest throughout the rest of this thesis.

2.2 Finite Elements, the Galerkin projection

In this section we will give a summary on the basics of the FEM; see [21] and [22] for a much more thorough introduction.

2.2.1 Weak formulation

Let $u \in \mathcal{V} = H^1_{\Gamma_D}$, with $H^1_{\Gamma_D}$ as defined in the previous section. Consider a rather simple example, the Poisson equation with homogeneous Dirichlet boundary conditions (that is $g = 0, u|_{\Gamma_D} = 0$):

$$\begin{cases} -\Delta u = f & \text{in } \Omega, \\ u = 0 & \text{on } \Gamma_D. \end{cases} \tag{2.8}$$

First one must obtain the variational formulation of the equation. This is done by multiplying the equation with a test function $v \in \mathcal{V}$, and integrating over the domain [23].

$$-\int_\Omega \Delta u v \, d\Omega = \int_\Omega f v \, d\Omega. \tag{2.9}$$

The resulting equation can then be simplified by applying Greens first identity:

$$-\int_\Omega \Delta u v \, d\Omega = \int_\Omega \nabla u \nabla v \, d\Omega - \int_{\Gamma_D} (\nabla u \cdot \boldsymbol{n}) v \, d\Gamma_D = \int_\Omega f v \, d\Omega. \tag{2.10}$$

For $v \in \mathcal{V}$, $v = 0$ on Γ_D, and the boundary integral disappears. Thus one is left with

$$\int_\Omega \nabla u \nabla v \, d\Omega = \int_\Omega f v \, d\Omega. \tag{2.11}$$

The resulting equation is known as the weak formulation of the PDE:

$$\begin{aligned} &\text{Find } u \in \mathcal{V}, \text{ such that } a(u,v) = f(v) \quad \forall v \in \mathcal{V}, \text{ where} \\ &a(u,v) = \int_\Omega \nabla u \nabla v \, d\Omega = \int_\Omega f v \, d\Omega = f(v). \end{aligned} \tag{2.12}$$

2.2.2 Uniqueness and stability

Before we look for the solution of the weak form obtained above, we want to know if the solution (if it exists) is unique, and if the solution depends continuously on the data ($f(v)$). For strongly coercive problems such as the Poisson equation, the Lax-Milgram theorem is sufficient to prove both of these properties:

Theorem 2.1 (Lax-Milgram Theorem)**.** *Let $\mathcal{V}$ be a Hilbert space and $a(\cdot,\cdot)$ a bilinear form on $\mathcal{V}$, which is*

- ***Boundedness:*** $|a(u,v)| \leq C\|u\|_{\mathcal{V}}\|v\|_{\mathcal{V}}, \quad \forall u, v \in \mathcal{V}.$
- ***Coercivity:*** $a(u,u) \geq c\|u\|^2_{\mathcal{V}}, \quad \forall u \in \mathcal{V}.$

Then, for any $f \in \mathcal{V}'$, there is a unique solution $u \in \mathcal{V}$ to the equation

$a(u,v) = f(v), \quad \forall v \in \mathcal{V},$

which satisfies the stability estimate

$\|u\|_{\mathcal{V}} \leq \frac{1}{c}\|f\|_{\mathcal{V}'}.$

We will now use the variational formulation found above and Theorem 2.1 to prove the uniqueness of the solution to the Poisson equation, while simultaneously obtaining an estimate for the stability of the solution.

Proof. We first consider the boundedness of the Poisson equation. Using the Cauchy-Schwarz inequality, we obtain

$$|a(u,v)| = \int_\Omega \nabla u \nabla v d\Omega \leq \|\nabla u\|_{L^2}\|\nabla v\|_{L^2}. \tag{2.13}$$

Note that

$$\|u\|^2_{H^1} = \|u\|^2_{\mathcal{V}} = \|u\|^2_{L^2} + \|\nabla u\|^2_{L^2} \Rightarrow \|u\|^2_{\mathcal{V}} \geq \|\nabla u\|^2_{L^2}, \tag{2.14}$$

thus

$$|a(u,v)| \leq \|\nabla u\|_{L^2}\|\nabla v\|_{L^2} \leq \|u\|_{\mathcal{V}}\|v\|_{\mathcal{V}}. \tag{2.15}$$

Thus the Poisson equation is bounded. To show coercivity, we write the norm as a sum of two halves, and use the Poincaré inequality:

$$a(v,v) = \int_\Omega |\nabla v|^2 d\Omega = \|\nabla v\|_{L^2}^2 = \frac{1}{2}\|\nabla v\|_{L^2}^2 + \frac{1}{2}\|\nabla v\|_{L^2}^2 \geq \frac{1}{2C^2}\|v\|_{L^2}^2 + \frac{1}{2}\|\nabla v\|_{L^2}^2. \tag{2.16}$$

Now let $\beta = \min\{\frac{1}{2C^2}, \frac{1}{2}\}$. Then

$$a(v,v) \geq \frac{1}{2C^2}\|v\|_{L^2}^2 + \frac{1}{2}\|\nabla v\|_{L^2}^2 \geq \beta\Big(\|v\|_{L^2}^2 + \|\nabla v\|_{L^2}^2\Big) = \beta\|v\|_{H^1}^2 = \beta\|v\|_{\mathcal{V}}^2. \tag{2.17}$$

Thus by Theorem 2.1, there exists a unique solution $u \in \mathcal{V}$ to the Poisson equation , that also satisfies the stability estimate

$$\|u\|_{\mathcal{V}} \leq \frac{1}{\beta}\|f\|_{\mathcal{V}'}. \tag{2.18}$$

□

2.2.3 The Galerkin projection

With the weak formulation as above, the next goal is to discretize the domain in question so that u can be approximated as the solution of a linear system. This is done by considering a discrete subspace of $\mathcal{V}$, that is $\mathcal{V}_h \subset \mathcal{V}$. This gives us the Galerkin equation, or the Galerkin formulation:

$$\text{Find } u_h \in \mathcal{V}_h, \text{ such that } a(u_h, v_h) = f(v_h) \quad \forall v_h \in \mathcal{V}_h. \tag{2.19}$$

Since the functions u_h, v_h now are members of the finite dimensional space $\mathcal{V}_h$, they can be expressed as linear combinations of some basis for said space:

$$u_h = \sum_{j=1}^{N_h} u_h^{(j)}\varphi_j, \quad v_h \sum_{i=1}^{N_h} v_h^{(i)}\varphi_i, \tag{2.20}$$

where $\text{span}(\varphi_i)_{i=1}^{N_h} = \mathcal{V}_h$, $\dim(\mathcal{V}_h) = N_h$. Inserted into the Galerkin formulation we get

$$a(u_h, v_h) = \sum_{j=1}^{N_h}\sum_{i=1}^{N_h} u_h^{(j)} v_h^{(i)} a(\varphi_j, \varphi_i) = f(v_h) = \sum_{i=1}^{N_h} v_h^{(i)} f(\varphi_i), \tag{2.21}$$

which can be rewritten as a linear system of equations:

$$\boldsymbol{v}_h^T A_h \boldsymbol{u}_h = \boldsymbol{v}_h^T \boldsymbol{f}_h, \quad (A_h)_{i,j} = a(\varphi_j, \varphi_i), \quad (\boldsymbol{f}_h)_i = f(\varphi_i). \tag{2.22}$$

The Galerkin formulation requires this to hold for all $v_h \in \mathcal{V}_h$, which implies that

$$A_h \boldsymbol{u}_h = \boldsymbol{f}_h. \tag{2.23}$$

The matrix A_h is typically referred to as the *stiffness matrix*, and its construction, as well as the construction of $\boldsymbol{f}_h$, is discussed in the upcoming section.

2.2.4 The Finite Elements method

The FEM is a process for constructing discrete subspaces such as $\mathcal{V}_h$. These are referred to as Finite Element (FE) spaces. The construction of such space is characterized by three basic aspects, known as (FEM 1), (FEM 2), and (FEM 3) [24] [22].

(FEM 1) *A partition $\mathcal{T}_h$, with $|\mathcal{T}_h| = K$ (the cardinality of $\mathcal{T}_h$ is K), is established over the set $\bar{\Omega}$, i.e. the set $\bar{\Omega}$ (the closure of Ω) is divided into K subsets, called finite elements, E_l, in such a way that the following properties are satisfied* [24]:

(i) $\bigcup_{l=1}^{K} E_l = \bar{\Omega}$.

(ii) For each $E_l \in \mathcal{T}_h$ the set E_l is closed and the interior $\dot{E}_l$ is non-empty.

(iii) For each distinct $E_l, E_m \in \mathcal{T}_h$, the intersection of their interior is empty, $\dot{E}_l \cap \dot{E}_m = \emptyset$.

(iv) For each $E_l \in \mathcal{T}_h$, the boundary ∂E_l is Lipschitz-continuous.

(FEM 2) *Let $\mathcal{P}$ be a finite-dimensional space of functions (typically polynomials) on $\mathcal{T}_h$ (the space of shape functions). This is key to the convergence of the method, as well as it simplifies the construction of the linear system* [24].

(FEM 3) *Finally, let $\mathcal{N}$ be a canonical basis for $\mathcal{P}'$, whose corresponding basis functions have "small" support, and which are easily described* [24].

Then $(\mathcal{T}_h, \mathcal{P}, \mathcal{N})$ is called a finite element. The importance of these three basis aspects will become apparent in the following example problem. Let's once again consider the Poisson equation. Let $\Omega \subset \mathbb{R}^2$, and let it be divided into K elements E_l, so that $\bigcup_{l=1}^{K} E_l = \bar{\Omega}$. Consider for the sake of simplicity the elements to be triangular, with bilinear basis functions (later in this paper we use the Q_2/Q_1 Taylor-Hood element, a quadrilateral element with biquadratic and bilinear basis functions). To each element we associate three nodes, one in every corner of the element: $(x_i, y_i), (x_j, y_j), (x_k, y_k)$. To each node we associate one basis function $\varphi_i(x_m, y_m) = \delta_{im}$, where δ_{im} is the Kronecker delta:

$$\delta_{im} = \begin{cases} 1 & \text{if } m = i, \\ 0 & \text{if } m \neq i. \end{cases} \tag{2.24}$$

This also ensures that the basis functions have compact support. With bilinear basis functions, the basis functions vary linearly between 1 and 0 with respect to each variable, $\varphi_i(x, y) = C^i + C^i_x x + C^i_y y$. The coefficients of the basis functions can then be determined by solving the linear system

$$\begin{bmatrix} 1 & x_i & y_i \\ 1 & x_j & y_j \\ 1 & x_k & y_k \end{bmatrix} \begin{bmatrix} C^i \\ C^i_x \\ C^i_y \end{bmatrix} = \begin{bmatrix} 1 \\ 0 \\ 0 \end{bmatrix},$$

and similarly for j and k, replacing the right hand side with $[0, 1, 0]^T$, $[0, 0, 1]^T$ respectively. Thus $a(\varphi_l, \varphi_m)$ can be calculated for all nine pairs $l, m = i, j, k$, and added to $(A_h)_{l,m}$. This is then repeated for all of the K elements. For the Poisson equation we get

$$a(\varphi_l, \varphi_m) = \int_E \nabla\varphi_l \nabla\varphi_m \, dE = \int_E C^l_x C^m_x + C^l_y C^m_y \, dE = (C^l_x C^m_x + C^l_y C^m_y)\text{Area}(E), \quad l, m = i, j, k. \tag{2.25}$$

A similar procedure is used for constructing $\boldsymbol{f}_h$. Every element adds three contributions to $\boldsymbol{f}_h$, one for each node. In the Poisson example we get

$$f(\varphi_m) = \int_E f\varphi_m \, dE = \int_E f(C^m + C_x^m x + C_y^m y) \, dE, \quad m = i, j, k. \tag{2.26}$$

In this simple case there are only constant terms in the integrand of $a(\varphi_l, \varphi_m)$, making the solution easy to compute analytically. When this is not the case, as with $f(\varphi_m)$, the integral can be solved with some numerical integration method. After the assembly of A_h and $\boldsymbol{f}_h$, the system can be solved directly with any solver.

2.3 Galerkin Reduced Basis method

Let us now consider some arbitrary second order PDE, with parametric dependence. Let $\boldsymbol{\mu}$ be the *input-parameter* vector, and $\mathcal{P}$ be the set of all possible input parameters, so that $\boldsymbol{\mu} \in \mathcal{P}$ [3]. The problem can be solved in the same manner as in the previous section, although this is highly unpreferable. If one of the parameters is changed, it would affect the stiffness matrix which would have to be recalculated. The domain Ω could also depend on any number of parameters, and changing one of these would require one to redo the entire procedure from scratch.

2.3.1 Affine parametric dependence

Denote by $\tilde{\Omega}(\boldsymbol{\mu}_{\mathrm{g}})$ a domain with parametric dependence, with $\boldsymbol{\mu}_{\mathrm{g}}$ as a vector of geometrical parameters. It is then convenient to reformulate and solve the PDE on some reference domain which is independent of $\boldsymbol{\mu}_{\mathrm{g}}$. The solution can then be mapped back to the original domain after it is found [25].

Let $\Omega = \tilde{\Omega}(\boldsymbol{\mu}_{\mathrm{g}}^{\mathrm{ref}})$ be the reference domain, with $\boldsymbol{\mu}_{\mathrm{g}}^{\mathrm{ref}}$ as some fixed reference parameters. Assume also that the PDE have been reformulated to match the reference domain. Then we can find the weak formulation of the PDE in a very similar manner as in Section 2.2.1. Let $\mathcal{V}(\Omega)$ be some suitable Hilbert space (typically $\mathcal{V}(\Omega) = H^1_{\Gamma_D}(\Omega)$ is sufficient). Let $u(\boldsymbol{\mu}), v \in \mathcal{V}$ be the parameter-dependent function of interest, and some test function. Then the weak formulation reads:

$$\begin{aligned} &\text{Given } \boldsymbol{\mu} \in \mathcal{P}, \text{ Find } u(\boldsymbol{\mu}) \in \mathcal{V}, \text{ such that} \\ &a(u(\boldsymbol{\mu}), v; \boldsymbol{\mu}) = f(v; \boldsymbol{\mu}) \quad \forall v \in \mathcal{V}, \end{aligned} \tag{2.27}$$

where $a(\cdot, \cdot; \boldsymbol{\mu})$ is called the *parametrized* bilinear form, and $f(\cdot; \boldsymbol{\mu})$ the parametrized linear form. Following the procedure in Section 2.2.2, we arrive at the linear system

$$A_h(\boldsymbol{\mu})\boldsymbol{u}_h(\boldsymbol{\mu}) = \boldsymbol{f}_h(\boldsymbol{\mu}). \tag{2.28}$$

Note that both the stiffness matrix $A_h(\boldsymbol{\mu})$ and $\boldsymbol{f}_h(\boldsymbol{\mu})$ are parameter dependent, meaning they must be reconstructed for every new choice of $\boldsymbol{\mu}$. However, this can be avoided if one makes the *affine parametric dependence* assumption. That is, one assumes that $a(\cdot, \cdot; \boldsymbol{\mu}), f(\cdot; \boldsymbol{\mu})$ are affine, or separable, with respect to $\boldsymbol{\mu}$:

$$\begin{aligned} a(\cdot, \cdot; \boldsymbol{\mu}) &= \sum_{q=1}^{Q_a} \theta_q(\boldsymbol{\mu}) a_q(\cdot, \cdot), \\ f(\cdot; \boldsymbol{\mu}) &= \sum_{q=1}^{Q_f} \gamma_q(\boldsymbol{\mu}) f_q(\cdot). \end{aligned} \tag{2.29}$$

Here θ_q, γ_q are functions mapping from $\mathcal{P}$ to $\mathbb{R}$. The bilinear and linear forms are written as sums since they could consist of multiple integrals. If we now follow the procedure from Section 2.2.2, this property will carry over to the linear system.

$$\begin{aligned} A_h(\boldsymbol{\mu})\boldsymbol{u}_h(\boldsymbol{\mu}) &= \boldsymbol{f}_h(\boldsymbol{\mu}), \\ A_h(\boldsymbol{\mu}) &= \sum_{q=1}^{Q_a} \theta_q(\boldsymbol{\mu}) A_h^q, \\ \boldsymbol{f}_h(\boldsymbol{\mu}) &= \sum_{q=1}^{Q_f} \gamma_q(\boldsymbol{\mu}) \boldsymbol{f}_h^q. \end{aligned} \tag{2.30}$$

Thus, there is no longer a need to reconstruct the matrices and vectors A_h^q, f_h^q when changing parameters. Equation 2.30 is known as the FOM.

2.3.2 Reduced Basis methods

The the goal of any RB method is to exploit the $\boldsymbol{\mu}$-dependence of the solutions by projecting the problem onto a much smaller subspace $\mathcal{V}_r \subset \mathcal{V}_h$, $N_r \ll N_h$. In this paper we use Proper Orthogonal Decomposition (POD) to generate $\mathcal{V}_r$, a method known as Principal Component Analysis (PCA) in multivariate statistics [26] [27].

Let $\mathcal{M}_h$ be the set of all FOM solutions, that is

$$\mathcal{M}_h := \left\{ \boldsymbol{u}_h(\boldsymbol{\mu}) \in \mathcal{V}_h; \boldsymbol{\mu} \in \mathcal{P} \right\} \subset \mathcal{V}_h. \tag{2.31}$$

The idea is then that any $\boldsymbol{u}_h(\boldsymbol{\mu})$ can be approximated well with linear combinations of just a few elements in $\mathcal{M}_h$. This is done by first selecting a few elements from $\mathcal{M}_h$, that is $\{\boldsymbol{u}_h(\boldsymbol{\mu}^1), \dots, \boldsymbol{u}_h(\boldsymbol{\mu}^{N_n})\}$. These are known as snapshots. Here $\{\boldsymbol{\mu}^1, \dots, \boldsymbol{\mu}^{N_n}\} \subset \mathcal{P}$ is a small set of uniformly selected parameters, although these can be chosen in many different ways [28]. It is important to include the minimum and maximum value for each of the parameters in these snapshots to avoid extrapolation. The snapshots are then used to form a snapshot matrix, $S \in \mathbb{R}^{N_h \times N_n}$, and its Singular Value Decomposition (SVD) is computed [29]:

$$S = U \Sigma Z^T, \tag{2.32}$$

$$\begin{aligned} U &= \left[\boldsymbol{\zeta}_1 | \dots | \boldsymbol{\zeta}_{N_h} \right] \in \mathbb{R}^{N_h \times N_h}, \\ Z &= \left[\boldsymbol{\psi}_1 | \dots | \boldsymbol{\psi}_{N_n} \right] \in \mathbb{R}^{N_n \times N_n}, \\ \Sigma &= \operatorname{diag}(\sigma_1, \dots, \sigma_{N_n}) \in \mathbb{R}^{N_h \times N_n}, \end{aligned} \tag{2.33}$$

where $\boldsymbol{\zeta}_i$ are the left-singular vectors of S, $\boldsymbol{\psi}_i$ are the right-singular vectors of S, and σ_i are the singular values of S, $\sigma_1 \geq \dots \geq \sigma_{N_n}$. Note that both U and Z are orthonormal matrices. Then we can write

$$S\boldsymbol{\psi}_i = \sigma_i \boldsymbol{\zeta}_i \quad \text{and} \quad S^T \boldsymbol{\zeta}_i = \sigma_i \boldsymbol{\psi}_i \qquad i = 1, \dots, N_n, \tag{2.34}$$

or equivalently

$$S^T S \boldsymbol{\psi}_i = \sigma_i^2 \boldsymbol{\psi}_i \qquad i = 1, \dots, N_n. \tag{2.35}$$

Thus σ_i^2 is the eigenvalues of the matrix $S^T S$ in a non-increasing order. The matrix $C = S^T S$ is known as the *correlation matrix*. Note that the correlation matrix is equivalent to the discrete L^2 inner product of the snapshots, that is $(C)_{i,j} = \boldsymbol{u}_i^T \boldsymbol{u}_j$. One could consider using different inner products to define the correlation matrix, such as in [30]. The POD basis of any dimension $N \leq N_n$ is then defined as the first N left-singular vectors $\boldsymbol{\zeta}_1, \dots, \boldsymbol{\zeta}_N$ of S, or equivalently

$$\boldsymbol{\zeta}_j = \frac{1}{\sigma_j} S \boldsymbol{\psi}_j \qquad j = 1, \dots, N, \tag{2.36}$$

where $\boldsymbol{\psi}_j$ is the first N eigenvectors of the correlation matrix C. This basis is by construction orthonormal. In addition, the error of the POD basis can be calculated as

$$E(\boldsymbol{\zeta}_1, \dots, \boldsymbol{\zeta}_N) = \sum_{i=N+1}^{N_m} \sigma_i^2, \tag{2.37}$$

that is the sum of the eigenvalues omitted from the POD basis. This can be used to estimate the error of our ROM solution compared to the FOM solution. Say we want the average error to stay below a certain threshold, ε_{POD}. It is then sufficient to choose the smallest N such that

$$\sum_{i=1}^{N} \sigma_i^2 \Bigg/ \sum_{j=1}^{N_m} \sigma_j^2 \geq 1 - \varepsilon_{\text{POD}}^2. \tag{2.38}$$

Denote this N as N_r, the dimension of our RB space. The RB matrix V can then be constructed as $V = \left[|\boldsymbol{\zeta}_1|, \ldots, |\boldsymbol{\zeta}_{N_r}|\right] \in \mathbb{R}^{N_h \times N_r}$, where $N_r \ll N_h$. Once the matrix V is constructed, the FOM (equation (2.30)) can be projected onto our RB space:

$$\begin{aligned} V^T A_h(\boldsymbol{\mu}) V &= \sum_{q=1}^{Q_a} \theta_q(\boldsymbol{\mu}) V^T A_h^q V = \sum_{q=1}^{Q_a} \theta_q(\boldsymbol{\mu}) A_r^q = A_r(\boldsymbol{\mu}) \in \mathbb{R}^{N_r \times N_r}, \\ V^T \boldsymbol{f}_h(\boldsymbol{\mu}) &= \sum_{q=1}^{Q_f} \gamma_q(\boldsymbol{\mu}) V^T \boldsymbol{f}_h^q = \sum_{q=1}^{Q_f} \gamma_q(\boldsymbol{\mu}) \boldsymbol{f}_r^q = \boldsymbol{f}_r(\boldsymbol{\mu}) \in \mathbb{R}^{N_r}, \end{aligned} \tag{2.39}$$

see Figure 1. Thus we are left with the reduced linear system, referred to as the ROM:

$$A_r(\boldsymbol{\mu}) \boldsymbol{u}_r(\boldsymbol{\mu}) = \boldsymbol{f}_r(\boldsymbol{\mu}). \tag{2.40}$$

The reduced solution $\boldsymbol{u}_N(\boldsymbol{\mu})$ can then be projected back onto the high-fidelity space for visualization:

$$\boldsymbol{u}_h(\boldsymbol{\mu}) = V \boldsymbol{u}_r(\boldsymbol{\mu}). \tag{2.41}$$

Thus we have succeeded in reducing the original problem from a $N_h \times N_h$ linear system, to a $N_r \times N_r$ linear system. The error will then *typically* stay below ε_{POD}, although for a new set of parameters one must expect some added inaccuracies [31]. Typically $N_h \geq 10^4$, $10 \leq N_r \leq 30$, and the ROM can be solved in a fraction of the time it takes to solve the FOM [32].

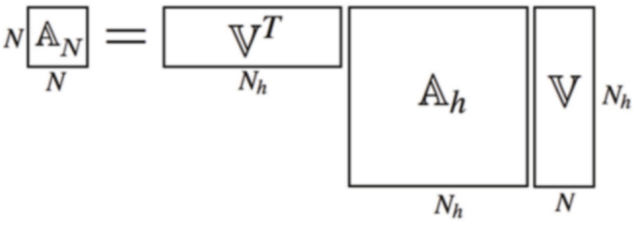

Figure 1: The transformation from A_h to A_r. Illustration from page 628 of [27].

3 Navier-Stokes and Stokes equation

We will now turn to the problem of interest, fluid flow in a system of pipes. First we will look at how the Stokes equation relates to the Navier-Stokes equation for incompressible Newtonian fluids. Let $\Omega \subset \mathbb{R}^3$, with $\partial\Omega = \Gamma_D \cup \Gamma_N$ where Γ_D, Γ_N is the part of the boundary with Dirichlet and Neumann boundary conditions, respectively. The strong form of Navier Stokes equation can then be derived from Newtons 2nd law and the law of mass conservation:

$$\begin{cases} \dfrac{\partial \boldsymbol{u}}{\partial t} + (\boldsymbol{u} \cdot \nabla)\boldsymbol{u} = -\nabla p + \nu \Delta \boldsymbol{u} + \boldsymbol{f} & \text{in } \Omega \times (0,T) \quad \text{(Newtons II law)}, \\ \nabla \cdot \boldsymbol{u} = 0 & \text{in } \Omega \times (0,T) \quad \text{(Mass conservation)}, \\ \boldsymbol{u} = \boldsymbol{g} & \text{on } \Gamma_D \times (0,T), \\ -p\boldsymbol{n} + \nu(\nabla \boldsymbol{u}) \cdot \boldsymbol{n} = \boldsymbol{0} & \text{on } \Gamma_N \times (0,T). \end{cases} \tag{3.1}$$

Here $\boldsymbol{u} = [u_x, u_y, u_z]^T$ is the fluid velocity, p is the internal pressure force, $\boldsymbol{f}$ are the external forces, $\boldsymbol{g}$ is some function describing the boundary datum, $\boldsymbol{n}$ is the outer normal vector, and ν is the kinematic viscosity. The first and second equations are known as the *momentum balance equation* and the *continuity equation*, respectively. In addition to assuming incompressibility, we will now make several important assumptions to simplify the problem:

- Stationarity: $\frac{\partial \boldsymbol{u}}{\partial t} = \boldsymbol{0}$.
- No external forces: $\boldsymbol{f} = \boldsymbol{0}$.
- Linearity: $(\boldsymbol{u} \cdot \nabla)\boldsymbol{u} = \boldsymbol{0}$.

Note that we will work in $\mathbb{R}^2$, thus also neglecting gravity as an external force. To justify the linearity assumption we assume that the velocities $\boldsymbol{u}$ are small compared to the viscosity term ν. Thus, we are left with the following simplified equation, the strong form of the (stationary and incompressible) Stokes equation:

$$\begin{cases} \nu \Delta \boldsymbol{u} - \nabla p = \boldsymbol{0} & \text{in } \Omega, \\ \nabla \cdot \boldsymbol{u} = 0 & \text{in } \Omega, \\ \boldsymbol{u} = \boldsymbol{g} & \text{on } \Gamma_D, \\ -p \cdot \boldsymbol{n} + \nu(\nabla \boldsymbol{u}) \cdot \boldsymbol{n} = \boldsymbol{0} & \text{on } \Gamma_N. \end{cases} \tag{3.2}$$

We will now use equation 3.2 to define the specific problem we intend to investigate, and obtain its weak formulation as in Section 2.2.1.

3.1 Setting up the problem

Consider an arbitrary domain $\Omega_{\text{sys}} \subset \mathbb{R}^2$, where Ω_{sys} represents some complete system of pipes. Let $\mathcal{A}$ be the set of all pipe-sections or sub-domains Ω_i necessary to construct any arbitrary pipe-system Ω_{sys}. Thus any specific pipe-system can be constructed as the union of a select few elements of $\mathcal{A}$, see Figure 2. We will refer to the elements of $\mathcal{A}$ as archetype components, and the set of necessary archetype components to construct Ω_{sys} as $\mathcal{A}_{\text{sys}} \subset \mathcal{A}$. Next, we introduce some local geometrical parameters for each archetype, that is $\Omega_i = \Omega_i(\boldsymbol{\mu}_{\text{g}})$. These parameters alter the initial geometry of the archetype through some geometrical transformation, allowing us to change each archetype into the desired shape. We design these parameters in such a way that setting all geometrical parameters to zero yields the initial geometry of the archetype: we will refer to this choice of parameters as the *initial parameters*. Note that the geometrical parameters $\boldsymbol{\mu}_{\text{g}}$ also affects the boundaries of each archetype. Let $\Gamma_{i,\text{I}}(\boldsymbol{\mu}_{\text{g}}), \Gamma_{i,\text{W}}(\boldsymbol{\mu}_{\text{g}}), \Gamma_{i,\text{O}}(\boldsymbol{\mu}_{\text{g}})$ denote the inlet, walls, and outlet of archetype i, respectively. That is

$$\bar{\Omega}_i(\boldsymbol{\mu}_{\text{g}}) = \Omega_i(\boldsymbol{\mu}_{\text{g}}) \cup \partial\Omega_i(\boldsymbol{\mu}_{\text{g}}) = \Omega_i(\boldsymbol{\mu}_{\text{g}}) \cup \Gamma_{i,\text{I}}(\boldsymbol{\mu}_{\text{g}}) \cup \Gamma_{i,\text{W}}(\boldsymbol{\mu}_{\text{g}}) \cup \Gamma_{i,\text{O}}(\boldsymbol{\mu}_{\text{g}}). \tag{3.3}$$

Note that connecting two archetypes will leave one overlapping boundary, that is the outlet and inlet of two adjacent archetypes:

$$\partial\Omega_i \cap \partial\Omega_j = \Gamma_{i,\text{O}} = \Gamma_{j,\text{I}}, \quad \text{for } \Omega_i, \Omega_j \text{ adjacent.} \tag{3.4}$$

To avoid this overlap, we remove the inlet boundary of every archetype following the first archetype in the system. Hence, we should be able to construct the geometry of any given pipe-system as

$$\bar{\Omega}_{\text{sys}} = \bigcup_{\Omega_i \in \mathcal{A}_{\text{sys}}} \bar{\Omega}_i(\boldsymbol{\mu}_{\text{g}}) \setminus \Gamma_{i,\text{I}}(\boldsymbol{\mu}_{\text{g}}), \quad \text{unless } \Omega_i \text{ is the first archetype.} \tag{3.5}$$

Note that $\mathcal{A}_{\text{sys}}$ can contain multiple of the same archetypes as in Figure 2. Let the velocity space be defined as $\mathcal{V} = [H^1_{\Gamma_D}(\Omega)]^2$ and the pressure space as $\mathcal{Q} = L^2(\Omega)$. We seek the local solution pair $(\boldsymbol{u_i}, p_i) \in \mathcal{V} \times \mathcal{Q}$ on each archetype Ω_i, from which we can hopefully obtain the global solution pair on any arbitrary pipe-system Ω_{sys}:

$$(\boldsymbol{u}_{\text{sys}}, p_{\text{sys}}) = \bigcup_{\Omega_i \in \mathcal{A}_{\text{sys}}} (\boldsymbol{u_i}, p_i)\big|_{\bar{\Omega}_i \setminus \Gamma_{i,\text{I}}}, \quad \text{unless } \Omega_i \text{ is the first archetype.} \tag{3.6}$$

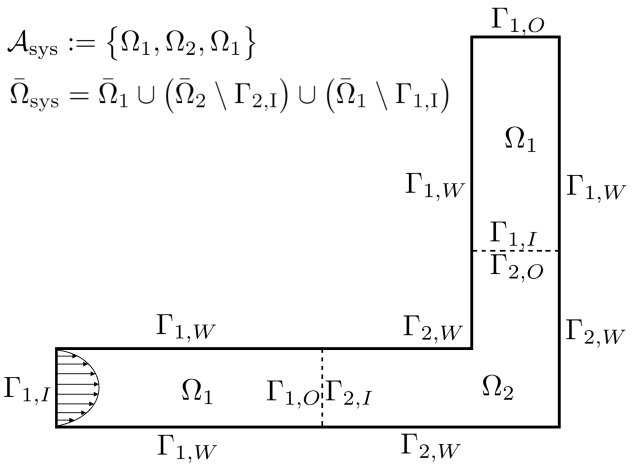

Figure 2: An example of a small pipe system consisting of three components, where two of the components are created from the same archetype.

3.1.1 Boundary conditions

Now that the geometry of any pipe-system can be constructed, the next issue we need to address is the boundary conditions. To impose the no-slip condition, we require that the velocity is zero on the walls of the archetype components, that is $\boldsymbol{u}|_{\Gamma_{\text{W}}} = \boldsymbol{0}$, or homogeneous Dirichlet boundary conditions on Γ_{W}. At the inlet of each archetype we assume that the velocity profile has a parabolic shape, where the amplitude of the parabola is given by μ_{a}. Note that since the inlet boundary depends on $\boldsymbol{\mu}_{\text{g}}$, so will the inlet velocity parabola. Thus $\boldsymbol{u}|_{\Gamma_{\text{I}}} = \mu_{\text{a}}\boldsymbol{g}(\boldsymbol{\mu}_{\text{g}})$, or non-homogeneous Dirichlet boundary conditions on Γ_{I}. Finally we leave the outlet boundary as is, that is imposing a homogeneous Neumann condition on Γ_{O}.

Finally we address the non-homogeneous Dirichlet boundary in standard fashion, by writing $\boldsymbol{u}$ as the sum of its homogeneous part $\boldsymbol{u}_0$ and a lifting vector function $\boldsymbol{r}_g \in [H^1_{\Gamma_D}(\Omega)]^2$, that is $\boldsymbol{u} = \boldsymbol{u}_0 + \boldsymbol{r}_g$ where $\boldsymbol{r}_g|_{\Gamma_{\text{I}}} = \mu_{\text{a}}\boldsymbol{g}(\boldsymbol{\mu}_{\text{g}})$ (and $\boldsymbol{u}_0|_{\Gamma_{\text{I}}} = \boldsymbol{0}$). Note that the lifting function does *not* have support on Γ_{O}, that is $\boldsymbol{r}_g|_{\Gamma_{\text{O}}} = \boldsymbol{0}$. Hence we arrive at the strong form of the Stokes equation for each archetype:

$$
\begin{cases}
\nu\Delta\boldsymbol{u}_0 - \nabla p = -\nu\Delta\boldsymbol{r}_g & \text{in } \Omega_i(\boldsymbol{\mu}_{\text{g}}), \\
\nabla\cdot\boldsymbol{u}_0 = -\nabla\cdot\boldsymbol{r}_g & \text{in } \Omega_i(\boldsymbol{\mu}_{\text{g}}), \\
\boldsymbol{u}_0 = \boldsymbol{0} & \text{on } \Gamma_{\text{I}}(\boldsymbol{\mu}_{\text{g}}) \cup \Gamma_{\text{W}}(\boldsymbol{\mu}_{\text{g}}), \\
\boldsymbol{r}_g = \mu_{\text{a}}\boldsymbol{g}(\boldsymbol{\mu}_{\text{g}}) & \text{on } \Gamma_{\text{I}}(\boldsymbol{\mu}_{\text{g}}), \\
-p\boldsymbol{n} + \nu(\nabla\boldsymbol{u}_0)\cdot\boldsymbol{n} = \boldsymbol{0} & \text{on } \Gamma_{\text{O}}(\boldsymbol{\mu}_{\text{g}}).
\end{cases}
\tag{3.7}
$$

3.1.2 Weak form

Consider the two previously defined spaces $\mathcal{V} = [H^1_{\Gamma_D}(\Omega)]^2, \mathcal{Q} = L^2(\Omega)$. Let $\boldsymbol{v}, q$ be test functions belonging to said spaces, $\boldsymbol{v} \in \mathcal{V}, q \in \mathcal{Q}$. Similar to what we did in section 2.2.1, we obtain the weak formulation by multiplying the momentum balance equation with $\boldsymbol{v}$ and the continuity equation with q, and integrating over the domain. We will look at the components of $\boldsymbol{u}$ and $\boldsymbol{v}$ separately to simplify notation:

$$\begin{cases} \nu \int_{\Omega_i} \Delta u_x v_x \, d\Omega - \int_{\Omega_i} \dfrac{\partial p}{\partial x} v_x \, d\Omega = -\nu \int_{\Omega_i} \Delta r_{gx} v_x \, d\Omega, \\ \nu \int_{\Omega_i} \Delta u_y v_y \, d\Omega - \int_{\Omega_i} \dfrac{\partial p}{\partial y} v_y \, d\Omega = -\nu \int_{\Omega_i} \Delta r_{gy} v_y \, d\Omega, \\ \int_{\Omega_i} \dfrac{\partial u_x}{\partial x} q \, d\Omega + \int_{\Omega_i} \dfrac{\partial u_y}{\partial y} q \, d\Omega = -\int_{\Omega_i} \dfrac{\partial r_{gx}}{\partial x} q \, d\Omega - \int_{\Omega_i} \dfrac{\partial r_{gy}}{\partial y} q \, d\Omega. \end{cases} \tag{3.8}$$

Next we apply Green's first identity:

$$\begin{cases} -\nu \int_{\Omega_i} \nabla u_x \nabla v_x \, d\Omega + \int_{\Omega_i} p \dfrac{\partial v_x}{\partial x} \, d\Omega + \int_{\Gamma_O} v_x \Big[\nu (\nabla u_x) \cdot \boldsymbol{n} - (p n_x) \Big] \, d\Gamma_O = \nu \int_{\Omega_i} \nabla r_{gx} \nabla v_x \, d\Omega, \\ -\nu \int_{\Omega_i} \nabla u_y \nabla v_y \, d\Omega + \int_{\Omega_i} p \dfrac{\partial v_y}{\partial y} \, d\Omega + \int_{\Gamma_O} v_y \Big[\nu (\nabla u_y) \cdot \boldsymbol{n} - (p n_y) \Big] \, d\Gamma_O = \nu \int_{\Omega_i} \nabla r_{gy} \nabla v_y \, d\Omega, \\ \int_{\Omega_i} q \dfrac{\partial u_x}{\partial x} \, d\Omega + \int_{\Omega_i} q \dfrac{\partial u_y}{\partial y} \, d\Omega = -\int_{\Omega_i} q \dfrac{\partial r_{gx}}{\partial x} \, d\Omega - \int_{\Omega_i} q \dfrac{\partial r_{gy}}{\partial y} \, d\Omega. \end{cases} \tag{3.9}$$

Note that the integral over Γ_O vanishes due to the chosen boundary conditions, leaving us with

$$\begin{cases} \nu \int_{\Omega_i} \nabla u_x \nabla v_x \, d\Omega - \int_{\Omega_i} p \dfrac{\partial v_x}{\partial x} \, d\Omega = -\nu \int_{\Omega_i} \nabla r_{gx} \nabla v_x \, d\Omega, \\ \nu \int_{\Omega_i} \nabla u_y \nabla v_y \, d\Omega - \int_{\Omega_i} p \dfrac{\partial v_y}{\partial y} \, d\Omega = -\nu \int_{\Omega_i} \nabla r_{gy} \nabla v_y \, d\Omega, \\ \int_{\Omega_i} q \dfrac{\partial u_x}{\partial x} \, d\Omega + \int_{\Omega_i} q \dfrac{\partial u_y}{\partial y} \, d\Omega = -\int_{\Omega_i} q \dfrac{\partial r_{gx}}{\partial x} \, d\Omega - \int_{\Omega_i} q \dfrac{\partial r_{gy}}{\partial y} \, d\Omega. \end{cases} \tag{3.10}$$

We can now define the three bilinear forms

$$\begin{aligned} a(\cdot,\cdot) &: H^1_{\Gamma_D}(\Omega) \times H^1_{\Gamma_D}(\Omega) \to \mathbb{R}, \\ b_x(\cdot,\cdot) &: H^1_{\Gamma_D}(\Omega) \times L^2 \to \mathbb{R}, \\ b_y(\cdot,\cdot) &: H^1_{\Gamma_D}(\Omega) \times L^2 \to \mathbb{R}, \end{aligned} \tag{3.11}$$

where

$$\begin{aligned} a(v,w) &= \nu \int_{\Omega_i} \nabla v \nabla w \, d\Omega, \\ b_x(v,q) &= -\int_{\Omega_i} q \dfrac{\partial v}{\partial x} \, d\Omega, \\ b_y(v,q) &= -\int_{\Omega_i} q \dfrac{\partial v}{\partial y} \, d\Omega. \end{aligned} \tag{3.12}$$

Thus we arrive at the weak formulation of our problem:

Find $(\boldsymbol{u}, p) \in \mathcal{V} \times \mathcal{Q}$ such that

$$\begin{cases} a(u_x, v_x) + b_x(v_x, p) = -a(r_{gx}, v_x), & \\ a(u_y, v_y) + b_y(v_y, p) = -a(r_{gy}, v_y), & \forall \boldsymbol{v} \in \mathcal{V}, \\ b_x(u_x, q) + b_y(u_y, q) = -b_x(r_{gx}, q) - b_y(r_{gy}, q), & \forall q \in \mathcal{Q}. \end{cases} \tag{3.13}$$

3.2 The Taylor-Hood element

As in section 2.2.3, we aim to discretize the problem so we can approximate $(\boldsymbol{u}, p)$ as the solution of a linear system of equations, $(\boldsymbol{u}_h, p_h)$. But unlike Poisson-equation, our discrete solution pair exist in two different spaces: the velocity space $\mathcal{V}_h \subset \mathcal{V}$ and the pressure space $\mathcal{Q}_h \subset \mathcal{Q}$. Essentially $\mathcal{Q}_h$ acts as a set of constraints on the velocity $\boldsymbol{u}_h$, and if the dimensionality of $\mathcal{Q}_h$ is too large compared to $\mathcal{V}_h$, there are not enough dofs for the velocity $\boldsymbol{u}_h$. In addition, the Ladyzhenskaia-Babuška-Brezzi (LBB) *inf-sup condition* must be satisfied for any h for the solution to be both stable and unique, further restricting the viable methods of discretizing the problem [33]. We will discuss this condition further once the problem have been discretized.

Hence we turn to a particular class of elements, the Taylor-Hood elements [34]. Let k denote the degree of the basis functions associated with a discrete space, and let P, Q indicate whether the elements are triangular or quadrilateral, respectively (i.e. Q_2 is a discrete space constructed from quadrilateral elements with biquadratic basis functions). We denote by $Q_{k'}/Q_k$ (or $P_{k'}/P_k$) the Taylor-Hood element associated with two discrete spaces (in our case $\mathcal{V}_h \times \mathcal{Q}_h$), where the basis functions of the first space are of degree k', and the basis functions of the second space are of degree k. It can be shown that for the Stokes equation, $k' = k + 1$ is sufficient to ensure both solvability of the linear system, and stability of the solution, given that the spaces are at least C^0 continuous [35]. We will use the Q_2/Q_1 Taylor-Hood element for this problem, see Figure 3. This was chosen to ease numerical implementation.

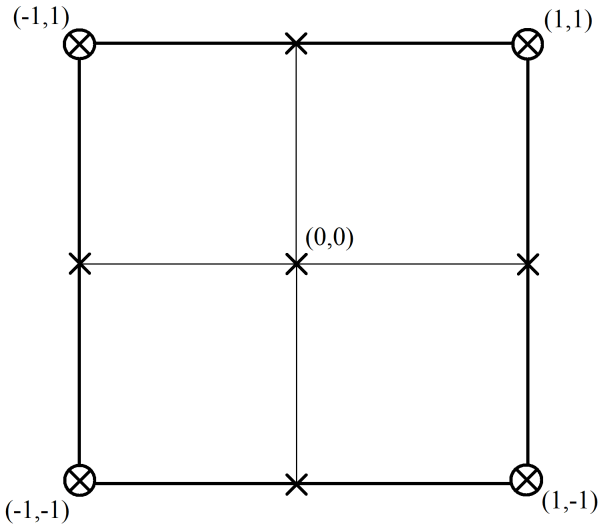

Figure 3: The Q_2/Q_1 Taylor-Hood reference element. X indicates a velocity-node, O indicates a pressure-node.

3.2.1 Defining the basis functions

As Figure 3 indicates we have nine velocity-nodes and four pressure-nodes on each element, where each node has a corresponding basis function. We will define the basis functions in terms of coordinates on the reference element $\xi, \eta \in [-1, 1]$, and later we introduce a mapping from an arbitrary element to this reference element. Let $\psi_i(\xi, \eta), \varphi_{i'}(\xi, \eta)$ be the basis functions for the velocity and pressure, respectively. As in section 2.2.4, we require that $\psi_i(\xi_j, \eta_j), \varphi_{i'}(\xi_{j'}, \eta_{j'}) = \delta_{ij}$. That is the value of basis function i is one at node i, and zero at any other node. To enforce the biquadratic form on the velocity-basis we also require that

$$\psi_i(\xi, \eta) = C_0^i + C_1^i \xi + C_2^i \eta + C_3^i \xi\eta + C_4^i \xi^2 + C_5^i \eta^2 + C_6^i \xi^2\eta + C_7^i \xi\eta^2 + C_8^i \xi^2\eta^2, \tag{3.14}$$

and similarly for the bilinear pressure-basis

$$\varphi_{i'}(\xi, \eta) = C_0^{i'} + C_1^{i'} \xi + C_2^{i'} \eta + C_3^{i'} \xi\eta. \tag{3.15}$$

The coefficients are of each basis function are then determined by solving a linear system just as in section 2.2.4. Two of the basis functions are shown in Figure 4.

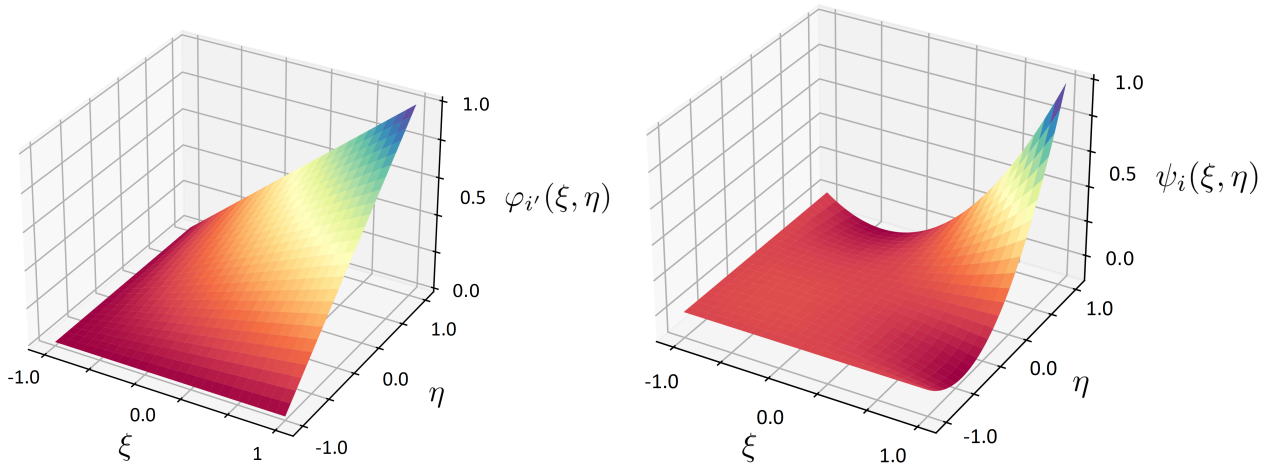

(a) One of the four bilinear basis functions

(b) One of the nine biquadratic basis functions

Figure 4: Two examples of the basis functions on the reference element.

3.3 Numerical integration, Gaussian quadrature

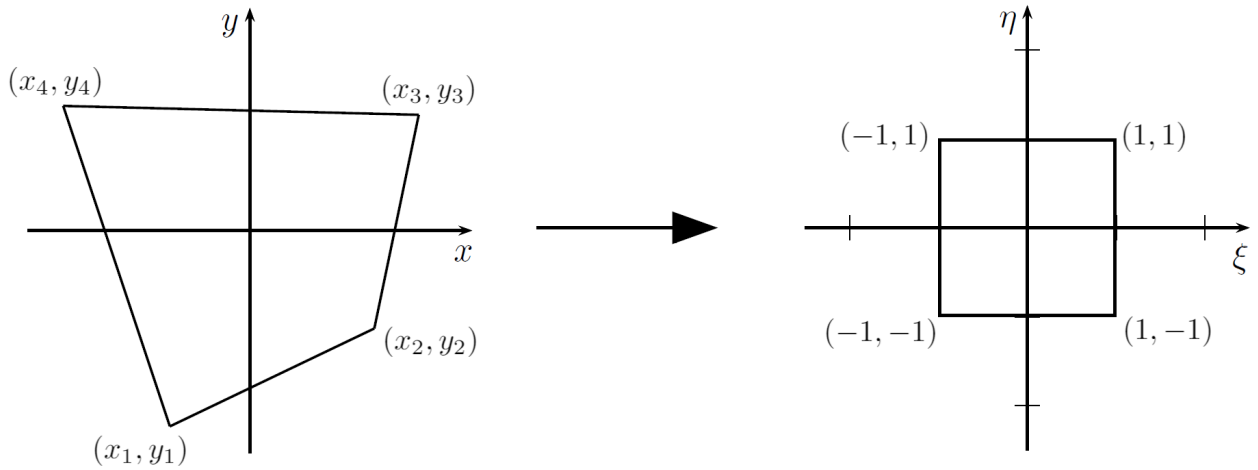

Figure 5: The mapping from an arbitrary quadrilateral element to the reference element.

To evaluate the bilinear forms, a Gaussian quadrature is used. With $f(\xi, \eta)$ as the integrand, we have that

$$\int_{-1}^{1}\int_{-1}^{1} f(\xi,\eta)\, d\xi d\eta \approx \sum_{i=1}^{n}\sum_{j=1}^{n} w_i w_j f(\xi_i, \eta_j), \tag{3.16}$$

where w_i, w_j, ξ_i, η_j are the weights and evaluation points associated with the Gaussian quadrature of degree n. For an arbitrary quadrilateral element, we must first map to this reference element:

$$\int_a^b\int_c^d f(x,y)\, dxdy = \int_{-1}^{1}\int_{-1}^{1} f(\xi,\eta) \begin{vmatrix} \frac{\partial x}{\partial \xi} & \frac{\partial x}{\partial \eta} \\ \frac{\partial y}{\partial \xi} & \frac{\partial y}{\partial \eta} \end{vmatrix} d\xi d\eta \approx \sum_{i=1}^{n}\sum_{j=1}^{n} w_i w_j \Big(\frac{\partial x}{\partial \xi}\frac{\partial y}{\partial \eta} - \frac{\partial x}{\partial \eta}\frac{\partial y}{\partial \xi}\Big) f(\xi_i, \eta_j). \tag{3.17}$$

The change of variables can be defined as follows:

$$x = \sum_{i=1}^{4} N_i(\xi,\eta) x_i, \quad y = \sum_{i=1}^{4} N_i(\xi,\eta) x_i, \tag{3.18}$$

where (x_i, y_i) are the vertices of the original quadrilateral (see Figure 5), and

$$\begin{aligned} N_1 &= \frac{1}{4}(1-\xi)(1-\eta), \quad N_2 = \frac{1}{4}(1+\xi)(1-\eta), \\ N_3 &= \frac{1}{4}(1+\xi)(1+\eta), \quad N_4 = \frac{1}{4}(1-\xi)(1+\eta). \end{aligned} \tag{3.19}$$

Thus the partial derivatives are

$$\begin{aligned} \frac{\partial x}{\partial \xi} &= \frac{1}{4}\Big[(1-\eta)(x_2 - x_1) + (1+\eta)(x_3 - x_4)\Big], \\ \frac{\partial x}{\partial \eta} &= \frac{1}{4}\Big[(1-\xi)(x_4 - x_1) + (1+\xi)(x_3 - x_2)\Big], \end{aligned} \tag{3.20}$$

and quite similar for $\frac{\partial y}{\partial \xi}, \frac{\partial y}{\partial \eta}$.

3.4 Discretization of the equation

Now that we have acquired a basis for both $\mathcal{V}_h$ and $\mathcal{Q}_h$, we can proceed with the discretization, starting with the Galerkin formulation of our problem:

$$\text{Find } (\boldsymbol{u}_h, p_h) \in \mathcal{V}_h \times \mathcal{Q}_h \text{ such that}$$

$$\begin{cases} a(u_{x,h}, v_{x,h}) + b_x(v_{x,h}, p_h) = -a(r_{gx,h}, v_{x,h}), & \\ a(u_{y,h}, v_{y,h}) + b_{y,h}(v_{y,h}, p_h) = -a(r_{gy,h}, v_{y,h}), & \forall \boldsymbol{v}_h \in \mathcal{V}_h, \\ b_x(u_{x,h}, q_h) + b_y(u_{y,h}, q_h) = -b_x(r_{gx,h}, q_h) - b_y(r_{gy,h}, q_h), & \forall q_h \in \mathcal{Q}_h. \end{cases} \tag{3.21}$$

Next we express $\boldsymbol{u}_h, \boldsymbol{r}_{g,h}, \boldsymbol{v}_h, p_h, q_h$ as linear combinations of the basis of their respective spaces. Let $\dim(\mathcal{V}_h) = N_u > \dim(\mathcal{Q}_h) = N_p$. Then

$$\begin{aligned} u_{x,h} &= \sum_{j=1}^{N_u} u_{x,h}^{(j)} \psi_j, & u_{y,h} &= \sum_{j=1}^{N_u} u_{y,h}^{(j)} \psi_j, \\ r_{gx,h} &= \sum_{j=1}^{N_u} r_{gx,h}^{(j)} \psi_j, & r_{gy,h} &= \sum_{j=1}^{N_u} r_{gy,h}^{(j)} \psi_j, \\ v_{x,h} &= \sum_{i=1}^{N_u} v_{x,h}^{(i)} \psi_i, & v_{y,h} &= \sum_{i=1}^{N_u} v_{y,h}^{(i)} \psi_i, \\ p_h &= \sum_{j=1}^{N_p} p_h^{(j)} \varphi_j, & q_h &= \sum_{i=1}^{N_p} q_h^{(i)} \varphi_i. \end{aligned} \tag{3.22}$$

Note that $\psi = \psi(x, y),\ \varphi = \varphi(x, y)$. Inserted into the bilinear forms we get

$$\begin{aligned} a(u_{x,h}, v_{x,h}) &= \sum_{j=1}^{N_u} \sum_{i=1}^{N_u} v_{x,h}^{(i)} a(\psi_j, \psi_i) u_{x,h}^{(j)} = \boldsymbol{v}_x^T A \boldsymbol{u}_x, \quad b_x(v_{x,h}, p_h) = \sum_{j=1}^{N_p} \sum_{i=1}^{N_u} p_h^{(j)} b_x(\psi_i, \varphi_j) v_{x,h}^{(i)} = \boldsymbol{p}^T B_x \boldsymbol{v}_x, \\ a(r_{gx,h}, v_{x,h}) &= \sum_{j=1}^{N_u} \sum_{i=1}^{N_u} v_{x,h}^{(i)} a(\psi_j, \psi_i) r_{gx,h}^{(j)} = \boldsymbol{v}_x^T A \boldsymbol{r}_{gx}, \quad b_y(u_{y,h}, q_h) = \sum_{i=1}^{N_p} \sum_{j=1}^{N_u} q_h^{(i)} b_y(\psi_j, \varphi_i) u_{y,h}^{(j)} = \boldsymbol{q}^T B_y \boldsymbol{u}_y, \end{aligned} \tag{3.23}$$

where

$$\begin{aligned} (A)_{i,j} &= a(\psi_j, \psi_i), \quad \dim(A) = N_u \times N_u, \\ (B_x)_{i,j} &= b_x(\psi_i, \varphi_j), \quad \dim(B_x) = N_p \times N_u, \\ (B_y)_{i,j} &= b_y(\psi_i, \varphi_j), \quad \dim(B_y) = N_p \times N_u, \end{aligned} \tag{3.24}$$

and similarly for the remaining terms. Note that since $\boldsymbol{x}^T A \boldsymbol{y} = \boldsymbol{y}^T A^T \boldsymbol{x}$ we can rewrite our problem as

$$\begin{cases} \boldsymbol{v}_x^T A \boldsymbol{u}_x + \boldsymbol{v}_x^T B_x^T \boldsymbol{p} = -\boldsymbol{v}_x^T A \boldsymbol{r}_{gx}, \\ \boldsymbol{v}_y^T A \boldsymbol{u}_y + \boldsymbol{v}_y^T B_y^T \boldsymbol{p} = -\boldsymbol{v}_y^T A \boldsymbol{r}_{gy}, \\ \boldsymbol{q}^T B_x \boldsymbol{u}_x + \boldsymbol{q}^T B_y \boldsymbol{u}_y = -\boldsymbol{q}^T B_x \boldsymbol{r}_{gx} - \boldsymbol{q}^T B_y \boldsymbol{r}_{gy}. \end{cases} \tag{3.25}$$

This must hold for all $v_h \in \mathcal{V}_h, q_h \in \mathcal{Q}_h$, which implies

$$\begin{cases} A \boldsymbol{u}_x + B_x^T \boldsymbol{p} = -A \boldsymbol{r}_{gx}, \\ A \boldsymbol{u}_y + B_y^T \boldsymbol{p} = -A \boldsymbol{r}_{gy}, \\ B_x \boldsymbol{u}_x + B_y \boldsymbol{u}_y = -B_x \boldsymbol{r}_{gx} - B_y \boldsymbol{r}_{gy}. \end{cases} \tag{3.26}$$

We now collect these matrices in a block-matrix to ease notation. Let $\boldsymbol{A}$ be the block matrix, and $\boldsymbol{z}, \boldsymbol{f}$ the concatenated vectors of unknowns and loads, respectively. That is

$$\boldsymbol{Az} = \boldsymbol{f} \Leftrightarrow \begin{bmatrix} A & 0 & B_x^T \\ 0 & A & B_y^T \\ B_x & B_y & 0 \end{bmatrix} \begin{bmatrix} \boldsymbol{u}_x \\ \boldsymbol{u}_y \\ \boldsymbol{p} \end{bmatrix} = \begin{bmatrix} -A\boldsymbol{r}_{gx} \\ -A\boldsymbol{r}_{gy} \\ -B_x\boldsymbol{r}_{gx} - B_y\boldsymbol{r}_{gy} \end{bmatrix}. \tag{3.27}$$

Thus we have obtained the linear system of equations, the FOM [36]. Note that every component of this linear system will depend on the parameters $\boldsymbol{\mu}$, that is $\boldsymbol{A}(\boldsymbol{\mu})\boldsymbol{z}(\boldsymbol{\mu}) = \boldsymbol{f}(\boldsymbol{\mu})$. In addition, each archetype will have a unique FOM associated to it that also depends on its local parameters. That is, for archetype Ω_i, we have $\boldsymbol{A}_i(\boldsymbol{\mu_i})\boldsymbol{z_i}(\boldsymbol{\mu_i}) = \boldsymbol{f_i}(\boldsymbol{\mu_i})$. In the next section we discuss the uniqueness and stability of this linear system, before we obtain the general form of the ROM.

3.5 Uniqueness and stability, the LBB inf-sup condition

The linear system obtained in the previous section is a *saddle point problem*. The Ladyzhenskaia-Babuška-Brezzi (LBB) inf-sup condition is sufficient for such problems to have a unique solution, that also depends continuously on the input data [3]. As before, let $\mathcal{V}_h \subset \mathcal{V}$ and $\mathcal{Q}_h \subset \mathcal{Q}$ be the two discrete Hilbert spaces, and let $a(\cdot,\cdot) : \mathcal{V}_h \times \mathcal{V}_h \to \mathbb{R}$, $b(\cdot,\cdot) : \mathcal{V}_h \times \mathcal{Q}_h \to \mathbb{R}$ be the two bilinear forms. Let $f_1(\cdot) \in \mathcal{V}'$, $f_2(\cdot) \in \mathcal{Q}'$, where $\mathcal{V}', \mathcal{Q}'$ are the dual spaces. Additionally we need to define a subspace of $\mathcal{V}_h$:

$$\mathcal{V}_0^h = \{v_h \in \mathcal{V}_h : b(v_h, q_h) = 0 \quad \forall q_h \in \mathcal{Q}_h\} \subset \mathcal{V}_h, \tag{3.28}$$

i.e. $\mathcal{V}_0^h$ is the kernel of $b(\cdot,\cdot)$. Again we consider the Galerkin formulation of the mixed variational problem:

$$\text{Find } (u_h, p_h) \in \mathcal{V}_h \times \mathcal{Q}_h \text{ such that}$$

$$\begin{cases} a(u_h, v_h) + b(v_h, p_h) = f_1(v_h), & \forall v_h \in \mathcal{V}_h, \\ b(u_h, q_h) = f_2(q_h), & \forall q_h \in \mathcal{Q}_h. \end{cases} \tag{3.29}$$

This problem is well posed, given that the following assumptions hold:

Theorem 3.1 (Ladyzhenskaya-Babuška-Brezzi inf-sup condition)**.** *Under the following assumptions:*

- ***Continuity:*** *There exists constants $\gamma_a, \gamma_b > 0$ such that*

$$\begin{aligned} |a(u_h, v_h)| &\leq \gamma_a ||u_h||_{\mathcal{V}} ||v_h||_{\mathcal{V}} \quad \forall u_h, v_h \in \mathcal{V}_h, \\ |b(v_h, q_h)| &\leq \gamma_b ||v_h||_{\mathcal{V}} ||q_h||_{\mathcal{Q}} \quad \forall v_h \in \mathcal{V}, q_h \in \mathcal{Q}_h. \end{aligned} \tag{3.30}$$

- ***Coercivity of*** *$a(\cdot,\cdot)$****:*** *There exists a constant $\alpha > 0$ such that $a(\cdot,\cdot)$ is coercive on the kernel of $b(\cdot,\cdot)$, that is*

$$\inf_{u_h \in \mathcal{V}_0^h} \sup_{v_h \in \mathcal{V}_0^h} \frac{a(u_h, v_h)}{||u_h||_{\mathcal{V}} ||v_h||_{\mathcal{V}}} \geq \alpha, \tag{3.31}$$

- ***Coercivity of*** *$b(\cdot,\cdot)$****:*** *There exists a constant $\beta > 0$ such that $b(\cdot,\cdot)$ satisfies the inf-sup condition*

$$\inf_{q_h \in \mathcal{Q}_h} \sup_{v_h \in \mathcal{V}_h} \frac{b(v_h, q_h)}{||v_h||_{\mathcal{V}} ||q_h||_{\mathcal{Q}}} \geq \beta, \tag{3.32}$$

where β is independent of h. Then for every $h > 0$, there exists a unique solution $(u_h, p_h) \in \mathcal{V}_h \times \mathcal{Q}_h$ to the mixed variational problem, which also satisfies the stability estimates

$$\begin{aligned} ||u_h||_{\mathcal{V}} &\leq \frac{1}{\alpha}\Big[||f_1||_{\mathcal{V}'} + \frac{\alpha+\gamma_a}{\beta}||f_2||_{\mathcal{Q}'}\Big], \\ ||p_h||_{\mathcal{Q}} &\leq \frac{1}{\beta}\Big[\Big(1+\frac{\gamma_a}{\alpha}\Big)||f_1||_{\mathcal{V}'} + \frac{\gamma_a(\alpha+\gamma_a)}{\alpha+\beta}||f_2||_{\mathcal{Q}'}\Big]. \end{aligned} \tag{3.33}$$

Additionally, the following error inequality holds:

$$||u-u_h||_{\mathcal{V}} + ||p-p_h||_{\mathcal{Q}} \leq C\Big(\inf_{v_h \in \mathcal{V}_h} ||u-v_h||_{\mathcal{V}} + \inf_{q_h \in \mathcal{Q}_h} ||p-q_h||_{\mathcal{Q}}\Big), \tag{3.34}$$

where $C = C(\alpha, \beta, \gamma_a, \gamma_b)$, but is independent of h.

We refer to [37] for the proof of this theorem. The assumption regarding the coercivity of $b(\cdot,\cdot)$ (Equation (3.32)) is another important reason why the Taylor-Hood element is the element of choice for this problem, as it has been shown to fulfill this criterion [38].

3.6 Reducing the system

For now, assume that for each archetype, there exists a well-defined mapping from the parameter-dependent domain to a parameter-independent reference domain. We will define such mappings for each of the archetypes in the next section. As in section 2.3.2, we aim to construct a RB matrix V using the POD method, so we can project the FOM onto our RB space. Note that our snapshots are the concatenated solutions of the FOM $\{\boldsymbol{z}(\boldsymbol{\mu}^1), \ldots, \boldsymbol{z}(\boldsymbol{\mu}^{N_n})\}$, where N_n is the number of snapshots, and

$$\boldsymbol{z}(\boldsymbol{\mu}^1) = \begin{bmatrix} \boldsymbol{u}_x(\boldsymbol{\mu}^1) \\ \boldsymbol{u}_y(\boldsymbol{\mu}^1) \\ \boldsymbol{p}_(\boldsymbol{\mu}^1) \end{bmatrix} \in \mathbb{R}^{2N_u+N_p}. \tag{3.35}$$

The snapshots are collected in the snapshot matrix S, and we compute its SVD. By choosing some tolerance ε_{POD}, we pick the N_r left-singular vectors corresponding to the N_r largest singular values, as in section 2.3.2. These vectors then make up our RB matrix V, where $V \in \mathbb{R}^{(2N_u+N_p)\times N_r}$. Thus we can rewrite our FOM as

$$V^T \boldsymbol{A}(\boldsymbol{\mu}) V V^T \boldsymbol{z}(\boldsymbol{\mu}) = V^T \boldsymbol{f}(\boldsymbol{\mu}). \tag{3.36}$$

Note that although $\boldsymbol{A}(\boldsymbol{\mu})$ could be written directly as a sum of affine functions and sub-matrices, it is easier to consider the block-components of $\boldsymbol{A}$ instead. First we write V as a block matrix:

$$V = \boldsymbol{V} = \begin{bmatrix} V_x \\ V_y \\ V_p \end{bmatrix}, \quad \boldsymbol{V}^T = \begin{bmatrix} V_x^T & V_y^T & V_p^T \end{bmatrix}, \quad V_x, V_y \in \mathbb{R}^{N_u \times N_r}, \quad V_p \in \mathbb{R}^{N_p \times N_r}. \tag{3.37}$$

Next we write $\boldsymbol{A}(\boldsymbol{\mu})$ in its full form and compute the matrix product $\boldsymbol{V}^T \boldsymbol{A}(\boldsymbol{\mu}) \boldsymbol{V}$:

$$\begin{bmatrix} V_x^T & V_y^T & V_p^T \end{bmatrix} \begin{bmatrix} A(\boldsymbol{\mu}) & 0 & B_x^T(\boldsymbol{\mu}) \\ 0 & A(\boldsymbol{\mu}) & B_y^T(\boldsymbol{\mu}) \\ B_x(\boldsymbol{\mu}) & B_y(\boldsymbol{\mu}) & 0 \end{bmatrix} \begin{bmatrix} V_x \\ V_y \\ V_p \end{bmatrix} = \begin{bmatrix} V_x^T A(\boldsymbol{\mu}) V_x & 0 & V_x^T B_x^T(\boldsymbol{\mu}) V_p \\ 0 & V_y^T A(\boldsymbol{\mu}) V_y & V_y^T B_y^T(\boldsymbol{\mu}) V_p \\ V_p^T B_x(\boldsymbol{\mu}) V_x & V_p^T B_y(\boldsymbol{\mu}) V_y & 0 \end{bmatrix}, \tag{3.38}$$

and similarly for $\boldsymbol{V}^T\boldsymbol{f}$:

$$\boldsymbol{V}^T\boldsymbol{f} = \begin{bmatrix} V_x^T & V_y^T & V_p^T \end{bmatrix} \begin{bmatrix} -A(\boldsymbol{\mu})\boldsymbol{r}_{gx} \\ -A(\boldsymbol{\mu})\boldsymbol{r}_{gy} \\ -B_x(\boldsymbol{\mu})\boldsymbol{r}_{gx} - B_y(\boldsymbol{\mu})\boldsymbol{r}_{gy} \end{bmatrix} = \begin{bmatrix} -V_x^T A(\boldsymbol{\mu})\boldsymbol{r}_{gx} \\ -V_y^T A(\boldsymbol{\mu})\boldsymbol{r}_{gy} \\ -V_p^T B_x(\boldsymbol{\mu})\boldsymbol{r}_{gx} - V_p^T B_y(\boldsymbol{\mu})\boldsymbol{r}_{gy} \end{bmatrix}. \tag{3.39}$$

Thus each sub-matrix of the block matrix $\boldsymbol{A}$ has an affine representation:

$$\begin{aligned} V_x^T A(\boldsymbol{\mu})V_x &= \sum_{q=1}^{Q_a} \theta_q(\boldsymbol{\mu}) V_x^T A^q V_x = \sum_{q=1}^{Q_a} \theta_q(\boldsymbol{\mu}) A_{x,r}^q = A_{x,r}(\boldsymbol{\mu}) \in \mathbb{R}^{N_r \times N_r}, \\ V_y^T A(\boldsymbol{\mu})V_y &= \sum_{q=1}^{Q_a} \theta_q(\boldsymbol{\mu}) V_y^T A^q V_y = \sum_{q=1}^{Q_a} \theta_q(\boldsymbol{\mu}) A_{y,r}^q = A_{y,r}(\boldsymbol{\mu}) \in \mathbb{R}^{N_r \times N_r}, \\ V_p^T B_x(\boldsymbol{\mu})V_x &= \sum_{q=1}^{Q_b} \gamma_{x,q}(\boldsymbol{\mu}) V_p^T B_x^q V_x = \sum_{q=1}^{Q_b} \gamma_{x,q}(\boldsymbol{\mu}) B_{x,r}^q = B_{x,r}(\boldsymbol{\mu}) \in \mathbb{R}^{N_r \times N_r}, \\ V_p^T B_y(\boldsymbol{\mu})V_y &= \sum_{q=1}^{Q_b} \gamma_{y,q}(\boldsymbol{\mu}) V_p^T B_y^q V_y = \sum_{q=1}^{Q_b} \gamma_{y,q}(\boldsymbol{\mu}) B_{y,r}^q = B_{y,r}(\boldsymbol{\mu}) \in \mathbb{R}^{N_r \times N_r}. \end{aligned} \tag{3.40}$$

And similarly for the components of the load vector $\boldsymbol{f}$:

$$\begin{aligned} V_x^T A(\boldsymbol{\mu}) &= \sum_{q=1}^{Q_a} \theta_q(\boldsymbol{\mu}) V_x^T A^q = \sum_{q=1}^{Q_a} \theta_q(\boldsymbol{\mu}) F_x^q = F_x(\boldsymbol{\mu}) \in \mathbb{R}^{N_r \times N_u}, \\ V_y^T A(\boldsymbol{\mu}) &= \sum_{q=1}^{Q_a} \theta_q(\boldsymbol{\mu}) V_y^T A^q = \sum_{q=1}^{Q_a} \theta_q(\boldsymbol{\mu}) F_y^q = F_y(\boldsymbol{\mu}) \in \mathbb{R}^{N_r \times N_u}, \\ V_p^T B_x(\boldsymbol{\mu}) &= \sum_{q=1}^{Q_b} \gamma_{x,q}(\boldsymbol{\mu}) V_p^T B_x^q = \sum_{q=1}^{Q_b} \gamma_{x,q}(\boldsymbol{\mu}) F_{px}^q = F_{px}(\boldsymbol{\mu}) \in \mathbb{R}^{N_r \times N_p}, \\ V_p^T B_y(\boldsymbol{\mu}) &= \sum_{q=1}^{Q_b} \gamma_{y,q}(\boldsymbol{\mu}) V_p^T B_y^q = \sum_{q=1}^{Q_b} \gamma_{y,q}(\boldsymbol{\mu}) F_{py}^q = F_{py}(\boldsymbol{\mu}) \in \mathbb{R}^{N_r \times N_p}. \end{aligned} \tag{3.41}$$

Note that although the number of columns in F_x, F_y, F_{px}, F_{pu} is the same as before reducing the system, we only need to consider the columns where the corresponding values of $\boldsymbol{r}_g$ is different from zero. The reduced linear system can then be written as

$$\boldsymbol{A}_r(\boldsymbol{\mu})\boldsymbol{z}_r(\boldsymbol{\mu}) = \begin{bmatrix} A_{x,r}(\boldsymbol{\mu}) & 0 & B_{x,r}^T(\boldsymbol{\mu}) \\ 0 & A_{y,r}(\boldsymbol{\mu}) & B_{y,r}^T(\boldsymbol{\mu}) \\ B_{x,r}(\boldsymbol{\mu}) & B_{y,r}(\boldsymbol{\mu}) & 0 \end{bmatrix} \begin{bmatrix} \boldsymbol{u}_{x,r}(\boldsymbol{\mu}) \\ \boldsymbol{u}_{y,r}(\boldsymbol{\mu}) \\ \boldsymbol{p}_r(\boldsymbol{\mu}) \end{bmatrix} = \begin{bmatrix} -F_x(\boldsymbol{\mu})\boldsymbol{r}_{gx}(\boldsymbol{\mu}) \\ -F_y(\boldsymbol{\mu})\boldsymbol{r}_{gy}(\boldsymbol{\mu}) \\ -F_{px}(\boldsymbol{\mu})\boldsymbol{r}_{gx}(\boldsymbol{\mu}) - F_{py}(\boldsymbol{\mu})\boldsymbol{r}_{gy}(\boldsymbol{\mu}) \end{bmatrix} = \boldsymbol{f}_r(\boldsymbol{\mu}), \tag{3.42}$$

and finally the full solution obtained from the reduced solution and the lifting functions:

$$\begin{bmatrix} \boldsymbol{u}_x \\ \boldsymbol{u}_y \\ \boldsymbol{p} \end{bmatrix} = \begin{bmatrix} V_x\boldsymbol{u}_{x,r} + \boldsymbol{r}_{gx} \\ V_y\boldsymbol{u}_{y,r} + \boldsymbol{r}_{gy} \\ V_p\boldsymbol{p}_r \end{bmatrix}. \tag{3.43}$$

4 The archetype components

In this section we will introduce the different archetype components, and define their related mappings and affine functions. Let us denote by $\boldsymbol{\Phi}_{\Omega_{i,j}}(x, y, \boldsymbol{\mu}_i)$ the linear mapping that maps the j-th partition of the i-th archetype from the reference domain to the parameter dependent domain. $\boldsymbol{\mu}_i$ are the local parameters belonging to archetype i. Let x', y' denote the coordinates on the parameter dependent domain. We will restrict these mappings to stretching and scaling only, giving us the general linear mapping

$$\begin{bmatrix} x' \\ y' \end{bmatrix} = \boldsymbol{\Phi}_{\Omega_{i,j}}(x, y, \boldsymbol{\mu}_i) = \begin{bmatrix} c_1(\boldsymbol{\mu}_i) & 0 \\ 0 & d_1(\boldsymbol{\mu}_i) \end{bmatrix} \begin{bmatrix} x \\ y \end{bmatrix} + \begin{bmatrix} c_2(\boldsymbol{\mu}_i) \\ d_2(\boldsymbol{\mu}_i) \end{bmatrix}, \tag{4.1}$$

here c_1, d_1, c_2, d_2 are typically linear functions with respect to $\boldsymbol{\mu}_i$, not to be confused with the bilinear forms. Mappings on this form ensures that the Jacobian $J_{\boldsymbol{\Phi}}$ will be constant with respect to x, y:

$$J_{\boldsymbol{\Phi}}(x, y, \boldsymbol{\mu}_i) = J_{\boldsymbol{\Phi}}(\boldsymbol{\mu}_i) \begin{bmatrix} c_1(\boldsymbol{\mu}_i) & 0 \\ 0 & d_1(\boldsymbol{\mu}_i) \end{bmatrix}. \tag{4.2}$$

We then map the bilinear forms from the parameter dependent domain to the parameter-independent domain:

$$\begin{aligned} a(\psi'_j, \psi'_i) &= \int_{\Omega'(\boldsymbol{\mu})} \nabla' \psi'_i \nabla' \psi'_j \, d\Omega'(\boldsymbol{\mu}) = \sum_{k,l=1}^{d} \int_{\Omega} M_{k,l} \frac{\partial \psi_i}{\partial x_k} \frac{\partial \psi_j}{\partial x_l} \, d\Omega, \\ b(\psi'_i \varphi'_j) &= \int_{\Omega'(\boldsymbol{\mu})} \varphi'_j (\nabla' \cdot \psi') \, d\Omega'(\boldsymbol{\mu}) = \sum_{k,l=1}^{d} \int_{\Omega} N_{k,l} \varphi_j \frac{\partial \psi_i}{\partial x_l} \, d\Omega, \end{aligned} \tag{4.3}$$

where $M(\boldsymbol{\mu}) = J_{\boldsymbol{\Phi}}^{-1} J_{\boldsymbol{\Phi}}^{-T} |J_{\boldsymbol{\Phi}}|, \quad N(\boldsymbol{\mu}) = J_{\boldsymbol{\Phi}}^{-T} |J_{\boldsymbol{\Phi}}|$. Note that the structure of $J_{\boldsymbol{\Phi}}$ make $M(\boldsymbol{\mu}), N(\boldsymbol{\mu})$ quite simple to compute:

$$M(\boldsymbol{\mu}_i) = \begin{bmatrix} \frac{d_1(\boldsymbol{\mu}_i)}{c_1(\boldsymbol{\mu}_i)} & 0 \\ 0 & \frac{c_1(\boldsymbol{\mu}_i)}{d_1(\boldsymbol{\mu}_i)} \end{bmatrix}, \quad N(\boldsymbol{\mu}_i) = \begin{bmatrix} d_1(\boldsymbol{\mu}_i) & 0 \\ 0 & c_1(\boldsymbol{\mu}_i) \end{bmatrix}. \tag{4.4}$$

Our bilinear forms on the reference domain are then

$$\begin{aligned} a(\psi_j, \psi_i) &= \frac{d_1(\boldsymbol{\mu})}{c_1(\boldsymbol{\mu})} \nu \int_{\Omega} \frac{\partial \psi_i}{\partial x} \frac{\partial \psi_j}{\partial x} \, d\Omega + \frac{c_1(\boldsymbol{\mu})}{d_1(\boldsymbol{\mu})} \nu \int_{\Omega} \frac{\partial \psi_i}{\partial y} \frac{\partial \psi_j}{\partial y} \, d\Omega, \\ b_x(\psi_i, \varphi_j) &= -d_1(\boldsymbol{\mu}) \int_{\Omega} \varphi_j \frac{\partial \psi_i}{\partial x} \, d\Omega, \\ b_y(\psi_i, \varphi_j) &= -c_1(\boldsymbol{\mu}) \int_{\Omega} \varphi_j \frac{\partial \psi_i}{\partial y} \, d\Omega. \end{aligned} \tag{4.5}$$

Note that every archetype will have inlets parallel to the y-axis. We assume that the y-component of the inlet velocity is zero, further simplifying our lifting function:

$$\boldsymbol{r}_g = \mu_a \boldsymbol{g}(\boldsymbol{\mu}) = \mu_a \begin{bmatrix} g_x(\boldsymbol{\mu}) \\ g_y(\boldsymbol{\mu}) \end{bmatrix} = \mu_a \begin{bmatrix} g_x(\boldsymbol{\mu}) \\ 0 \end{bmatrix}. \tag{4.6}$$

Additionally, we assume the inlet velocity to have a parabolic shape only depending on the width of the pipe, that is $\mu_a g_x(x', y', \boldsymbol{\mu}) = \mu_a g_x(y', \boldsymbol{\mu})$ where μ_a is the amplitude of the parabola.

4.1 Archetype 0 – The straight pipe

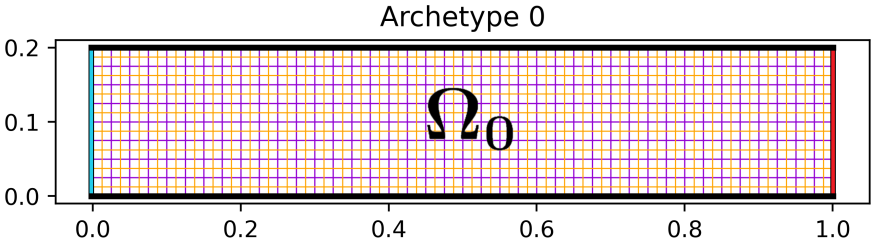

Figure 6: *Archetype 0 – The straight pipe*: Each purple square represents a Q_2/Q_1 Taylor-Hood element. The blue edge is the inlet, the black edges are the walls, and the red edge is the outlet.

Due to the simplicity of this archetype, there is no need to define any partitions. Let $\boldsymbol{\mu}_0 = [\mu^{(1)}, \mu^{(2)}]$ be the length and width of the pipe, respectively. Our mapping is then simply defined as

$$\boldsymbol{\Phi}_{\Omega_0}(x, y, \boldsymbol{\mu}_0) = \begin{bmatrix} 1+\mu^{(1)} & 0 \\ 0 & 1+\mu^{(2)} \end{bmatrix} \begin{bmatrix} x \\ y \end{bmatrix}, \tag{4.7}$$

i.e. $\mu^{(1)} = 1$ doubles the width of the pipe and so forth. To ensure a parabolic shape on the lifting function, let

$$g_x(y', \boldsymbol{\mu}_0) = C\big(0.2(1+\mu^{(2)}) - y'\big)y'. \tag{4.8}$$

The maximum value of this lifting function is $g_x = 0.01C(1+\mu^{(1)})^2$, which we want to be explicitly determined by μ_a. That is

$$0.01C(1+\mu^{(2)})^2 = \mu_a \Rightarrow C = \frac{100\mu_a}{(1+\mu^{(2)})^2}. \tag{4.9}$$

Thus we can express the lifting function both on the original domain, and on the reference domain:

$$\begin{aligned} g_x(y', \boldsymbol{\mu}_0) &= \frac{100\mu_a}{(1+\mu^{(2)})^2}\big(0.2(1+\mu^{(2)}) - y'\big)y', \\ g_x(y, \boldsymbol{\mu}_0) &= \frac{100\mu_a}{(1+\mu^{(2)})^2}\Big(0.2(1+\mu^{(2)}) - (1+\mu^{(2)})y\Big)(1+\mu^{(2)})y = 100\mu_a\big(0.2-y\big)y. \end{aligned} \tag{4.10}$$

The lifting function on the reference domain is used in the linear system, while the original lifting function is used when obtaining the final solution. Note that the geometrical parameters in the denominator cancels out on the reference domain, however this is not always the case. From equation (4.5), our affine functions and bilinear forms can be written as

$$\begin{aligned} \theta_1(\boldsymbol{\mu}_0) &= \frac{1+\mu^{(2)}}{1+\mu^{(1)}}, \quad a^{(1)}(\psi_j, \psi_i) = \nu \int_\Omega \frac{\partial \psi_i}{\partial x}\frac{\partial \psi_j}{\partial x}\, d\Omega, \\ \theta_2(\boldsymbol{\mu}_0) &= \frac{1+\mu^{(1)}}{1+\mu^{(2)}}, \quad a^{(2)}(\psi_j, \psi_i) = \nu \int_\Omega \frac{\partial \psi_i}{\partial y}\frac{\partial \psi_j}{\partial y}\, d\Omega, \\ \gamma_{x,1}(\boldsymbol{\mu}_0) &= 1+\mu^{(2)}, \quad b_x^{(1)}(\psi_i, \varphi_j) = -\int_\Omega \varphi_j \frac{\partial \psi_i}{\partial x}\, d\Omega, \\ \gamma_{y,1}(\boldsymbol{\mu}_0) &= 1+\mu^{(1)}, \quad b_y^{(1)}(\psi_i, \varphi_j) = -\int_\Omega \varphi_j \frac{\partial \psi_i}{\partial y}\, d\Omega. \end{aligned} \tag{4.11}$$

4.2 Archetype 1 – The closed bifurcation pipe

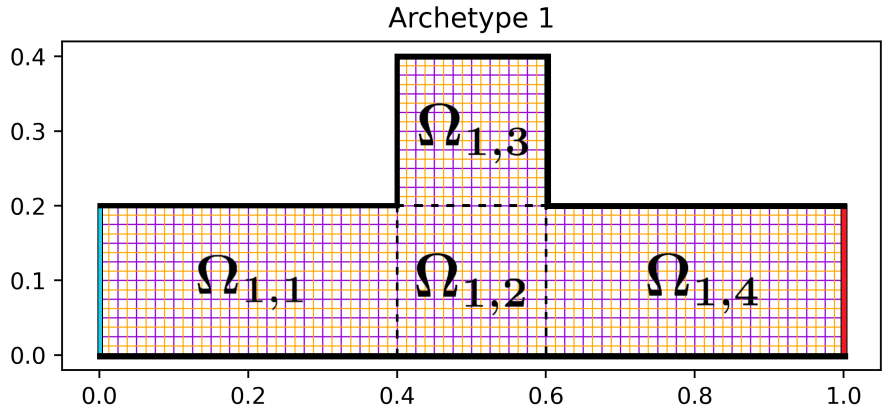

Figure 7: *Archetype 1 – The closed bifurcation pipe*: Each purple square represents a Q_2/Q_1 Taylor-Hood element. The blue edge is the inlet, the black edges are the walls, and the red edge is the outlet.

We partition the archetype into four sub-domains, to allow reshaping of both the length and width of each section. Let $\boldsymbol{\mu}_1 = [\mu^{(1)}, \mu^{(2)}, \mu^{(3)}, \mu^{(4)}, \mu^{(5)}]$ be the parameters, where $\mu^{(1)}$ controls the length of $\Omega_{1,1}$, $\mu^{(2)}$ the width of $\Omega_{1,1}, \Omega_{1,2}, \Omega_{1,4}$, $\mu^{(3)}$ the length of $\Omega_{1,2}, \Omega_{1,3}$, $\mu^{(4)}$ the width of $\Omega_{1,3}$, and $\mu^{(5)}$ the length of $\Omega_{1,4}$. This leads to the four parametric mappings

$$
\begin{aligned}
\boldsymbol{\Phi}_{\Omega_{1,1}}(x, y, \boldsymbol{\mu}_1) &= \begin{bmatrix} 1+\mu^{(1)} & 0 \\ 0 & 1+\mu^{(2)} \end{bmatrix} \begin{bmatrix} x \\ y \end{bmatrix} - \begin{bmatrix} 0.4\mu^{(1)} \\ 0.2\mu^{(2)} \end{bmatrix}, \\
\boldsymbol{\Phi}_{\Omega_{1,2}}(x, y, \boldsymbol{\mu}_1) &= \begin{bmatrix} 1+\mu^{(3)} & 0 \\ 0 & 1+\mu^{(2)} \end{bmatrix} \begin{bmatrix} x \\ y \end{bmatrix} - \begin{bmatrix} 0.4\mu^{(3)} \\ 0.2\mu^{(2)} \end{bmatrix}, \\
\boldsymbol{\Phi}_{\Omega_{1,3}}(x, y, \boldsymbol{\mu}_1) &= \begin{bmatrix} 1+\mu^{(3)} & 0 \\ 0 & 1+\mu^{(4)} \end{bmatrix} \begin{bmatrix} x \\ y \end{bmatrix} - \begin{bmatrix} 0.4\mu^{(3)} \\ 0.2\mu^{(4)} \end{bmatrix}, \\
\boldsymbol{\Phi}_{\Omega_{1,4}}(x, y, \boldsymbol{\mu}_1) &= \begin{bmatrix} 1+\mu^{(5)} & 0 \\ 0 & 1+\mu^{(2)} \end{bmatrix} \begin{bmatrix} x \\ y \end{bmatrix} - \begin{bmatrix} (0.6+0.2\mu^{(3)})\mu^{(5)} \\ 0.2\mu^{(2)} \end{bmatrix}.
\end{aligned}
\tag{4.12}
$$

The lifting function on the reference domain is identical to the straight pipe, although slightly different on the original domain:

$$
\begin{aligned}
g_x(y', \boldsymbol{\mu}_1) &= \frac{100\mu_a}{(1+\mu^{(2)})^2}\big(0.2 - y'\big)\big(y' + 0.2\mu^{(2)}\big), \\
g_x(y, \boldsymbol{\mu}_1) &= 100\mu_a\big(0.2 - y\big)y.
\end{aligned}
\tag{4.13}
$$

We get a total of sixteen affine functions (their respective bilinear forms can be found with Equation (4.5)):

$$
\begin{aligned}
&\theta_1(\boldsymbol{\mu}_1) = \frac{1+\mu^{(2)}}{1+\mu^{(1)}}, \quad \theta_2(\boldsymbol{\mu}_1) = \frac{1+\mu^{(1)}}{1+\mu^{(2)}}, && \theta_3(\boldsymbol{\mu}_1) = \frac{1+\mu^{(2)}}{1+\mu^{(3)}}, \quad \theta_4(\boldsymbol{\mu}_1) = \frac{1+\mu^{(3)}}{1+\mu^{(2)}}, \\
&\theta_5(\boldsymbol{\mu}_1) = \frac{1+\mu^{(4)}}{1+\mu^{(3)}}, \quad \theta_6(\boldsymbol{\mu}_1) = \frac{1+\mu^{(3)}}{1+\mu^{(4)}}, && \theta_7(\boldsymbol{\mu}_1) = \frac{1+\mu^{(2)}}{1+\mu^{(5)}}, \quad \theta_8(\boldsymbol{\mu}_1) = \frac{1+\mu^{(5)}}{1+\mu^{(2)}}, \\
&\gamma_{x,1}(\boldsymbol{\mu}_1) = 1+\mu^{(2)}, \quad \gamma_{x,2}(\boldsymbol{\mu}_1) = 1+\mu^{(2)}, && \gamma_{x,3}(\boldsymbol{\mu}_1) = 1+\mu^{(4)}, \quad \gamma_{x,4}(\boldsymbol{\mu}_1) = 1+\mu^{(2)}, \\
&\gamma_{y,1}(\boldsymbol{\mu}_1) = 1+\mu^{(1)}, \quad \gamma_{y,2}(\boldsymbol{\mu}_1) = 1+\mu^{(3)}, && \gamma_{y,3}(\boldsymbol{\mu}_1) = 1+\mu^{(3)}, \quad \gamma_{y,4}(\boldsymbol{\mu}_1) = 1+\mu^{(5)}.
\end{aligned}
\tag{4.14}
$$

4.3 Archetype 2 – The open bifurcation pipe

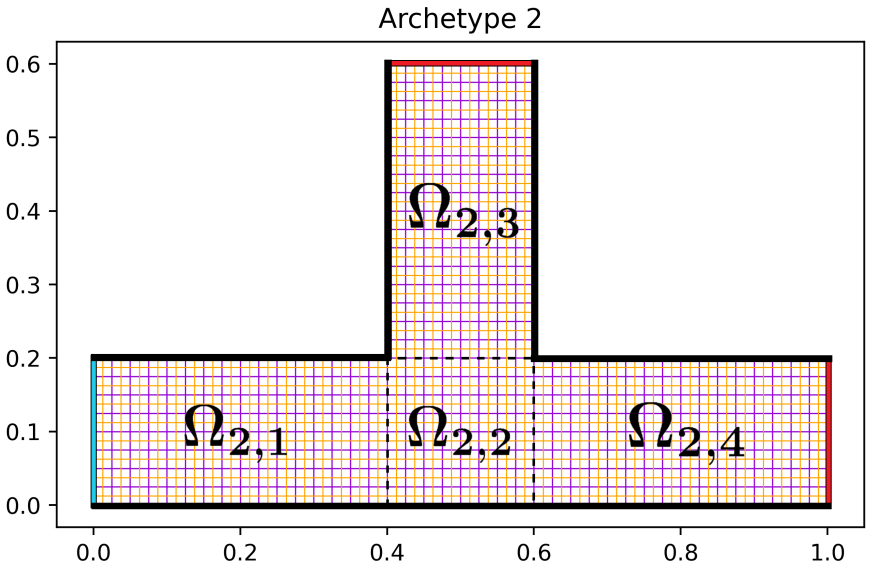

Figure 8: *Archetype 2 – The open bifurcation pipe*: Each purple square represents a Q_2/Q_1 Taylor-Hood element. The blue edge is the inlet, the black edges are the walls, and the red edges are the outlets.

Because of the similar shape to the previous archetype, all mappings, parameters, affine functions and bilinear forms are equal. The only major difference is the double outlet, and the slightly longer vertical pipe. Longer pipe sections leading up to the outlets are necessary to ensure that the velocity vector is perpendicular to the outlet edge, justifying our assumption of perpendicular inlet velocity for the next archetype.

4.4 Archetype 3 – The left-corner pipe

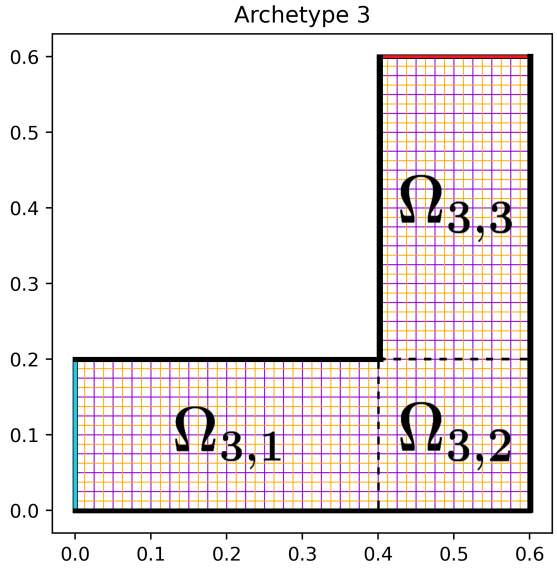

Figure 9: *Archetype 3 – The left-corner pipe*: Each purple square represents a Q_2/Q_1 Taylor-Hood element. The blue edge is the inlet, the black edges are the walls, and the red edge is the outlet.

Three partitions are necessary for us to control the length and width of both the inlet section and the outlet section of this pipe. Let $\boldsymbol{\mu}_3 = [\mu^{(1)}, \mu^{(2)}, \mu^{(3)}, \mu^{(4)}]$, where $\mu^{(1)}$ controls the length of $\Omega_{3,1}$, $\mu^{(2)}$ the width of $\Omega_{3,1}, \Omega_{3,2}$, $\mu^{(3)}$ the length of $\Omega_{3,2}, \Omega_{3,3}$, and $\mu^{(4)}$ the width of $\Omega_{3,3}$. This results in three mappings:

$$\begin{aligned}
\boldsymbol{\Phi}_{\Omega_{3,1}}(x, y, \boldsymbol{\mu}_3) &= \begin{bmatrix} 1+\mu^{(1)} & 0 \\ 0 & 1+\mu^{(2)} \end{bmatrix} \begin{bmatrix} x \\ y \end{bmatrix} - \begin{bmatrix} 0.4\mu^{(1)} \\ 0.2\mu^{(2)} \end{bmatrix}, \\
\boldsymbol{\Phi}_{\Omega_{3,2}}(x, y, \boldsymbol{\mu}_3) &= \begin{bmatrix} 1+\mu^{(3)} & 0 \\ 0 & 1+\mu^{(2)} \end{bmatrix} \begin{bmatrix} x \\ y \end{bmatrix} - \begin{bmatrix} 0.4\mu^{(3)} \\ 0.2\mu^{(2)} \end{bmatrix}, \\
\boldsymbol{\Phi}_{\Omega_{3,3}}(x, y, \boldsymbol{\mu}_3) &= \begin{bmatrix} 1+\mu^{(3)} & 0 \\ 0 & 1+\mu^{(4)} \end{bmatrix} \begin{bmatrix} x \\ y \end{bmatrix} - \begin{bmatrix} 0.4\mu^{(3)} \\ 0.2\mu^{(4)} \end{bmatrix}.
\end{aligned} \tag{4.15}$$

The lifting functions are identical to the previous archetype:

$$\begin{aligned}
g_x(y', \boldsymbol{\mu}_3) &= \frac{100\mu_a}{(1+\mu^{(2)})^2}\big(0.2 - y'\big)\big(y' + 0.2\mu^{(2)}\big), \\
g_x(y, \boldsymbol{\mu}_3) &= 100\mu_a\big(0.2 - y\big)y,
\end{aligned} \tag{4.16}$$

and we get twelve affine functions:

$$\begin{aligned}
\theta_1(\boldsymbol{\mu}_3) &= \frac{1+\mu^{(2)}}{1+\mu^{(1)}}, & \theta_2(\boldsymbol{\mu}_3) &= \frac{1+\mu^{(1)}}{1+\mu^{(2)}}, & \theta_3(\boldsymbol{\mu}_3) &= \frac{1+\mu^{(2)}}{1+\mu^{(3)}}, \\
\theta_4(\boldsymbol{\mu}_3) &= \frac{1+\mu^{(3)}}{1+\mu^{(2)}}, & \theta_5(\boldsymbol{\mu}_3) &= \frac{1+\mu^{(4)}}{1+\mu^{(3)}}, & \theta_6(\boldsymbol{\mu}_3) &= \frac{1+\mu^{(3)}}{1+\mu^{(4)}}, \\
\gamma_{x,1}(\boldsymbol{\mu}_3) &= 1+\mu^{(2)}, & \gamma_{x,2}(\boldsymbol{\mu}_3) &= 1+\mu^{(2)}, & \gamma_{x,3}(\boldsymbol{\mu}_3) &= 1+\mu^{(4)}, \\
\gamma_{y,1}(\boldsymbol{\mu}_3) &= 1+\mu^{(1)}, & \gamma_{y,2}(\boldsymbol{\mu}_3) &= 1+\mu^{(3)}, & \gamma_{y,3}(\boldsymbol{\mu}_3) &= 1+\mu^{(3)}.
\end{aligned} \tag{4.17}$$

4.5 Archetype 4 – The right-corner pipe

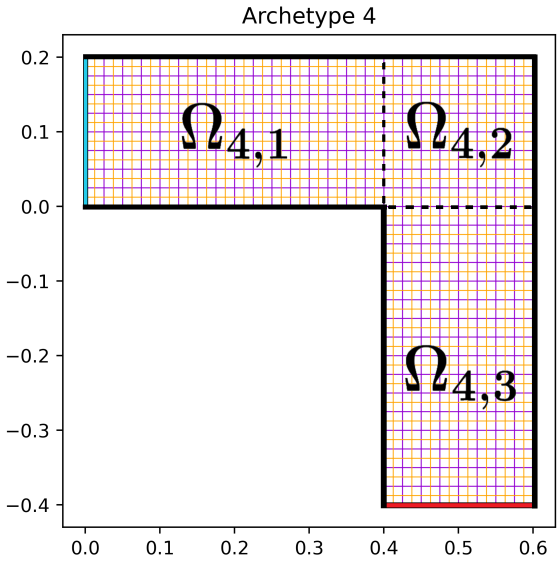

Figure 10: *Archetype 4 – The right-corner pipe*: Each purple square represents a Q_2/Q_1 Taylor-Hood element. The blue edge is the inlet, the black edges are the walls, and the red edge is the outlet.

The right-corner pipe is as one would expect identical to the left-corner pipe, only mirrored along the x-axis and shifted. Thus everything is done as in the previous section before changing the y-coordinates:

$$\begin{bmatrix} x \\ y \end{bmatrix}_{\Omega_4} = \begin{bmatrix} x \\ -y + 0.2 \end{bmatrix}_{\Omega_3}. \tag{4.18}$$

Note that a similar scheme is used when the rotation of an archetype is necessary:

$$\begin{bmatrix} x \\ y \end{bmatrix}_{\Omega_i}^{\pi/2} = \begin{bmatrix} 0 & -1 \\ 1 & 0 \end{bmatrix} \begin{bmatrix} x \\ y \end{bmatrix}_{\Omega_i}^{0}. \tag{4.19}$$

4.6 Archetype 5 – The partially blocked pipe

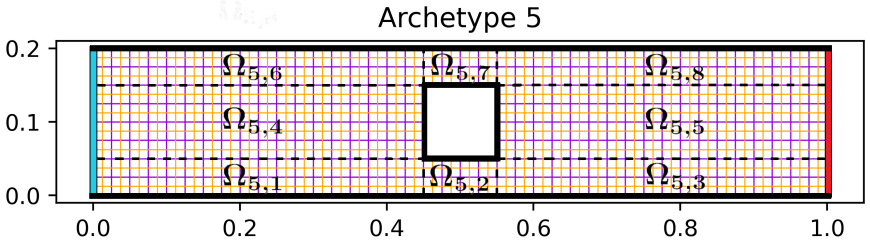

Figure 11: *Archetype 5 – The partially blocked pipe*: Each purple square represents a Q_2/Q_1 Taylor-Hood element. The blue edge is the inlet, the black edges are the walls, and the red edge is the outlet.

Due to the blockage in the middle of this pipe, this archetype is partitioned into eight subdomains. Let $\boldsymbol{\mu}_5 = [\mu^{(1)}, \mu^{(2)}, \mu^{(3)}]$ be our parameters, where $\mu^{(1)}$ controls the length before the blockage, $\mu^{(2)}$ the total width of the pipe, and $\mu^{(3)}$ the length after the blockage. Thus we need eight parametric mappings:

$$
\begin{aligned}
\boldsymbol{\Phi}_{\Omega_{5,1}}(x,y,\boldsymbol{\mu}_5) &= \begin{bmatrix} 1+\mu^{(1)} & 0 \\ 0 & 1+2\mu^{(2)} \end{bmatrix} \begin{bmatrix} x \\ y \end{bmatrix} - \begin{bmatrix} 0.45\mu^{(1)} \\ 0.1\mu^{(2)} \end{bmatrix}, \\
\boldsymbol{\Phi}_{\Omega_{5,2}}(x,y,\boldsymbol{\mu}_5) &= \begin{bmatrix} 1 & 0 \\ 0 & 1+2\mu^{(2)} \end{bmatrix} \begin{bmatrix} x \\ y \end{bmatrix} - \begin{bmatrix} 0 \\ 0.1\mu^{(2)} \end{bmatrix}, \\
\boldsymbol{\Phi}_{\Omega_{5,3}}(x,y,\boldsymbol{\mu}_5) &= \begin{bmatrix} 1+\mu^{(3)} & 0 \\ 0 & 1+2\mu^{(2)} \end{bmatrix} \begin{bmatrix} x \\ y \end{bmatrix} - \begin{bmatrix} 0.55\mu^{(3)} \\ 0.1\mu^{(2)} \end{bmatrix}, \\
\boldsymbol{\Phi}_{\Omega_{5,4}}(x,y,\boldsymbol{\mu}_5) &= \begin{bmatrix} 1+\mu^{(1)} & 0 \\ 0 & 1 \end{bmatrix} \begin{bmatrix} x \\ y \end{bmatrix} - \begin{bmatrix} 0.45\mu^{(1)} \\ 0 \end{bmatrix}, \\
\boldsymbol{\Phi}_{\Omega_{5,5}}(x,y,\boldsymbol{\mu}_5) &= \begin{bmatrix} 1+\mu^{(3)} & 0 \\ 0 & 1 \end{bmatrix} \begin{bmatrix} x \\ y \end{bmatrix} - \begin{bmatrix} 0.55\mu^{(3)} \\ 0 \end{bmatrix}, \\
\boldsymbol{\Phi}_{\Omega_{5,6}}(x,y,\boldsymbol{\mu}_5) &= \begin{bmatrix} 1+\mu^{(1)} & 0 \\ 0 & 1+2\mu^{(2)} \end{bmatrix} \begin{bmatrix} x \\ y \end{bmatrix} - \begin{bmatrix} 0.45\mu^{(1)} \\ 0.3\mu^{(2)} \end{bmatrix}, \\
\boldsymbol{\Phi}_{\Omega_{5,7}}(x,y,\boldsymbol{\mu}_5) &= \begin{bmatrix} 1 & 0 \\ 0 & 1+2\mu^{(2)} \end{bmatrix} \begin{bmatrix} x \\ y \end{bmatrix} - \begin{bmatrix} 0 \\ 0.3\mu^{(2)} \end{bmatrix}, \\
\boldsymbol{\Phi}_{\Omega_{5,8}}(x,y,\boldsymbol{\mu}_5) &= \begin{bmatrix} 1+\mu^{(3)} & 0 \\ 0 & 1+2\mu^{(2)} \end{bmatrix} \begin{bmatrix} x \\ y \end{bmatrix} - \begin{bmatrix} 0.55\mu^{(3)} \\ 0.3\mu^{(2)} \end{bmatrix}.
\end{aligned}
\tag{4.20}
$$

The eight mappings results in 32 affine functions and bilinear forms, which can be found using equation (4.5). Mapping the lifting function to the reference domain results in three distinct equations, due to the fact that the inlet covers three different subdomains:

$$
\begin{aligned}
g_x(y', \boldsymbol{\mu}_5) = \quad & \frac{100\mu_a}{(1+\mu^{(2)})^2}\big(0.2 + 0.1\mu^{(2)} - y'\big)\big(y' + 0.1\mu^{(2)}\big), \\
g_x(y, \boldsymbol{\mu}_5) = & \begin{cases} \dfrac{100\mu_a}{(1+\mu^{(2)})^2}\big(0.2 + 0.2\mu^{(2)} - (1+2\mu^{(2)})y\big)(1+2\mu^{(2)})y, & y \in \Omega_{5,1}, \\ \dfrac{100\mu_a}{(1+\mu^{(2)})^2}\big(0.2 + 0.1\mu^{(2)} - y\big)\big(y + 0.1\mu^{(2)}\big), & y \in \Omega_{5,4}, \\ \dfrac{100\mu_a}{(1+\mu^{(2)})^2}\big(0.2 + 0.4\mu^{(2)} - (1+2\mu^{(2)})y\big)\big((1+2\mu^{(2)})y - 0.2\mu^{(2)}\big), & y \in \Omega_{5,6}. \end{cases}
\end{aligned}
\tag{4.21}
$$

4.7 Archetype 6 – The contraction pipe

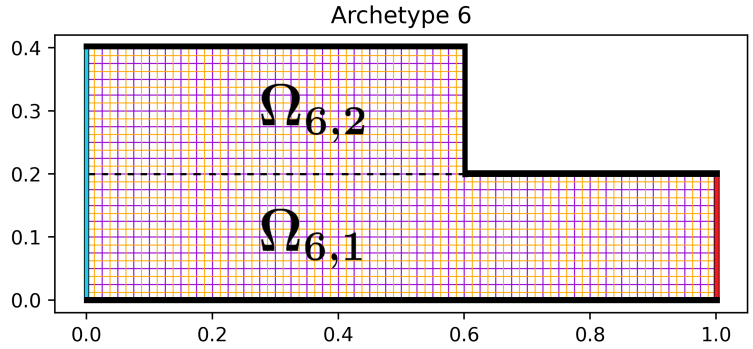

Figure 12: *Archetype 6 – The contraction pipe*: Each purple square represents a Q_2/Q_1 Taylor-Hood element. The blue edge is the inlet, the black edges are the walls, and the red edge is the outlet.

The contraction pipe is partitioned into two subdomains, and we wish to control the width of the inlet and the outlet independently. Let $\boldsymbol{\mu}_6 = [\mu^{(1)}, \mu^{(2)}]$ control the width of the outlet and the inlet, respectively. This results in the two parametric mappings

$$\begin{aligned} \boldsymbol{\Phi}_{\Omega_{6,1}}(x, y, \boldsymbol{\mu}_6) &= \begin{bmatrix} 1 & 0 \\ 0 & 1+\mu^{(1)} \end{bmatrix} \begin{bmatrix} x \\ y \end{bmatrix}, \\ \boldsymbol{\Phi}_{\Omega_{6,2}}(x, y, \boldsymbol{\mu}_6) &= \begin{bmatrix} 1 & 0 \\ 0 & 2\mu^{(2)}+1-\mu^{(1)} \end{bmatrix} \begin{bmatrix} x \\ y \end{bmatrix} + \begin{bmatrix} 0 \\ 0.4(\mu^{(1)}-\mu^{(2)}) \end{bmatrix}, \end{aligned} \tag{4.22}$$

and a total of eight affine functions and bilinear forms. The resulting lifting functions are

$$\begin{aligned} g_x(y', \boldsymbol{\mu}_6) = &\quad \frac{25\mu_a}{(1+\mu^{(2)})^2}\big(0.4(1+\mu^{(2)}) - y'\big)y', \\ g_x(y, \boldsymbol{\mu}_6) = &\begin{cases} \dfrac{25\mu_a}{(1+\mu^{(2)})^2}\big(0.4(1+\mu^{(2)}) - (1+\mu^{(1)})y\big)(1+\mu^{(1)})y, & y \in \Omega_{6,1}, \\ \dfrac{25\mu_a}{(1+\mu^{(2)})^2}\big((2\mu^{(2)}+1-\mu^{(1)})(0.4-y)\big)\big((2\mu^{(2)}+1-\mu^{(1)})y + 0.4(\mu^{(1)}-\mu^{(2)})\big), & y \in \Omega_{6,2}. \end{cases} \end{aligned} \tag{4.23}$$

4.8 Archetype 7 – The expansion pipe

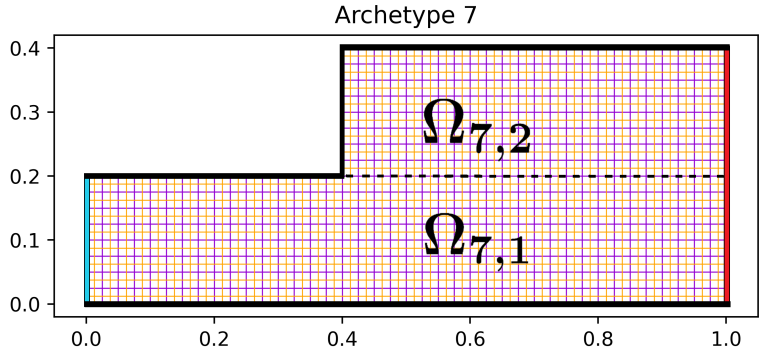

Figure 13: *Archetype 7 – The expansion pipe*: Each purple square represents a Q_2/Q_1 Taylor-Hood element. The blue edge is the inlet, the black edges are the walls, and the red edge is the outlet.

Since this archetype is essentially the mirrored version of the previous archetype, the mappings, affine functions and bilinear forms are the same. Note that here $\mu^{(1)}$ controls the width of the inlet, and $\mu^{(2)}$ the outlet. The width of the inlet on the reference domain is also different, resulting in different lifting functions. Also the inlet now only covers one of the domains, thus we only need one lifting function on the reference domain:

$$\begin{aligned} g_x(y', \boldsymbol{\mu}_7) &= \frac{100\mu_a}{(1+\mu^{(1)})^2}\big(0.2(1+\mu^{(1)}) - y'\big)y', \\ g_x(y, \boldsymbol{\mu}_7) &= 100\mu_a\big(0.2 - y\big)y. \end{aligned} \tag{4.24}$$

5 Connecting the archetypes

With our recently constructed library of reduced archetypes, we turn to the next challenge: Connecting the archetypes to assemble the desired system [39].

To achieve this we must be able to connect the outlet of the previous archetype to the inlet of the next archetype in our system. Recall that for each archetype, the amplitude of the inlet velocity are determined by one parameter, μ_a. Whereas the width of the inlet and the outlet are controlled by (typically) two separate parameters, say μ_{in} and μ_{out}. The general form of our velocity parabola is then

$$g_x = \frac{4\mu_a}{b^2(1+\mu_{\text{in}})^2}\big(b(1+\mu_{\text{in}}) - y\big)y. \tag{5.1}$$

First we require that the width of the previous outlet matches the width of the next inlet, that is

$$\hat{b}_i(1+\mu_{i,\text{out}}) = b_j(1+\mu_{j,\text{in}}), \tag{5.2}$$

for adjacent archetypes i, j (where archetype i precedes j). Here $b_i, \hat{b}_i$ denotes the width of the inlet and outlet of archetype i, respectively. Then we use the discrete velocity solution at the preceding outlet boundary to determine the amplitude of the lifting function for the following archetype. This can be done in a multitude of ways; we use a least-squares algorithm to fit a second-degree polynomial to the preceding outlet boundary datum, and use the resulting polynomial to calculate the average velocity of the fluid leaving the outlet, as well as the volume flow/flux.

$$u_{x,\text{avg}}|_{\Gamma_{\text{i,out}}} = \frac{1}{\hat{b_i}(1+\mu_{i,\text{out}})}\int_0^{\hat{b_i}(1+\mu_{i,\text{out}})} \alpha_i y^2 + \beta_i y \, dy = \frac{\alpha_i}{3}\hat{b_i}^2(1+\mu_{i,\text{out}})^2 + \frac{\beta_i}{2}\hat{b_i}(1+\mu_{i,\text{out}}), \tag{5.3}$$

where α_i, β_i are obtained from the least-squares algorithm. The amplitude of the outlet velocity parabola and the volume flow V_i is then

$$\begin{aligned} u_{x,\text{max}} &= \frac{3}{2}u_{x,\text{avg}}, \\ V_i &= u_{x,\text{avg}}\hat{b_i}(1+\mu_{i,\text{out}}). \end{aligned} \tag{5.4}$$

This amplitude is then used as the amplitude for the following archetype inlet velocity profile, $\mu_{j,a} = u_{x,\text{max}}|_{\Gamma_{\text{i,out}}}$. Additionally the volume flow V_i enables us to monitor to which degree mass is conserved in the system.

For this approach to be accurate, we must also make some additional assumptions: The walls leading up to the outlet must be parallel, ensuring a 90 degree angle with the outlet. This justifies the assumption that the outlet velocity is one-dimensional, hence also justifying a one-dimensional inlet velocity for the following

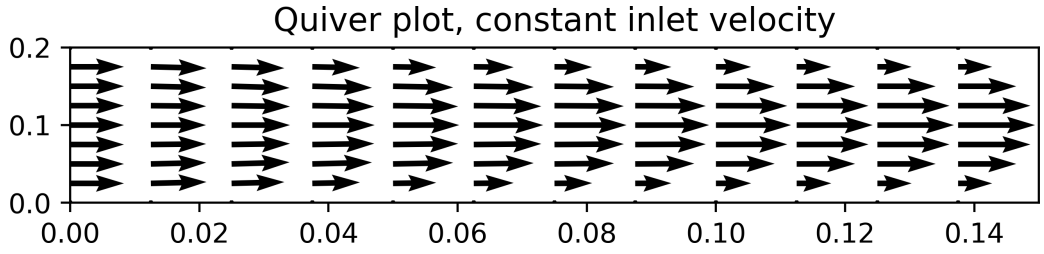

Figure 14: *Archetype 0 – The straight pipe*: An example of how a constant inlet velocity develops its parabolar shape. The velocity profile appears fully developed at $x = 0.15$.

archetype. In addition, this makes the pressure gradient consistent with the imposed boundary conditions: $u_y = 0$ implies $\frac{\partial p}{\partial y} = 0$. In relation to this we must also allow the flow to fully develop before and after each connection boundary, to ensure that the assumption of a parabolic velocity-profile holds (see Figure 14). Most of these assumptions could however be avoided had we used a more general approach such as in [40] [41] [42] [43]. In short it would be necessary to train every possible pair of archetypes for each of the N_n selected parameters [44] [45], however this is beyond the scope of this thesis.

6 Results

We begin this section by showing the solution to the Stokes' equation on each of the archetypes in their initial state, before changing some of the parameters. All the figures shown are ROM's as they are indistinguishable from their FOM counterparts. Instead we include a figure showing the difference between the FOM and the ROM for each archetype. Note that the scale of the color-bar on each figure may vary. Note that the amplitude of the inlet velocity μ_a is the last parameter in every μ-list. We omit the results from archetype 4, as they are identical to those from archetype 3, only mirrored about the x-axis. In addition we show the averaged relative differences between the FOM's and the ROM's as the dimension of the reduced space increases, measured in L^2 norm and H^1 semi-norm for the velocities, and L^2 norm for the pressure. A table comparing relevant computational details between the ROM and the FOM is also shown for each archetype. The ROM's in these tables were created using the POD algorithm introduced in Section 2.3.2. Following the sections on each individual archetype, we discuss noteworthy observations for each archetype.

Once each archetype have been presented and discussed, we turn to our component based approach. We investigate the error between two connected ROM archetypes relative to a full order single-domain approach, and consider how much the connection contributes to the relative error.

Finally we present three example systems, constructed from multiple archetypes. We analyse the loss of volume flow through the system, relative to to the inlet flow. Due to the complexity of the pipe systems, no equivalent FOMs were created for comparison, as this proved to be too time consuming.

6.1 Archetype 0

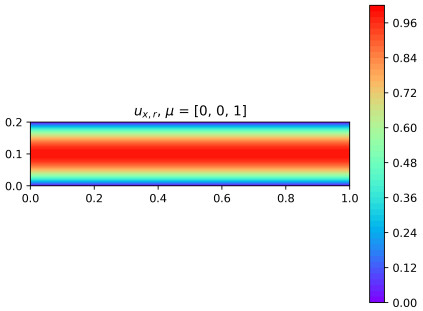

(a) ROM x-velocity, $\boldsymbol{\mu} = [0, 0, 1]$

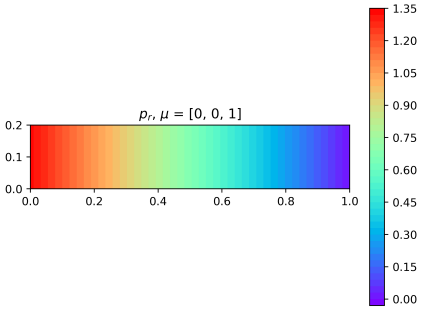

(b) ROM pressure, $\boldsymbol{\mu} = [0, 0, 1]$

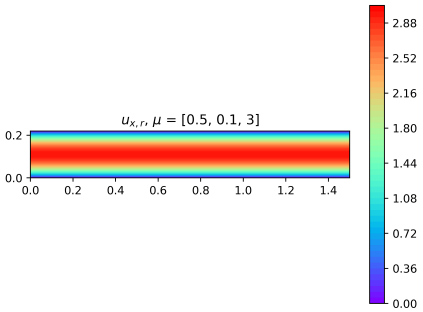

(c) ROM x-velocity, $\boldsymbol{\mu} = [.5, .1, 3]$

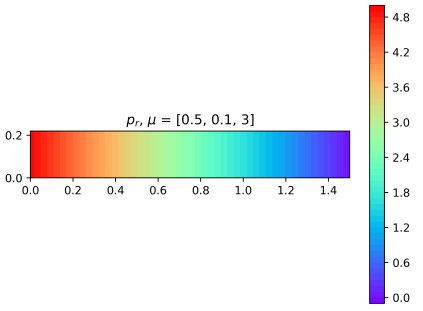

(d) ROM pressure, $\boldsymbol{\mu} = [.5, .1, 3]$

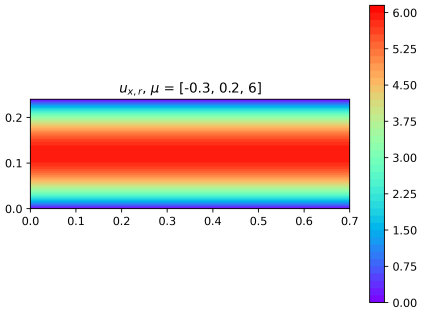

(e) ROM x-velocity, $\boldsymbol{\mu} = [-.3, .2, 6]$

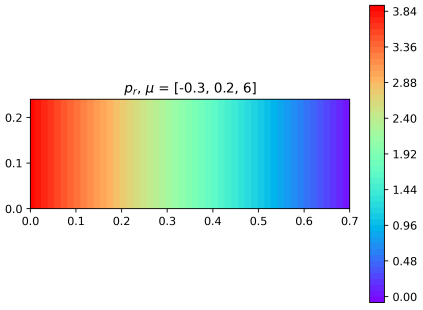

(f) ROM pressure, $\boldsymbol{\mu} = [-.3, .2, 6]$

Figure 15: *Archetype 0*: Three example ROM solutions. The y-velocities are zero, hence not shown here.

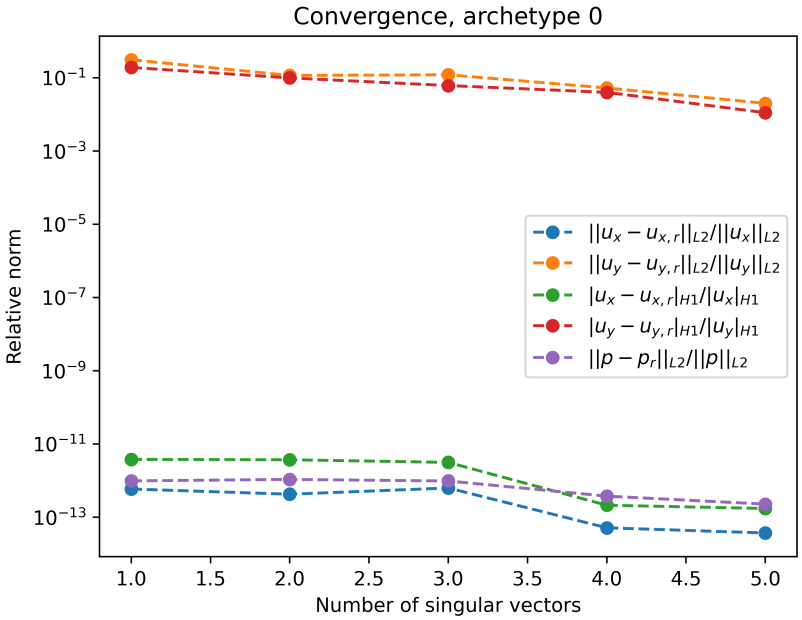

Figure 16: *Archetype 0*: Relative differences between the FOM's and the ROM's, averaged over all $4^3 = 64$ snapshots. The relative norms of the y-velocities are rather large since the y-velocities are theoretically zero, thus $||u_y - u_{y,h}||/||u_y|| \approx 0/0$. Note that machine precision is achieved for the other quantities with only one basis vector, due to the simplicity of this archetype.

FOM		ROM	
Total dofs:	11297	Total dofs:	6
Velocity dofs:	$2 \cdot 4960$	Velocity dofs:	$2 \cdot 2$
Pressure dofs:	1377	Pressure dofs:	2
Solution time:	$\sim$ 2.2 s.	Solution time:	$\sim$ 7 ms.
Snapshots:	64	ε_{POD}:	10^{-4}

Table 1: *Archetype 0*: Computational details. ROM dofs were chosen with the POD algorithm.

6.2 Archetype 1

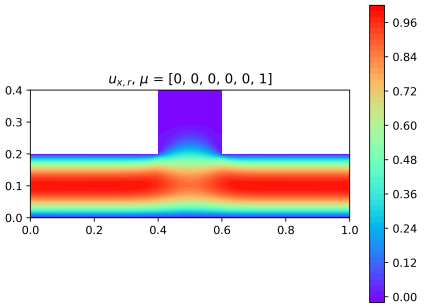

(a) ROM x-velocity, $\boldsymbol{\mu} = [0, 0, 0, 0, 0, 1]$

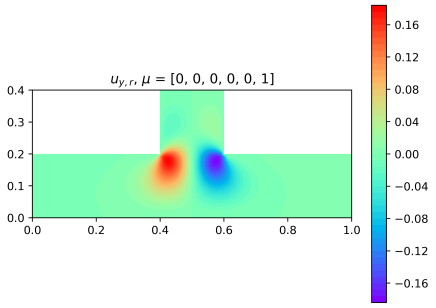

(b) ROM y-velocity, $\boldsymbol{\mu} = [0, 0, 0, 0, 0, 1]$

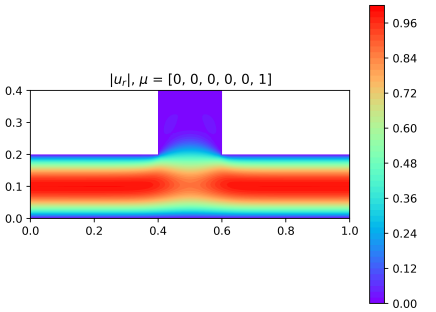

(c) ROM absolute velocity, $\boldsymbol{\mu} = [0, 0, 0, 0, 0, 1]$

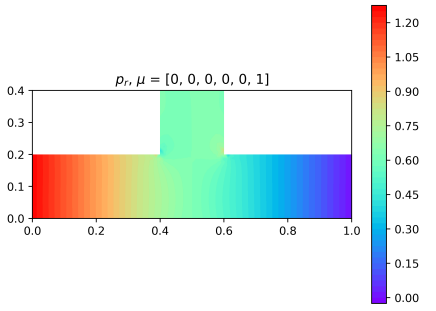

(d) ROM pressure, $\boldsymbol{\mu} = [0, 0, 0, 0, 0, 1]$

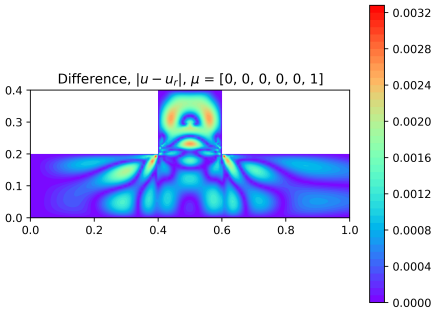

(e) ROM and FOM, absolute velocity difference.

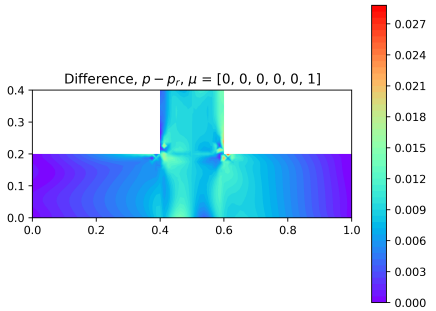

(f) ROM and FOM, pressure difference.

Figure 17: *Archetype 1*: The initial ROM solutions, and the difference between the FOM and the ROM.

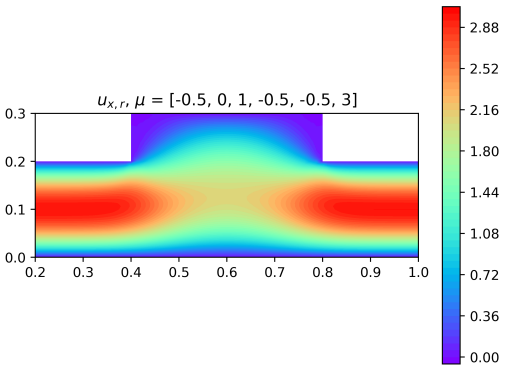

(a) ROM x-velocity, $\boldsymbol{\mu} = [-.5, 0, 1, -.5, -.5, 1]$

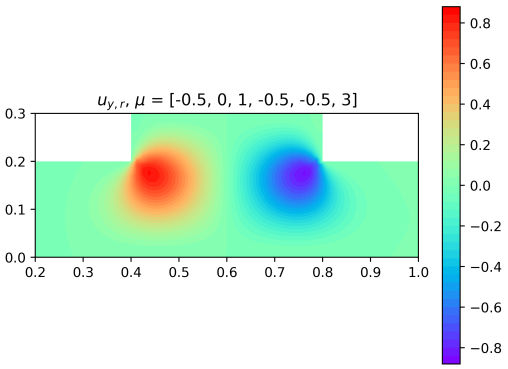

(b) ROM y-velocity, $\boldsymbol{\mu} = [-.5, 0, 1, -.5, -.5, 1]$

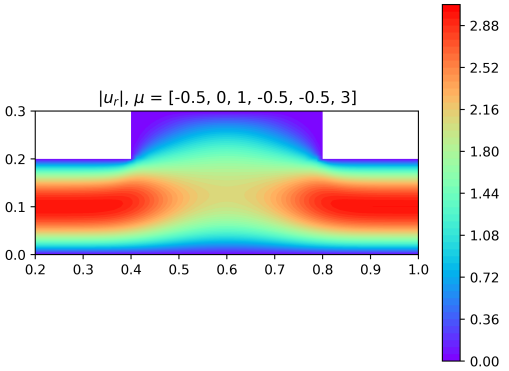

(c) ROM absolute velocity, $\boldsymbol{\mu} = [-.5, 0, 1, -.5, -.5, 1]$

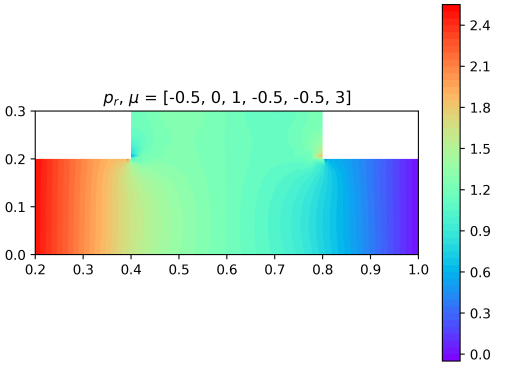

(d) ROM pressure, $\boldsymbol{\mu} = [-.5, 0, 1, -.5, -.5, 1]$

Figure 18: *Archetype 1*: ROM solutions for a case with a wide closed cavitation and a short inlet and outlet.

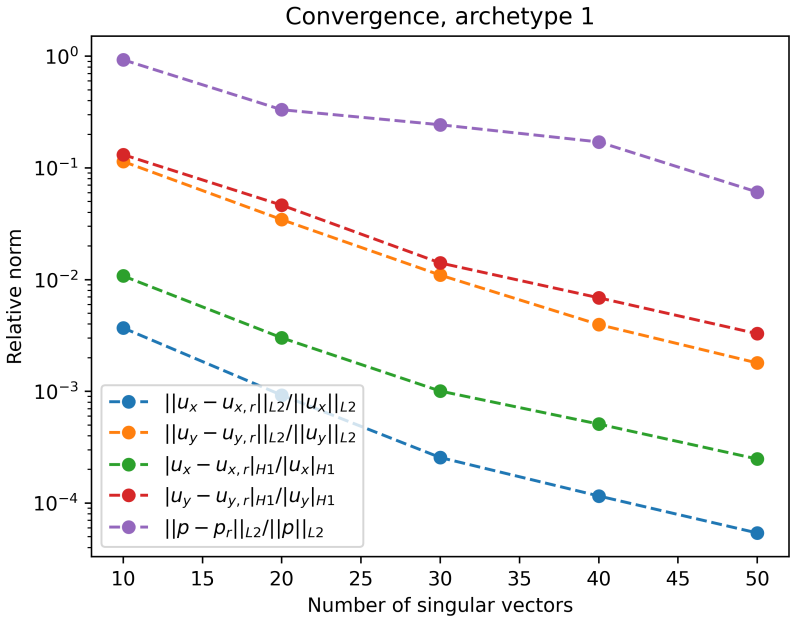

Figure 19: *Archetype 1*: Relative differences between the FOM's and the ROM's, averaged over all $3^6 = 729$ snapshots.

FOM		ROM	
Total dofs:	13553	Total dofs:	57
Velocity dofs:	$2 \cdot 5952$	Velocity dofs:	$2 \cdot 19$
Pressure dofs:	1649	Pressure dofs:	19
Solution time:	$\sim$ 11.2 s.	Solution time:	$\sim$ 20 ms.
Snapshots:	729	ε_{POD}:	10^{-4}

Table 2: *Archetype 1*: Computational details.ROM dofs were chosen with the POD algorithm.

6.3 Archetype 2

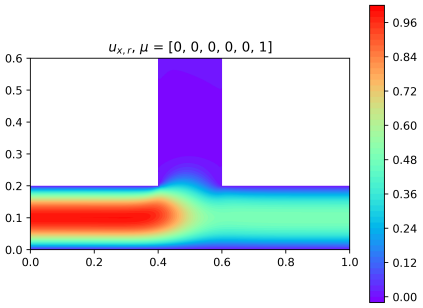

(a) ROM x-velocity, $\boldsymbol{\mu} = [0, 0, 0, 0, 0, 1]$

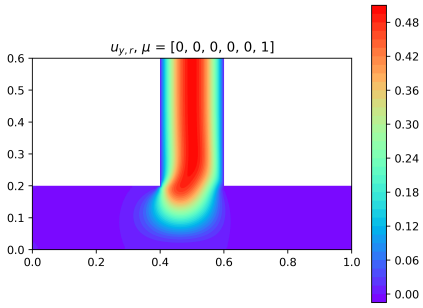

(b) ROM y-velocity, $\boldsymbol{\mu} = [0, 0, 0, 0, 0, 1]$

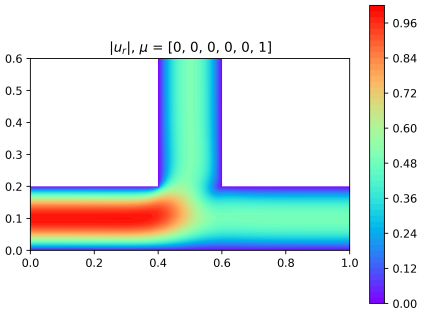

(c) ROM absolute velocity, $\boldsymbol{\mu} = [0, 0, 0, 0, 0, 1]$

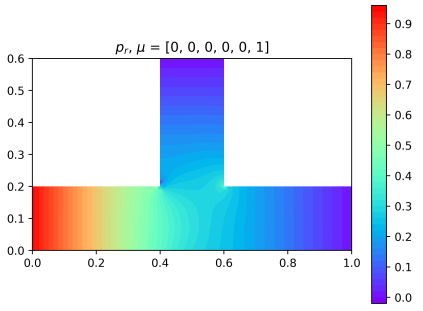

(d) ROM pressure, $\boldsymbol{\mu} = [0, 0, 0, 0, 0, 1]$

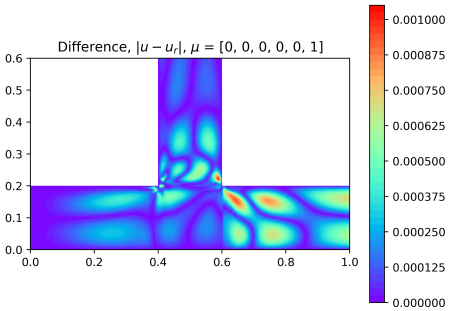

(e) ROM and FOM, absolute velocity difference.

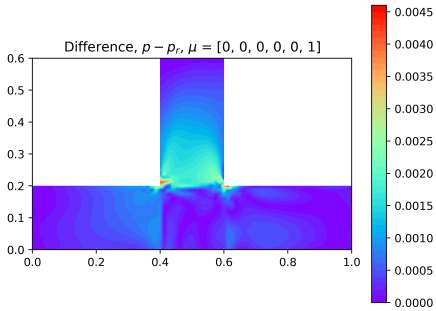

(f) ROM and FOM pressure difference.

Figure 20: *Archetype 2*: Initial ROM solutions, and the difference between the FOM and the ROM.

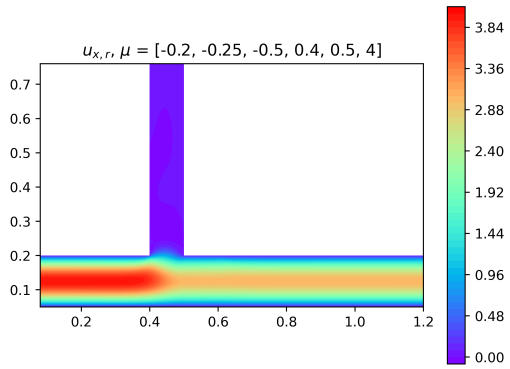

(a) ROM x-velocity, $\boldsymbol{\mu} = [-.2, -.25, -.5, .4, .5, 4]$

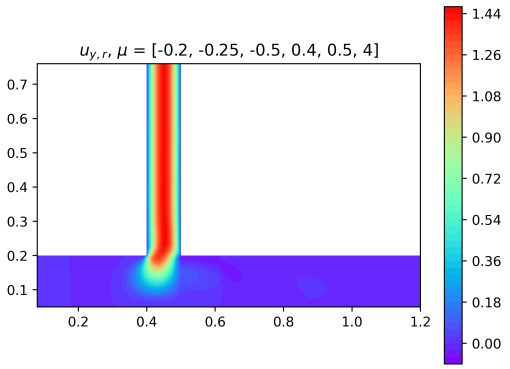

(b) ROM y-velocity, $\boldsymbol{\mu} = [-.2, -.25, -.5, .4, .5, 4]$

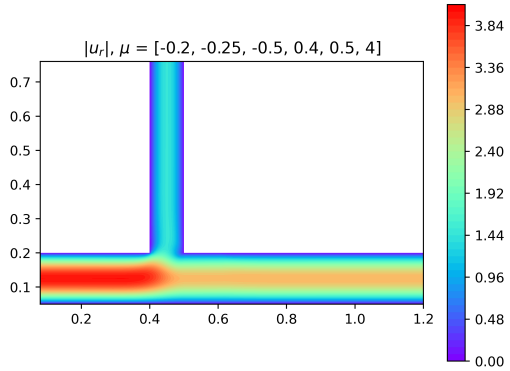

(c) ROM absolute velocity, $\boldsymbol{\mu} = [-.2, -.25, -.5, .4, .5, 4]$

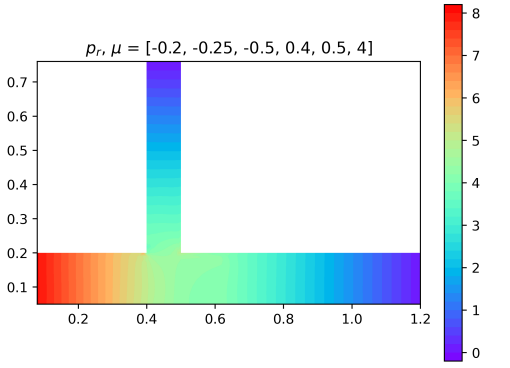

(d) ROM pressure, $\boldsymbol{\mu} = [-.2, -.25, -.5, .4, .5, 4]$

Figure 21: *Archetype 2*: ROM solutions for a case with narrow vertical outlet. Notice that the dominant flow occurs in the horizontal outlet pipe.

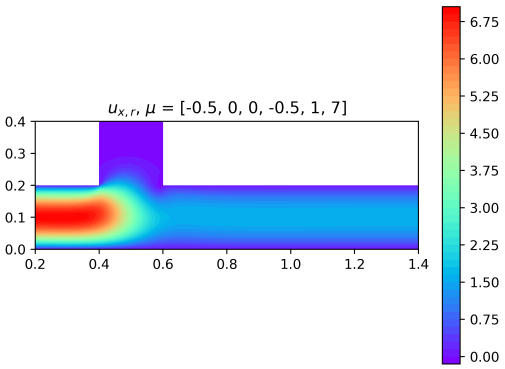

(a) ROM x-velocity, $\boldsymbol{\mu} = [-.5, 0, 0, -.5, 1, 7]$

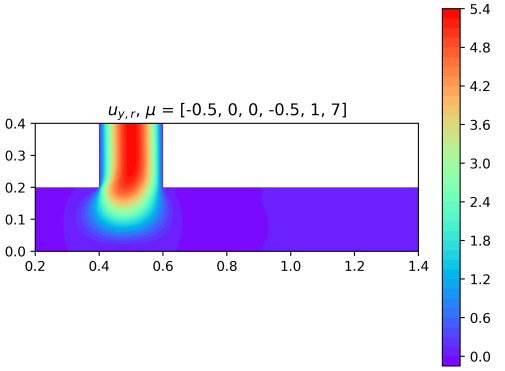

(b) ROM y-velocity, $\boldsymbol{\mu} = [-.5, 0, 0, -.5, 1, 7]$

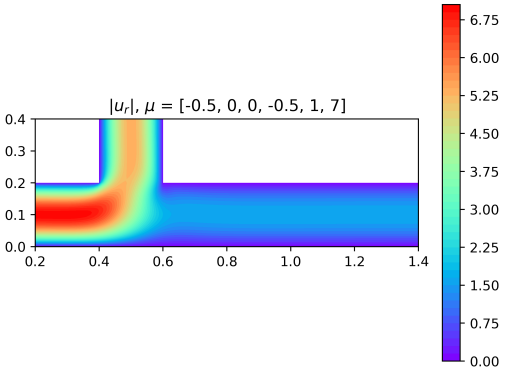

(c) ROM absolute velocity, $\boldsymbol{\mu} = [-.5, 0, 0, -.5, 1, 7]$

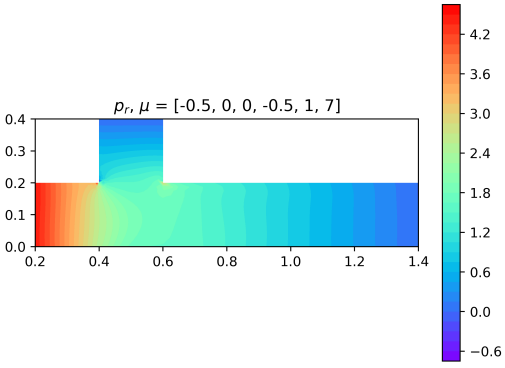

(d) ROM pressure, $\boldsymbol{\mu} = [-.5, 0, 0, -.5, 1, 7]$

Figure 22: *Archetype 2*: ROM solutions for a case with a short vertical outlet and a long horizontal outlet. Most of the flow occurs in the vertical outlet pipe, as the shorter pipe implies a larger pressure gradient.

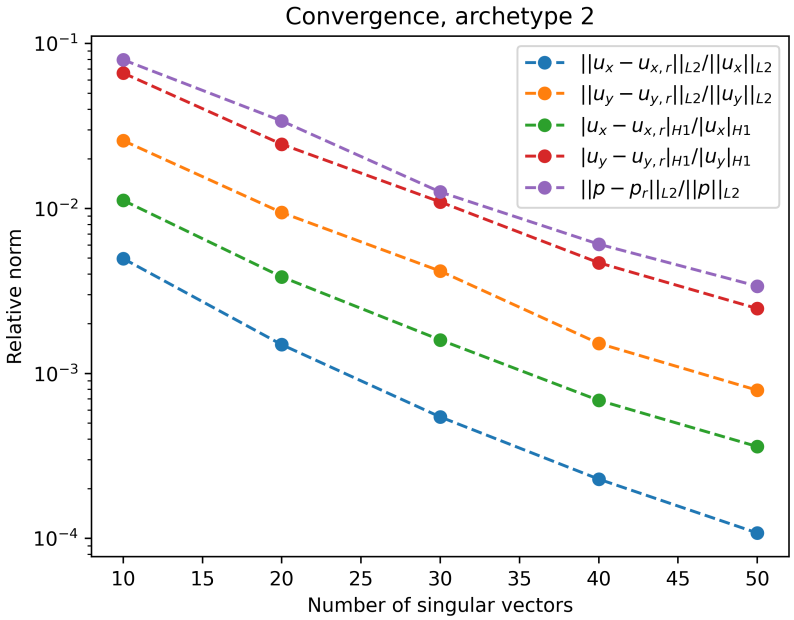

Figure 23: *Archetype 2*: Relative differences between the FOM's and the ROM's, averaged over all $3^6 = 729$ snapshots.

FOM		ROM	
Total dofs:	15871	Total dofs:	84
Velocity dofs:	$2 \cdot 6975$	Velocity dofs:	$2 \cdot 28$
Pressure dofs:	1921	Pressure dofs:	28
Solution time:	$\sim$ 14.9 s.	Solution time:	$\sim$ 22 ms.
Snapshots:	729	ε_{POD}:	10^{-4}

Table 3: *Archetype 2*: Computational details.ROM dofs were chosen with the POD algorithm.

6.4 Archetype 3

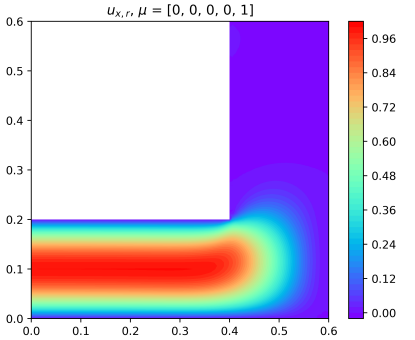

(a) ROM x-velocity, $\boldsymbol{\mu} = [0, 0, 0, 0, 1]$

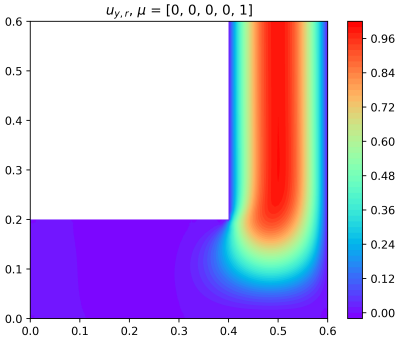

(b) ROM y-velocity, $\boldsymbol{\mu} = [0, 0, 0, 0, 1]$

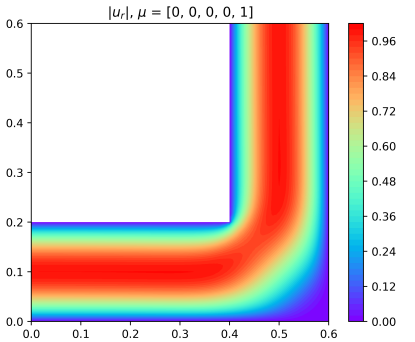

(c) ROM absolute velocity, $\boldsymbol{\mu} = [0, 0, 0, 0, 1]$

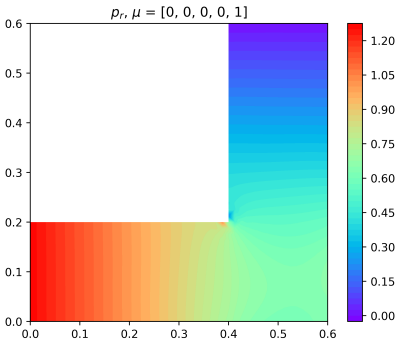

(d) ROM pressure, $\boldsymbol{\mu} = [0, 0, 0, 0, 1]$

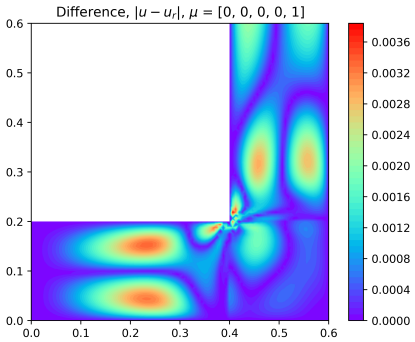

(e) ROM and FOM, absolute velocity difference.

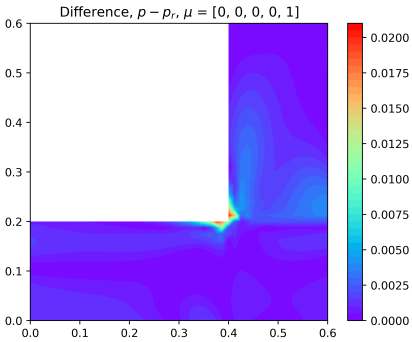

(f) ROM and FOM, pressure difference.

Figure 24: *Archetype 3*: Initial ROM solutions, and the difference between the FOM and the ROM.

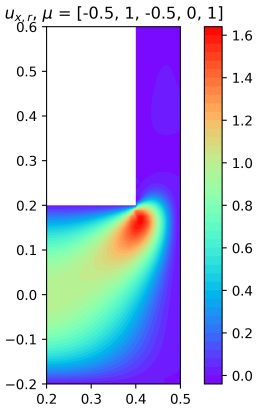

(a) ROM x-velocity, $\boldsymbol{\mu} = [-.5, 1, -.5, 0, 1]$

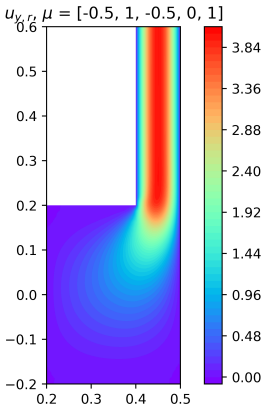

(b) ROM y-velocity, $\boldsymbol{\mu} = [-.5, 1, -.5, 0, 1]$

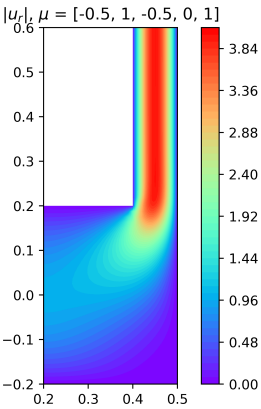

(c) ROM absolute velocity, $\boldsymbol{\mu} = [-.5, 1, -.5, 0, 1]$

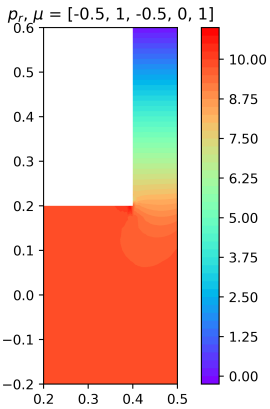

(d) ROM pressure, $\boldsymbol{\mu} = [-.5, 1, -.5, 0, 1]$

Figure 25: *Archetype 3*: ROM solutions for a case with a wide inlet and a narrow outlet. Note the velocity increase due to the contraction of the pipe.

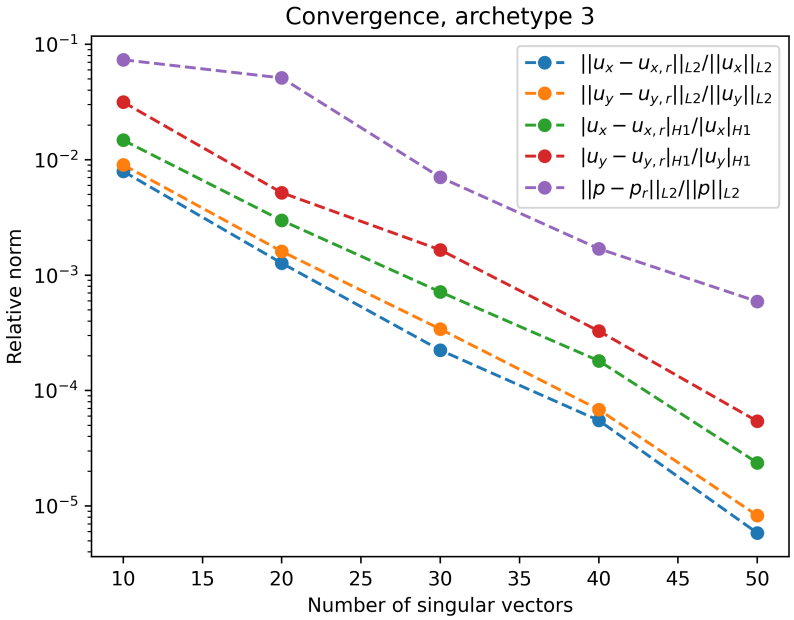

Figure 26: *Archetype 3*: Relative differences between the FOM's and the ROM's, averaged over all $3^5 = 243$ snapshots.

FOM		ROM	
Total dofs:	11297	Total dofs:	51
Velocity dofs:	$2 \cdot 4960$	Velocity dofs:	$2 \cdot 17$
Pressure dofs:	1377	Pressure dofs:	17
Solution time:	$\sim$ 6.2 s.	Solution time:	$\sim$ 16 ms.
Snapshots:	243	ε_{POD}:	10^{-4}

Table 4: *Archetype 3*: Computational details.ROM dofs were chosen with the POD algorithm.

6.5 Archetype 5

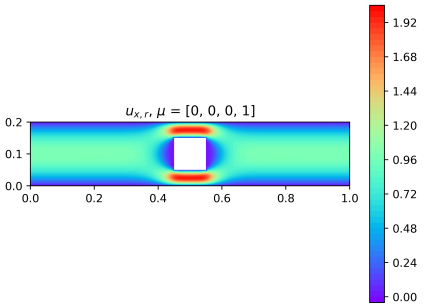

(a) ROM x-velocity, $\boldsymbol{\mu} = [0, 0, 0, 1]$

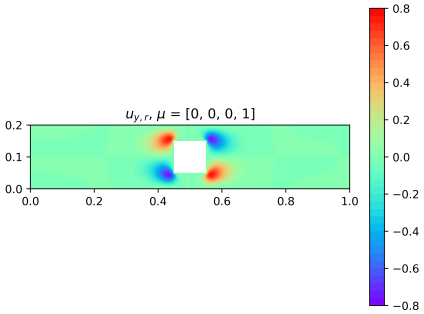

(b) ROM y-velocity, $\boldsymbol{\mu} = [0, 0, 0, 1]$

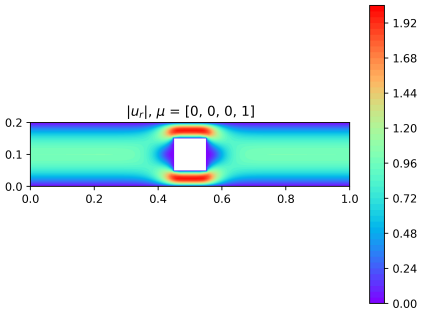

(c) ROM absolute velocity, $\boldsymbol{\mu} = [0, 0, 0, 1]$

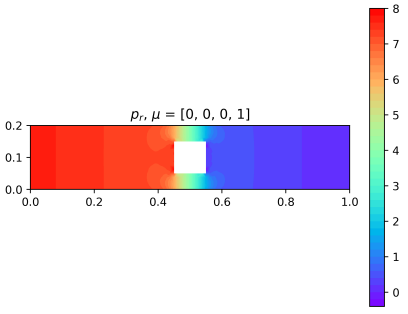

(d) ROM pressure, $\boldsymbol{\mu} = [0, 0, 0, 1]$

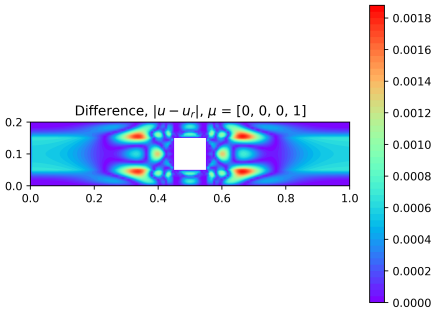

(e) ROM, and FOM, absolute velocity difference.

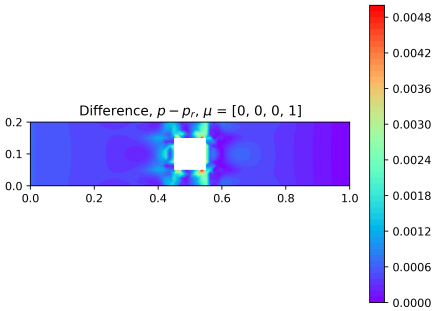

(f) ROM and FOM, pressure difference.

Figure 27: *Archetype 5*: Initial ROM solutions, and the difference between the FOM and the ROM.

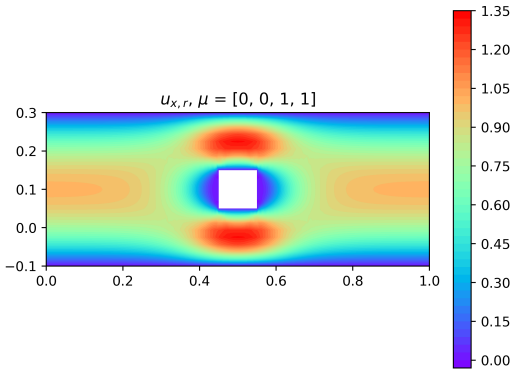

(a) ROM x-velocity, $\boldsymbol{\mu} = [0, 0, 1, 1]$

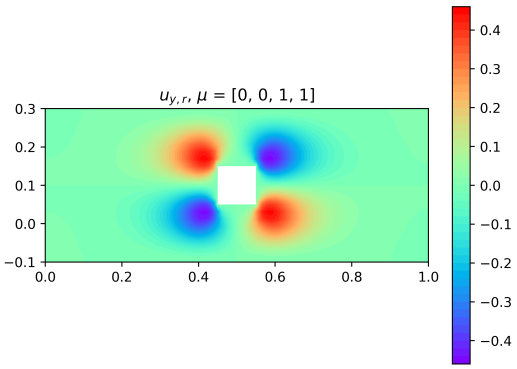

(b) ROM y-velocity, $\boldsymbol{\mu} = [0, 0, 1, 1]$

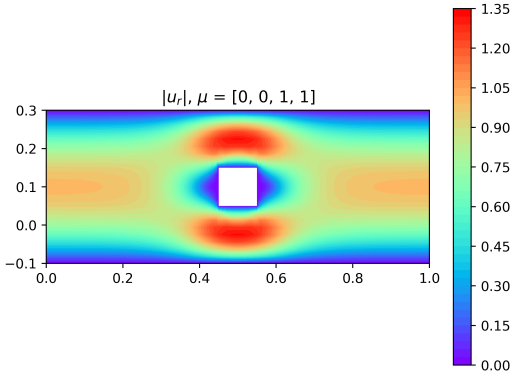

(c) ROM absolute velocity, $\boldsymbol{\mu} = [0, 0, 1, 1]$

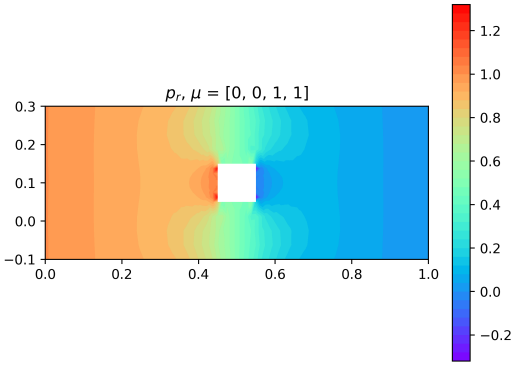

(d) ROM pressure, $\boldsymbol{\mu} = [0, 0, 1, 1]$

Figure 28: *Archetype 5*: ROM solutions for a case with a relatively wide inlet and outlet. Notice the decrease in pressure and maximum velocity compared to Figure 27.

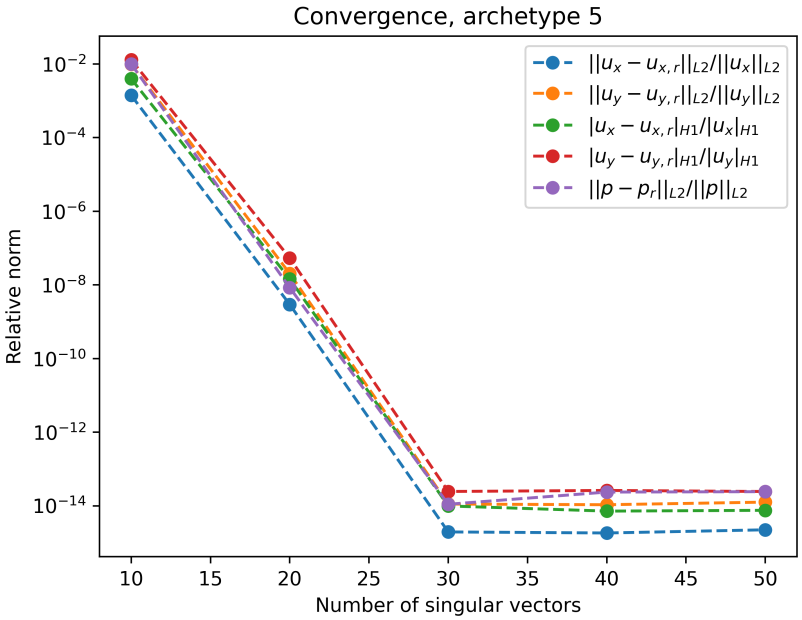

Figure 29: *Archetype 5*: Relative differences between the FOM's and the ROM's, averaged over all $4 \cdot 3^3 = 108$ snapshots.

FOM		ROM	
Total dofs:	10670	Total dofs:	33
Velocity dofs:	$2 \cdot 4671$	Velocity dofs:	$2 \cdot 11$
Pressure dofs:	1328	Pressure dofs:	11
Solution time:	$\sim$ 13.4 s.	Solution time:	$\sim$ 28 ms.
Snapshots:	108	ε_{POD}:	10^{-4}

Table 5: *Archetype 5*: Computational details. ROM dofs were chosen with the POD algorithm.

6.6 Archetype 6

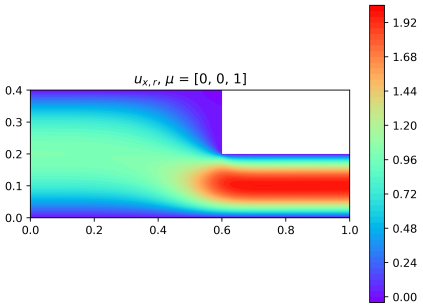

(a) ROM x-velocity, $\boldsymbol{\mu} = [0, 0, 1]$

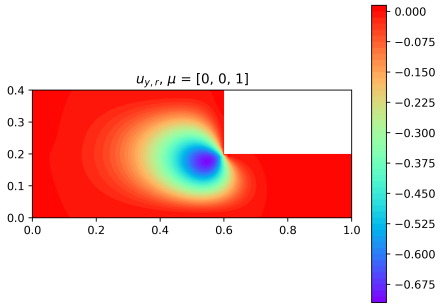

(b) ROM y-velocity, $\boldsymbol{\mu} = [0, 0, 1]$

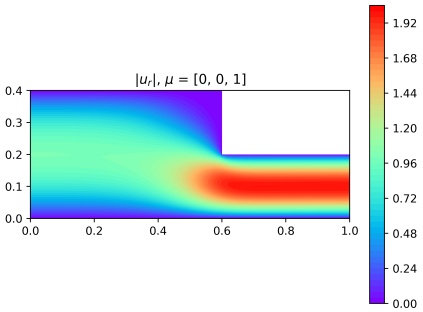

(c) ROM absolute velocity, $\boldsymbol{\mu} = [0, 0, 1]$

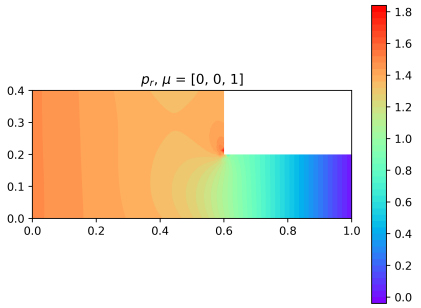

(d) ROM pressure, $\boldsymbol{\mu} = [0, 0, 1]$

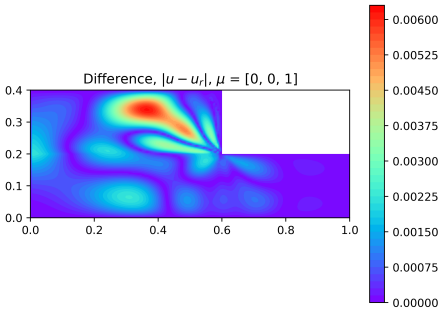

(e) ROM and FOM, absolute velocity difference.

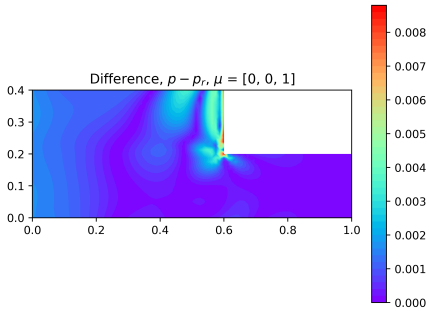

(f) ROM and FOM, pressure difference.

Figure 30: *Archetype 6*: Initial ROM solutions, and the difference between the FOM and the ROM.

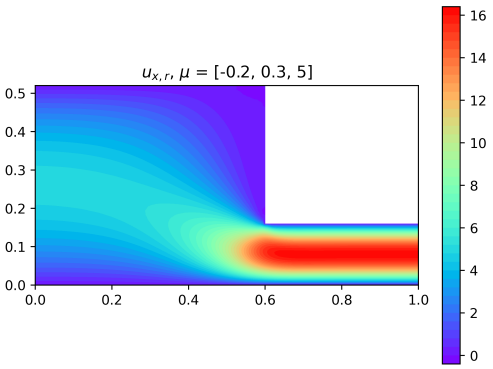

(a) ROM x-velocity, $\boldsymbol{\mu} = [-.2, .3, 5]$

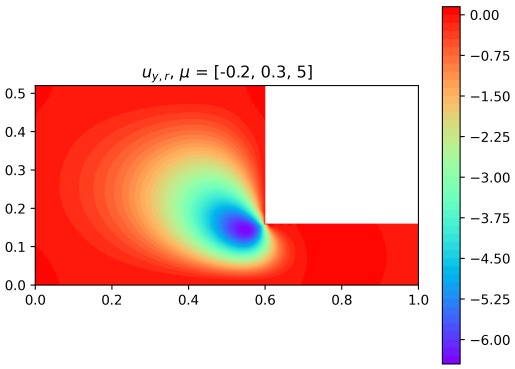

(b) ROM y-velocity, $\boldsymbol{\mu} = [-.2, .3, 5]$

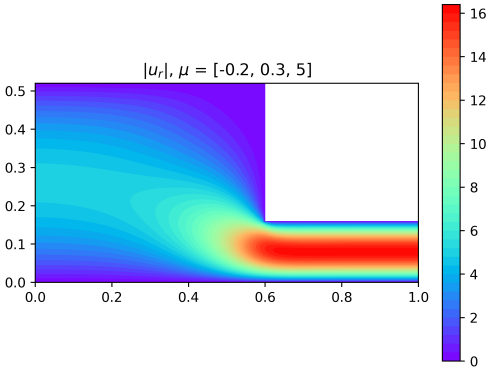

(c) ROM absolute velocity, $\boldsymbol{\mu} = [-.2, .3, 5]$

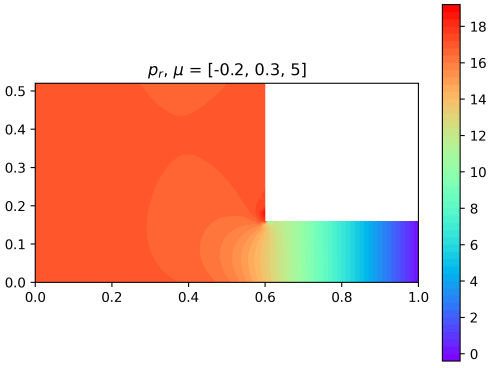

(d) ROM pressure, $\boldsymbol{\mu} = [-.2, .3, 5]$

Figure 31: *Archetype 6*: ROM solutions for a case with a wide inlet and a narrow outlet.

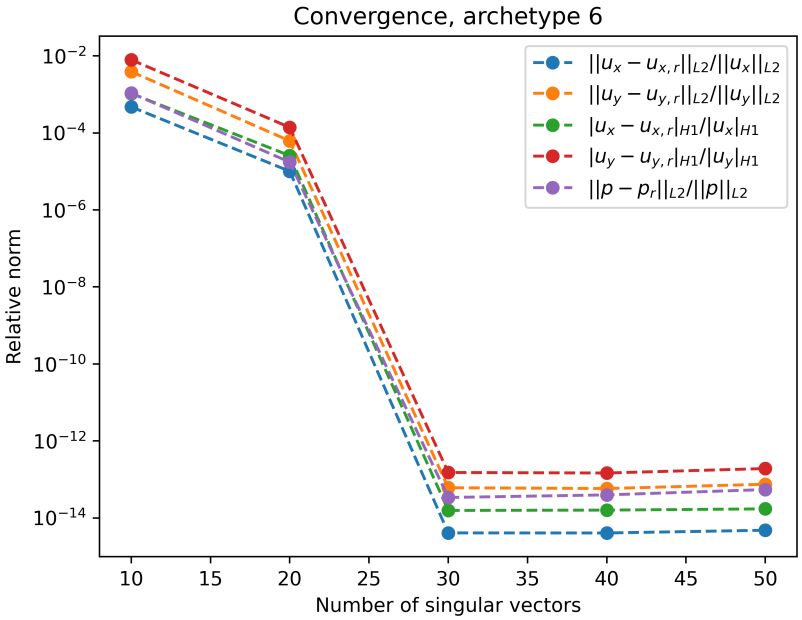

Figure 32: *Archetype 6*: Relative differences between the FOM's and the ROM's, averaged over all $4 \cdot 6^2 = 144$ snapshots.

FOM		ROM	
Total dofs:	18161	Total dofs:	27
Velocity dofs:	$2 \cdot 8000$	Velocity dofs:	$2 \cdot 9$
Pressure dofs:	2161	Pressure dofs:	9
Solution time:	$\sim$ 10.5 s.	Solution time:	$\sim$ 13 ms.
Snapshots:	144	ε_{POD}:	10^{-4}

Table 6: *Archetype 6*: Computational details. ROM dofs were chosen with the POD algorithm.

6.7 Archetype 7

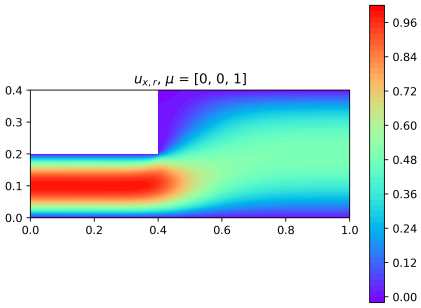

(a) ROM x-velocity, $\boldsymbol{\mu} = [0, 0, 1]$

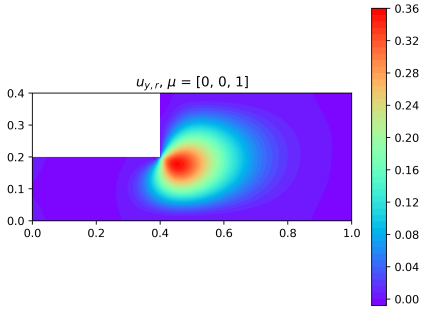

(b) ROM y-velocity, $\boldsymbol{\mu} = [0, 0, 1]$

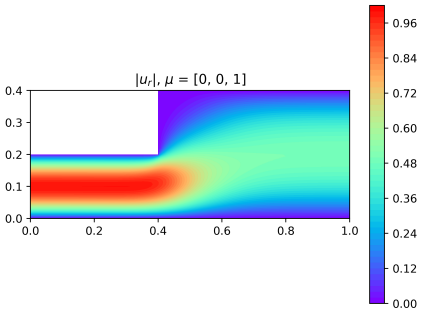

(c) ROM absolute velocity, $\boldsymbol{\mu} = [0, 0, 1]$

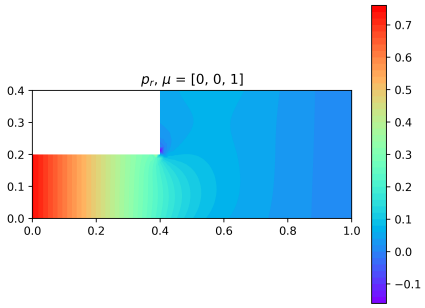

(d) ROM pressure, $\boldsymbol{\mu} = [0, 0, 1]$

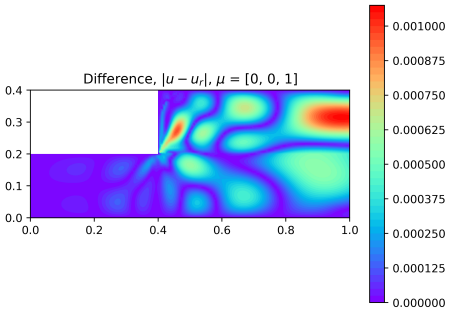

(e) ROM and FOM, absolute velocity difference.

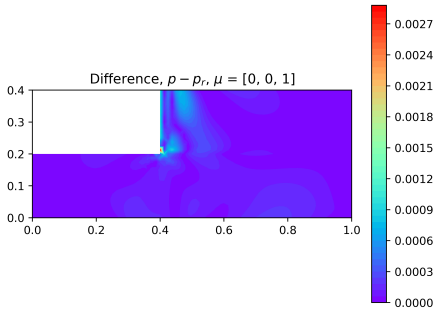

(f) ROM and FOM, pressure difference.

Figure 33: *Archetype 7*: Initial ROM solutions, and the difference between the FOM and the ROM.

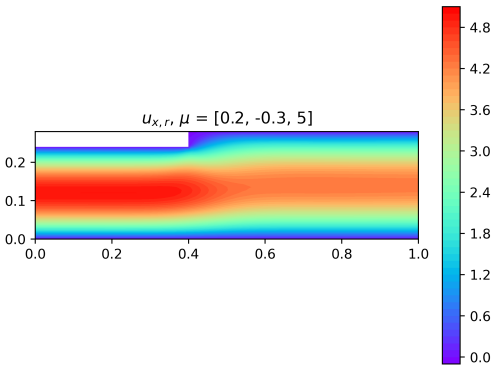

(a) ROM x-velocity, $\boldsymbol{\mu} = [.2, -.3, 5]$

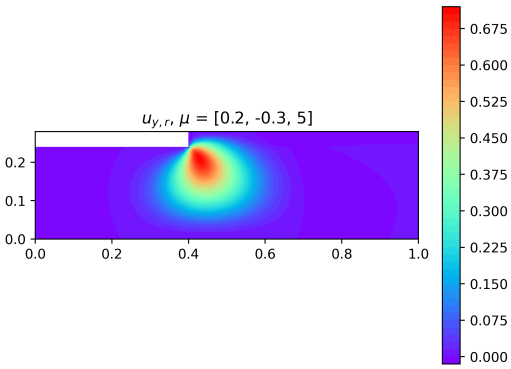

(b) ROM y-velocity, $\boldsymbol{\mu} = [.2, -.3, 5]$

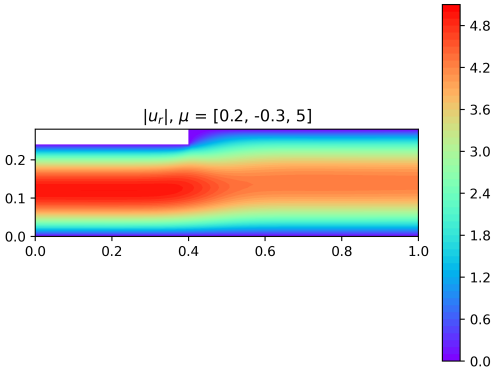

(c) ROM absolute velocity, $\boldsymbol{\mu} = [.2, -.3, 5]$

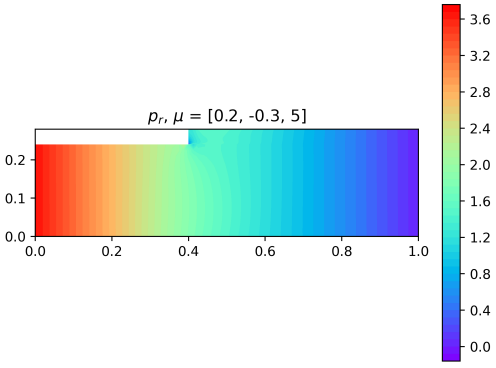

(d) ROM pressure, $\boldsymbol{\mu} = [.2, -.3, 5]$

Figure 34: *Archetype 7*: ROM solutions for a case with a relatively wide inlet.

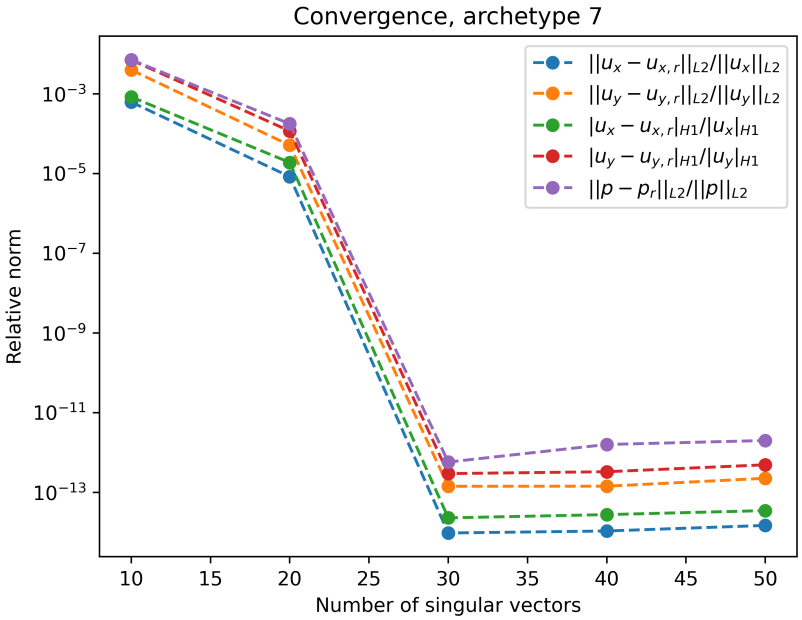

Figure 35: *Archetype 7*: Relative differences between the FOM's and the ROM's, averaged over all $4 \cdot 6^2 = 144$ snapshots.

FOM		ROM	
Total dofs:	18225	Total dofs:	30
Velocity dofs:	$2 \cdot 8032$	Velocity dofs:	$2 \cdot 10$
Pressure dofs:	2161	Pressure dofs:	10
Solution time:	$\sim$ 10.4 s.	Solution time:	$\sim$ 14 ms.
Snapshots:	144	ε_{POD}:	10^{-4}

Table 7: *Archetype 7*: Computational details. ROM dofs were chosen with the POD algorithm.

6.8 Noteworthy observations for the single components

Table 8 shows the relative norms of each archetype with their initial parameters. The dofs of the ROM were chosen by the POD-algorithm, with $\varepsilon_{\text{POD}} = 10^{-4}$. We will now discuss important observations from each of the archetypes:

- *Archetype 0*: The velocity of this archetype is strictly one-dimensional, thus the relative norm of the y-velocity is excluded from Figure 8.From Figure 16 we see that the average relative errors of the pressure and x-velocity reaches machine-precision with only one singular vector as basis for the RB-space, making this ROM extremely efficient.
- *Archetype 1*: From sub-figures 17e, 17f, it is clear that the closed bifurcation causes some error in the corners, especially for the pressure. This can also be seen in Figure 19, where the average pressure error is significantly higher than the average error in the velocities.
- *Archetype 2*: Compared to the previous archetype, opening the bifurcation results in a reduction in the average pressure error, see Figure 23. Most of the pressure error still accumulates from the corners, but to a much lesser extent. When changing the diameter and length of the two outlets, there is a notable change in the resulting volume flow. The dominant flow occurs in the shorter and wider outlet pipes, as one would expect. In the next section however we shall see that once the bifurcated pipe is connected to another archetype, our model fails, deeming this archetype infeasible with our way of handling the couplings.
- *Archetype 3*: From sub-Figure 24f, we notice once again that the majority of the pressure error occurs in the corner. Figure 26 shows that the average pressure error is notably larger than the average velocity errors, however not to the same extent as with archetype 1.
- *Archetype 4*: Since this archetype is the mirror-image of archetype 3, there are no additional notable observations.
- *Archetype 5*: From Figure 29 we see that this archetype converges much faster than every previous archetype except archetype 0. There are some notable spots close to the blockage where the most of the pressure error accumulates, similar to the other archetypes. Worth noting is that the partially blocked pipe induces higher pressures and greater velocities than its open counterpart, archetype 0 (see sub-figures 27a, 27d). We also observe from Figure 28 that as the relative width of the archetype increases, the maximum velocity and pressure decreases, as a smaller cross-section of the pipe is effectively blocked.
- *Archetype 6*: Figure 32 shows good convergence, achieving machine precision by 30 basis vectors. Figure 12 shows how the error propagates from the corners, as with the other archetypes.
- *Archetype 7*: Table 8 shows how this archetype is the most accurate apart from archetype 0. Machine precision is achieved by 30 basis vectors, with quite similar convergence results as archetype 6.

Archetype:	$\frac{\lvert u_x - u_{x,r}\rvert_{H^1}}{\lvert u_x\rvert_{H^1}}$	$\frac{\lvert u_y - u_{y,r}\rvert_{H^1}}{\lvert u_y\rvert_{H^1}}$	$\frac{\lvert\lvert p - p_r\rvert\rvert_{L^2}}{\lvert\lvert p\rvert\rvert_{L^2}}$
Ω_0	$1.57 \cdot 10^{-9}$	—	$5.84 \cdot 10^{-11}$
Ω_1	$3.29 \cdot 10^{-3}$	$3.65 \cdot 10^{-2}$	$9.76 \cdot 10^{-3}$
Ω_2	$1.04 \cdot 10^{-3}$	$3.46 \cdot 10^{-3}$	$1.74 \cdot 10^{-3}$
Ω_3	$3.75 \cdot 10^{-3}$	$6.99 \cdot 10^{-3}$	$2.50 \cdot 10^{-3}$
Ω_4	$3.75 \cdot 10^{-3}$	$6.99 \cdot 10^{-3}$	$2.50 \cdot 10^{-3}$
Ω_5	$1.12 \cdot 10^{-3}$	$3.94 \cdot 10^{-3}$	$1.31 \cdot 10^{-4}$
Ω_6	$3.06 \cdot 10^{-3}$	$1.56 \cdot 10^{-2}$	$1.01 \cdot 10^{-3}$
Ω_7	$8.44 \cdot 10^{-4}$	$7.36 \cdot 10^{-3}$	$6.25 \cdot 10^{-4}$

Table 8: Relative norms between the FOM and the ROM of all the archetypes, for their initial parameters. The dofs of the ROM were chosen with the POD algorithm.

6.9 Assembling the system, two-component error analysis

In this section we will look at difference plots and relative norms between two connected ROMs and an equivalent full order, *single domain* model. Norms are measured relative to the FOM, with the H^1-semi norm for velocities and the L^2-norm for pressure. The degrees of freedom for each archetype are once again chosen with the POD algorithm, hence they are the same as in the previous sections. We will look at five pairs of archetypes, to give an indication of how the error is compounded. Finally we discuss some noteworthy observations from each of the combinations.

6.9.1 Archetype 0 and 1

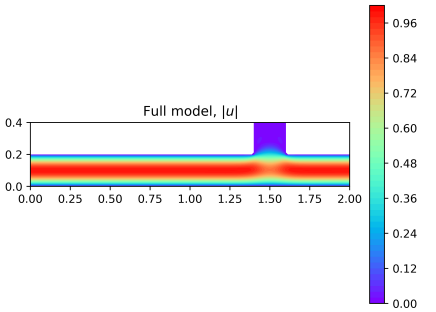

(a) Absolute velocity, FOM.

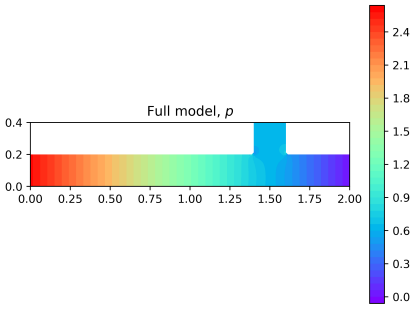

(b) Pressure, FOM.

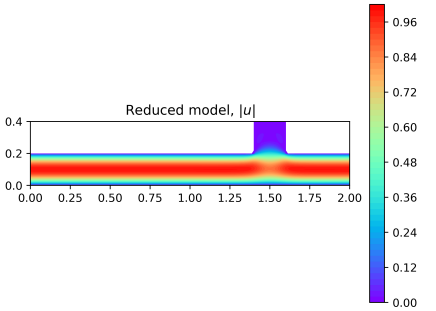

(c) Absolute velocity, ROM.

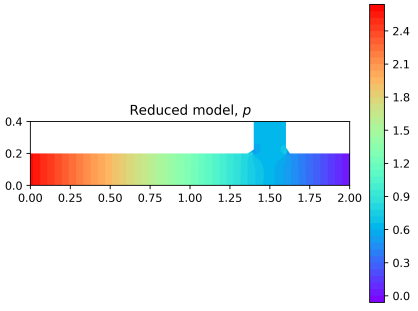

(d) Pressure, ROM.

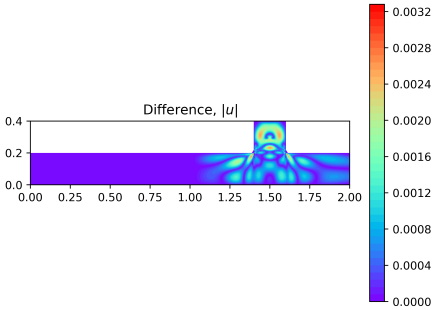

(e) Absolute velocity difference, FOM and ROM.

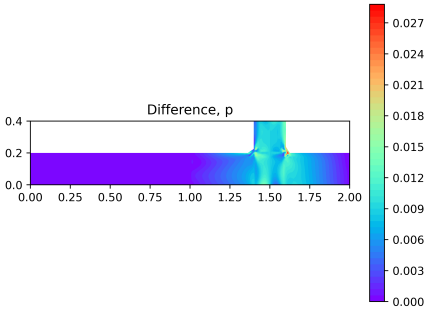

(f) Pressure difference , FOM and ROM.

Figure 36: *Archetype 0 and 1*: Absolute velocity, pressure, and the resulting error from combining the two archetypes.

6.9.2 Archetype 1 and 2

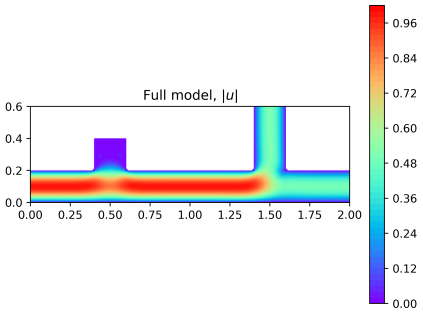

(a) Absolute velocity, FOM.

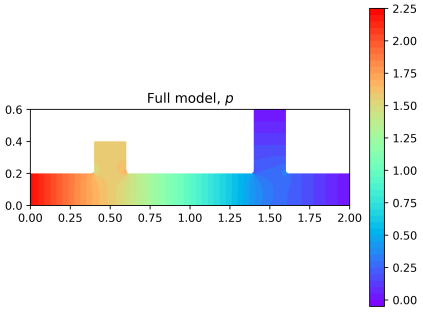

(b) Pressure, FOM.

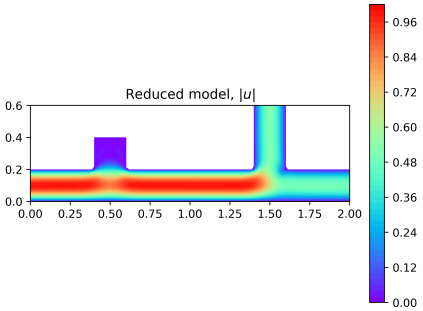

(c) Absolute velocity, ROM.

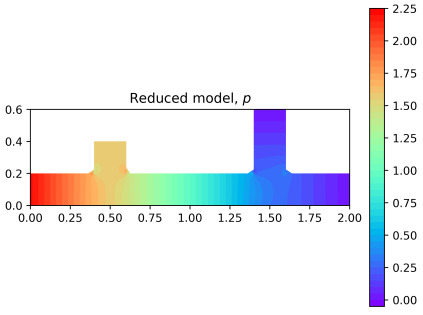

(d) Pressure, ROM.

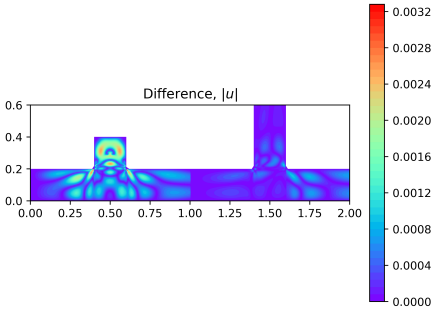

(e) Absolute velocity difference, FOM and ROM.

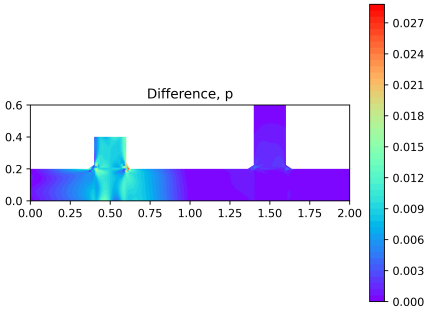

(f) Pressure difference , FOM and ROM.

Figure 37: *Archetype 1 and 2*: Absolute velocity, pressure, and the resulting error from combining the two archetypes.

6.9.3 Archetype 2 and 3

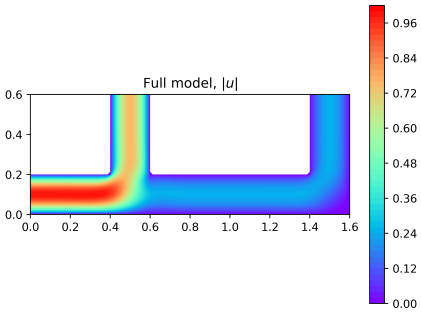

(a) Absolute velocity, FOM.

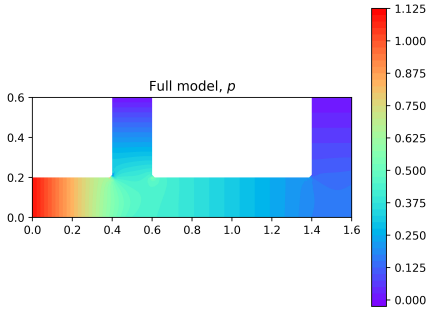

(b) Pressure, FOM.

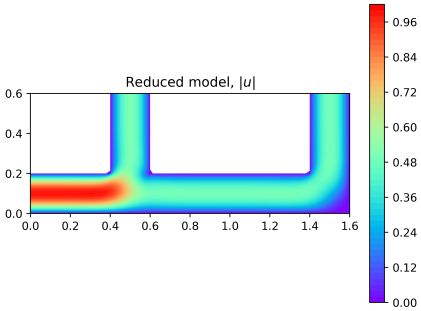

(c) Absolute velocity, ROM.

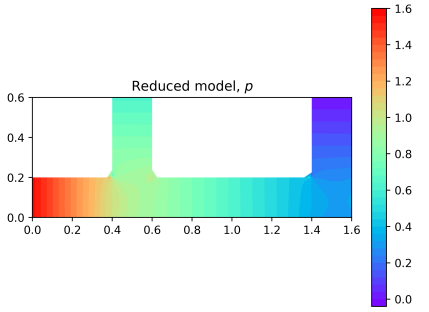

(d) Pressure, ROM.

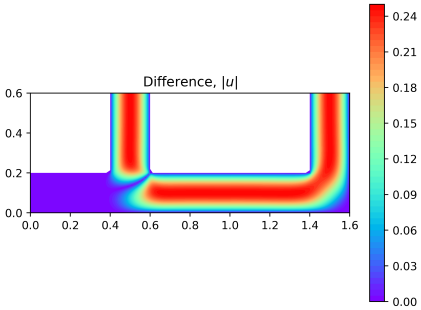

(e) Absolute velocity difference, FOM and ROM.

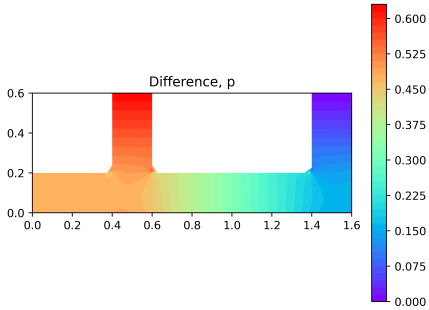

(f) Pressure difference , FOM and ROM.

Figure 38: *Archetype 2 and 3*: Absolute velocity, pressure, and the resulting error from combining the two archetypes.

6.9.4 Archetype 5 and 3

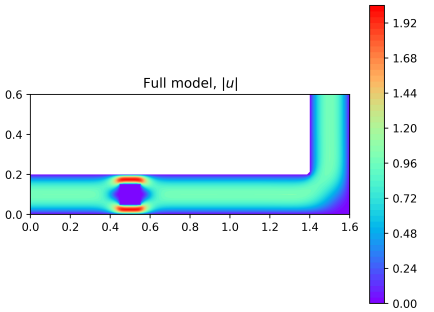

(a) Absolute velocity, FOM.

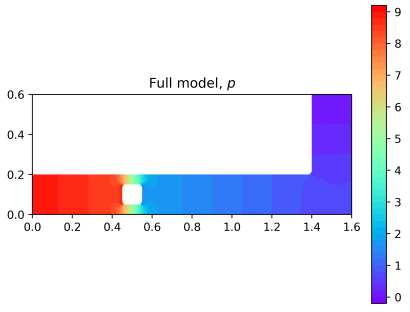

(b) Pressure, FOM.

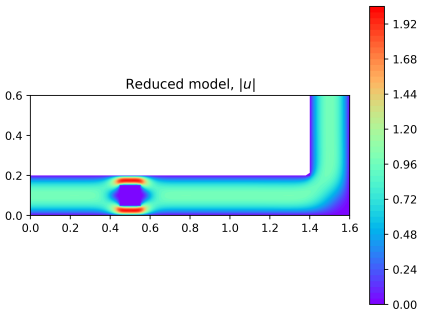

(c) Absolute velocity, ROM.

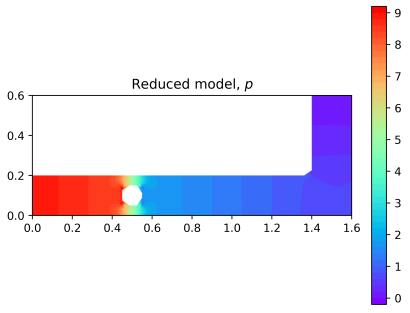

(d) Pressure, ROM.

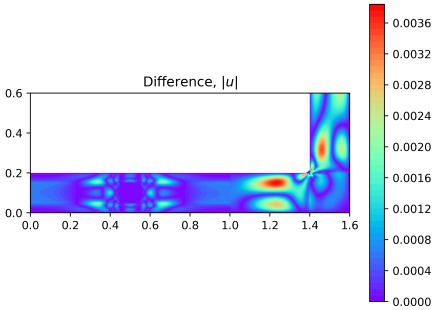

(e) Absolute velocity difference, FOM and ROM.

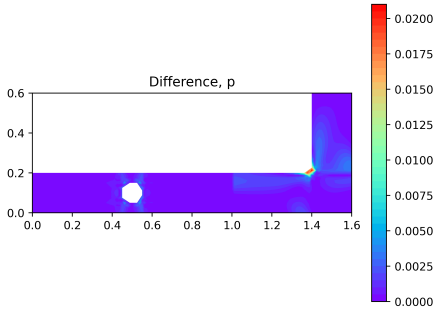

(f) Pressure difference , FOM and ROM.

Figure 39: *Archetype 5 and 3*: Absolute velocity, pressure, and the resulting error from combining the two archetypes.

6.9.5 Archetype 6 and 5

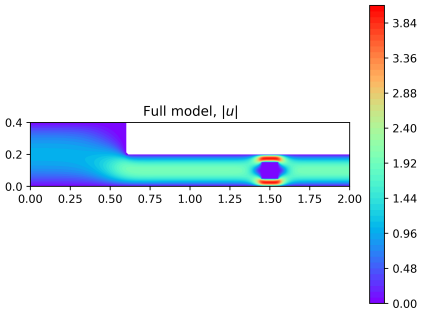

(a) Absolute velocity, FOM.

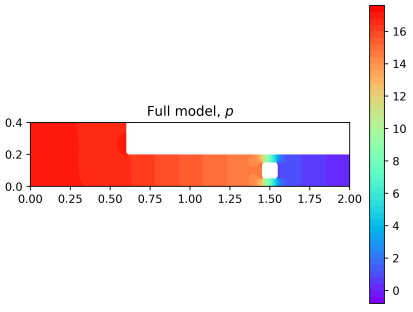

(b) Pressure, FOM.

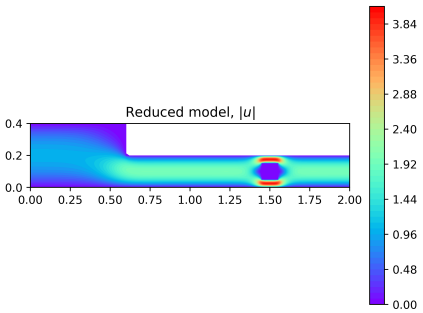

(c) Absolute velocity, ROM.

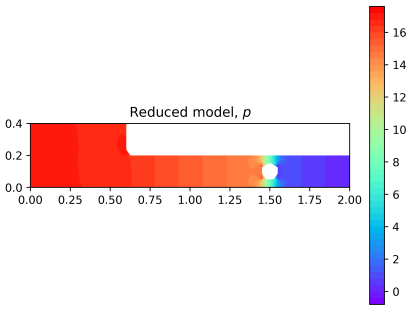

(d) Pressure, ROM.

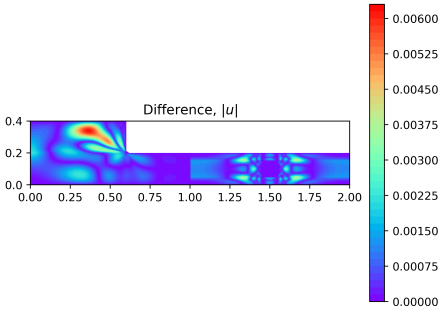

(e) Absolute velocity difference, FOM and ROM.

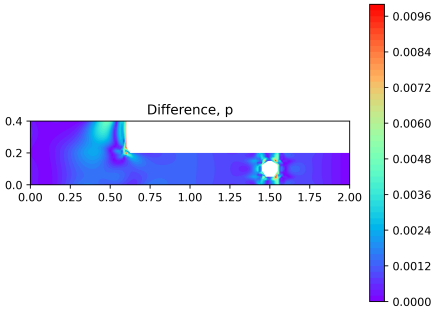

(f) Pressure difference , FOM and ROM.

Figure 40: *Archetype 6 and 5*: Absolute velocity, pressure, and the resulting error from combining the two archetypes.

6.9.6 Noteworthy observations for coupled components

Table 9 shows the relative norms of each archetype with their initial parameters. This is the same table as table 8, but we include it here as well to ease the comparisons. Table 10 shows the relative norms for each of the five combined systems, relative to the *total* FOM equivalent. Given that our approach for connecting the archetypes contributes negligibly to the error, we expect the relative error of the combined archetypes to be somewhere between the relative error for each of its individual components. The dofs of the ROMs were chosen by the POD-algorithm, with $\varepsilon_{\text{POD}} = 10^{-4}$. We will now discuss important observations:

- *Archetype 0 and 1*: From Figure 36 it is clear that almost all the error accumulates in the second archetype, the closed bifurcation. This is to be expected, as the error in velocity and pressure of archetype 0 is seven orders of magnitude smaller than the other archetypes. From the difference figures 36e, 36f we see that there is no visible error in the connection boundary at $x = 1$. Comparing Table 9 and 10, we see that the combined relative error is lower than the individual relative error, both for the x-velocity and the pressure. The error in the y-velocity for the combined model is almost identical to that of archetype 1, since archetype 0 has zero y-velocity.
- *Archetype 1 and 2*: From Sub-figure 37e we see that our method of connecting the archetypes actually improves the error plot, as the correct parabolar velocity shape is enforced through this method. From table 8 and 10, we see that all of the relative norms of the combined model lie in between the relative norms of the individual components.
- *Archetype 2 and 3*: This archetype pair illustrates why our method fails for the pipe with two outlets. From Figure 38 we can clearly see how the dominant flow in the FOM occurs in the first bifurcation, but in the ROM the volume flow is equal in both pipes. Comparing the pressures, it is clear that the outlet pressure of the first bifurcation in the ROM is higher than in the FOM. Our method has no way of retroactively changing the pressure gradient of the previous archetype, thus we omit archetype 2 from further systems. Table 10 also show how much the ROM solution deviates from the FOM solution.
- *Archetype 5 and 3*: Sub-figure 39f shows how most of the pressure error accumulates in the corner of archetype 3. Comparing table 9 and 10, we see that the relative error of the combined archetypes lies in between the relative error of the individual archetypes for the x-velocity and the pressure. However for the y-velocity, the combined archetypes have a higher relative norm than both of its individual components. This is probably due to the inlet of archetype 3 being too short for the one-dimensional inlet-velocity assumption to hold. By studying Sub-figure 39e we see that there is some error at the connection boundary at $x = 1$, further implying that the inlet of archetype 3 is too short in this case.
- *Archetype 6 and 5*: Figure 40 shows once again how the error accumulates around the corner of the archetypes. Tables 9 and 10 show how the relative velocity errors of the combined model lie in between the relative velocity error of each individual archetype. However, somehow the relative pressure error is lower for the combined model than the relative pressure error of its components.

Archetype:	$\frac{\lvert u_x - u_{x,r}\rvert_{H^1}}{\lvert u_x\rvert_{H^1}}$	$\frac{\lvert u_y - u_{y,r}\rvert_{H^1}}{\lvert u_y\rvert_{H^1}}$	$\frac{\lvert\lvert p - p_r\rvert\rvert_{L^2}}{\lvert\lvert p\rvert\rvert_{L^2}}$
Ω_0	$1.57 \cdot 10^{-9}$	—	$5.84 \cdot 10^{-11}$
Ω_1	$3.29 \cdot 10^{-3}$	$3.65 \cdot 10^{-2}$	$9.76 \cdot 10^{-3}$
Ω_2	$1.04 \cdot 10^{-3}$	$3.46 \cdot 10^{-3}$	$1.74 \cdot 10^{-3}$
Ω_3	$3.75 \cdot 10^{-3}$	$6.99 \cdot 10^{-3}$	$2.50 \cdot 10^{-3}$
Ω_4	$3.75 \cdot 10^{-3}$	$6.99 \cdot 10^{-3}$	$2.50 \cdot 10^{-3}$
Ω_5	$1.12 \cdot 10^{-3}$	$3.94 \cdot 10^{-3}$	$1.31 \cdot 10^{-4}$
Ω_6	$3.06 \cdot 10^{-3}$	$1.56 \cdot 10^{-2}$	$1.01 \cdot 10^{-3}$
Ω_7	$8.44 \cdot 10^{-4}$	$7.36 \cdot 10^{-3}$	$6.25 \cdot 10^{-4}$

Table 9: Relative norms between the FOM and the ROM of all the archetypes, for their initial parameters. The dofs of the ROM were chosen with the POD algorithm.

Archetypes:	$\frac{\lvert u_x - u_{x,r}\rvert_{H^1}}{\lvert u_x\rvert_{H^1}}$	$\frac{\lvert u_y - u_{y,r}\rvert_{H^1}}{\lvert u_y\rvert_{H^1}}$	$\frac{\lvert\lvert p - p_r\rvert\rvert_{L^2}}{\lvert\lvert p\rvert\rvert_{L^2}}$
$\Omega_0 \cup \Omega_1$	$3.07 \cdot 10^{-3}$	$3.64 \cdot 10^{-2}$	$3.61 \cdot 10^{-3}$
$\Omega_1 \cup \Omega_2$	$3.61 \cdot 10^{-3}$	$1.15 \cdot 10^{-2}$	$4.20 \cdot 10^{-3}$
$\Omega_2 \cup \Omega_3$	$3.33 \cdot 10^{-1}$	$4.43 \cdot 10^{-1}$	$8.88 \cdot 10^{-1}$
$\Omega_5 \cup \Omega_3$	$2.07 \cdot 10^{-3}$	$5.77 \cdot 10^{-2}$	$3.08 \cdot 10^{-4}$
$\Omega_6 \cup \Omega_5$	$1.66 \cdot 10^{-3}$	$5.13 \cdot 10^{-3}$	$1.03 \cdot 10^{-4}$

Table 10: Relative norms of some of the archetype pairs, compared to the single domain, FOM equivalent, for their initial parameters. The dofs of the ROM were chosen with the POD algorithm.

6.10 Full system examples

In this section we show three examples of how the archetypes can be connected to create a complete system. We omit the use of archetype 2, due to the previously mentioned issues the bifurcation causes. We also measure the volume inflow and outflow of each system, to calculate the relative error in the volume flow of the system. The connection boundaries between each archetype are indicated by dashed lines in the velocity figures. We've added contour lines for the pressure figures to better illustrate where the pressure gradient is the steepest. Unfortunately calculating the norm of a complete FOM proved to be very difficult, as the combined domains get very complex as more archetypes are added. Thus we only compare the in-flux of the system to the out-flux of the system. Note that the inlet of each system is located at $(x, y) = (0, 0)$.

6.10.1 $\mathcal{A}_1$ – The first system

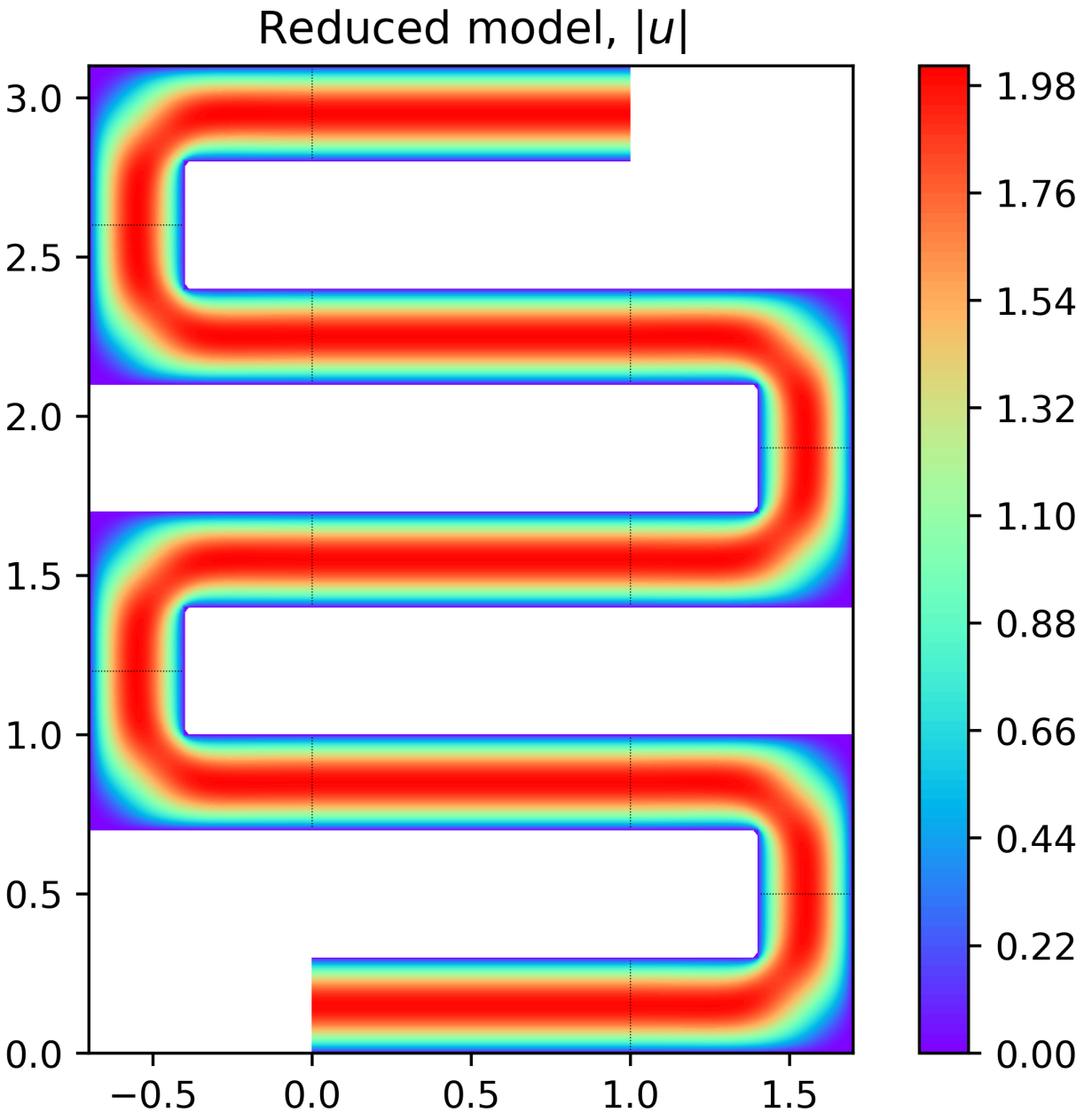

Figure 41: *The first system* : Absolute velocity of a complete system created from archetypes 0, 3 and 4. The dotted lines marks the intersections between the archetypes.

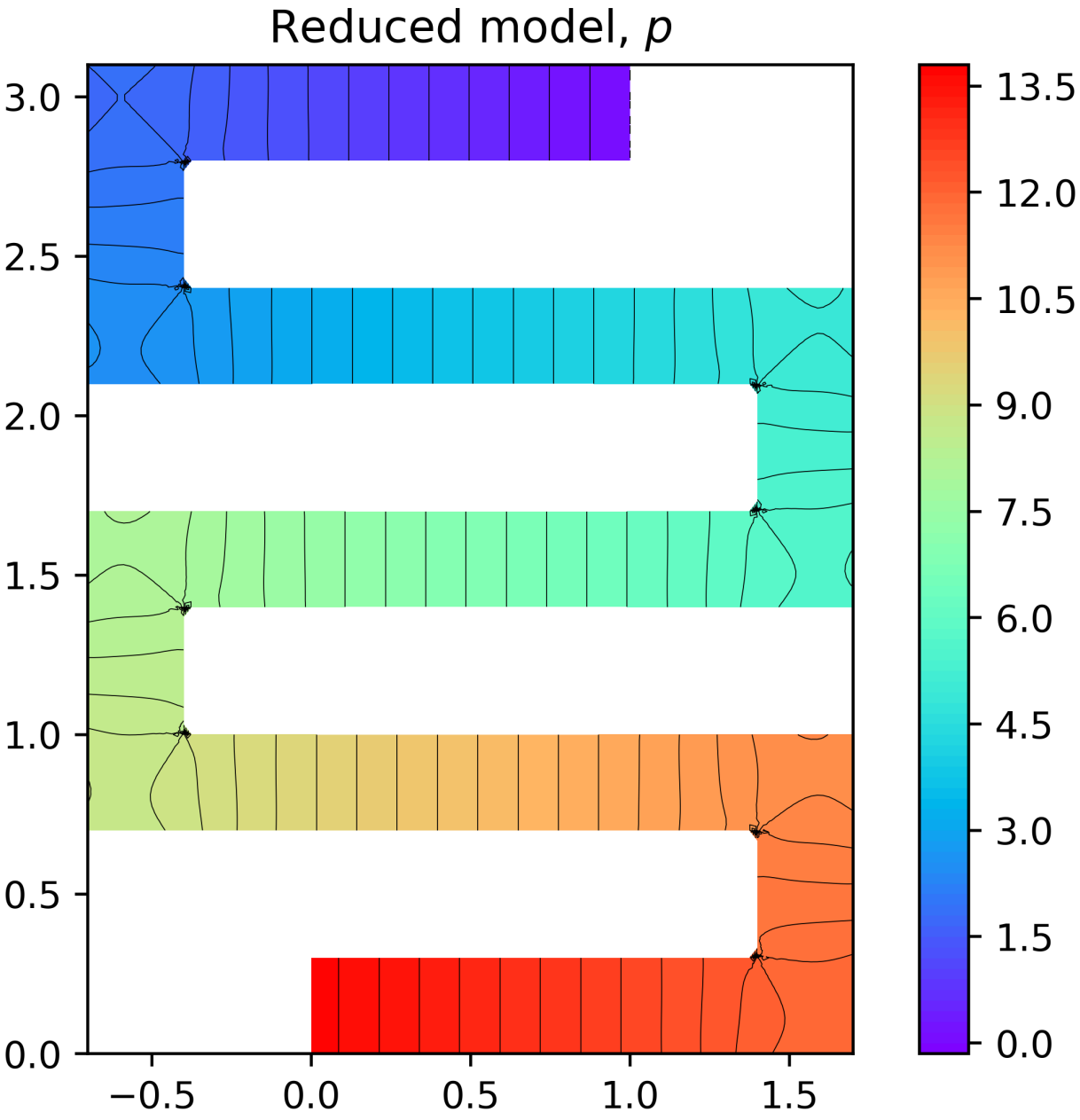

Figure 42: *The first system* : Pressure of a complete system created from archetypes 0, 3 and 4.

6.10.2 $\mathcal{A}_2$ – The second system

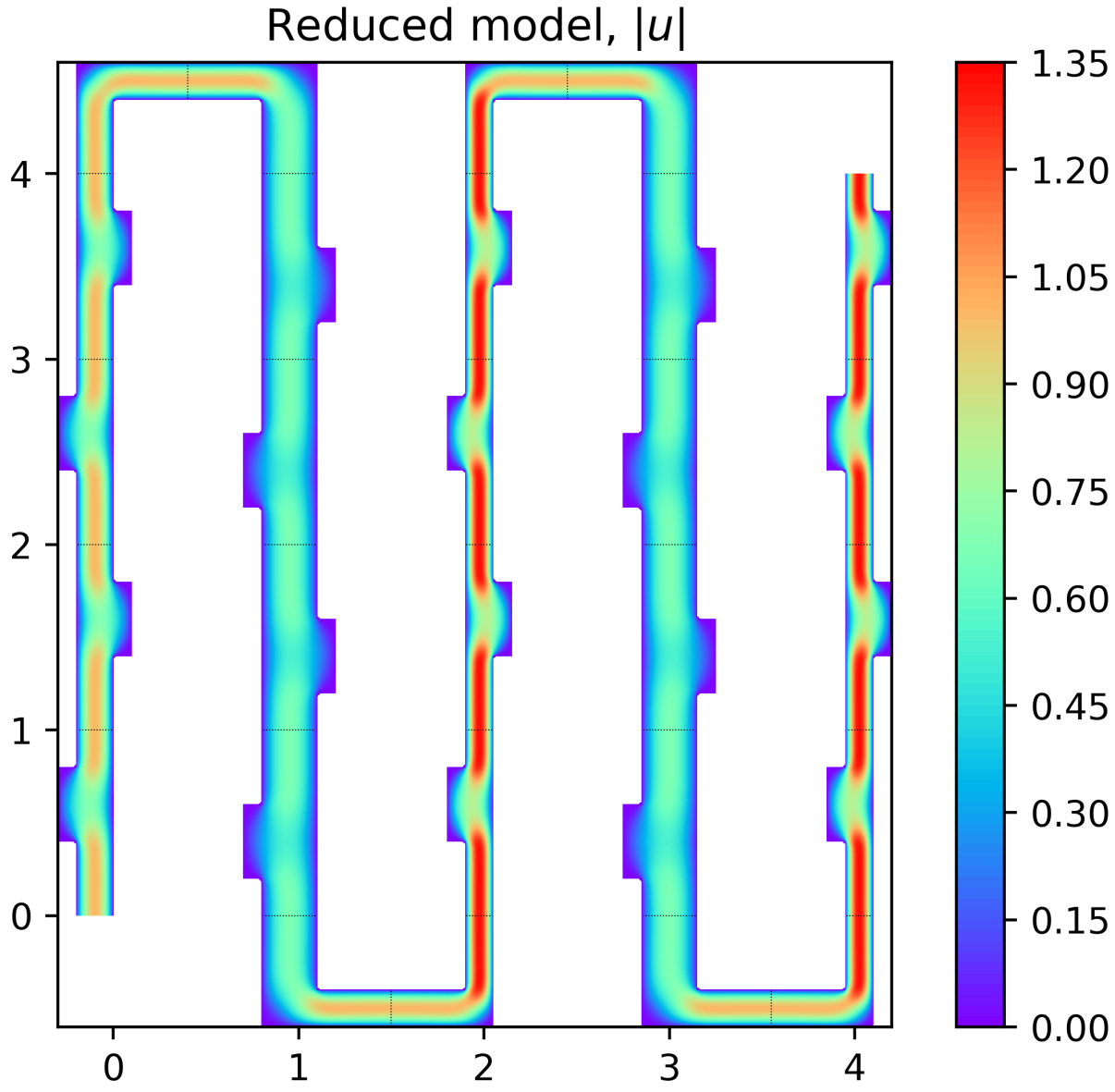

Figure 43: *The second system* : Absolute velocity of a complete system created from archetypes 1, 3 and 4. The dotted lines marks the intersections between the archetypes.

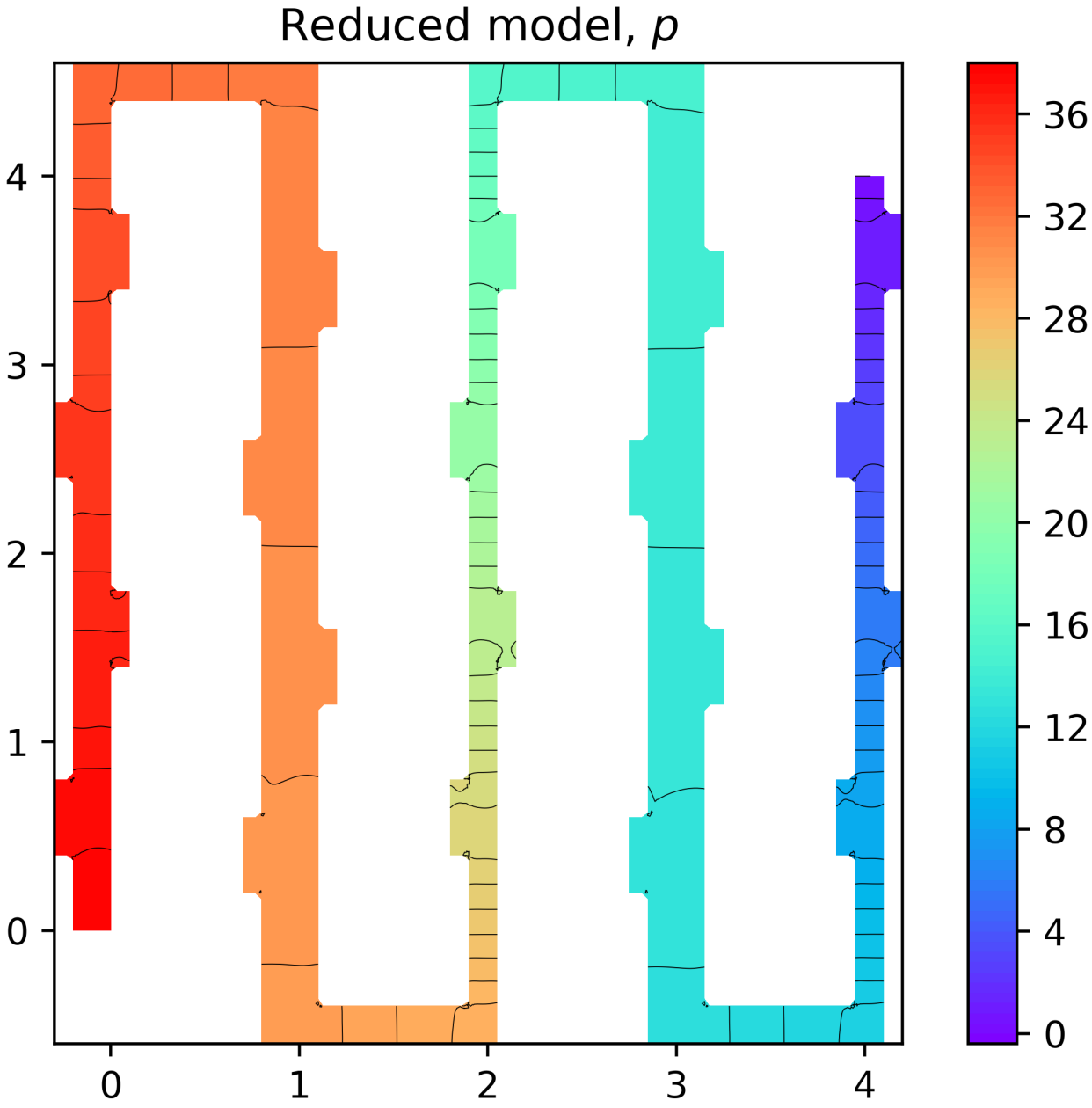

Figure 44: *The second system* : Pressure of a complete system created from archetypes 1, 3 and 4.

6.10.3 $\mathcal{A}_3$ – The third system

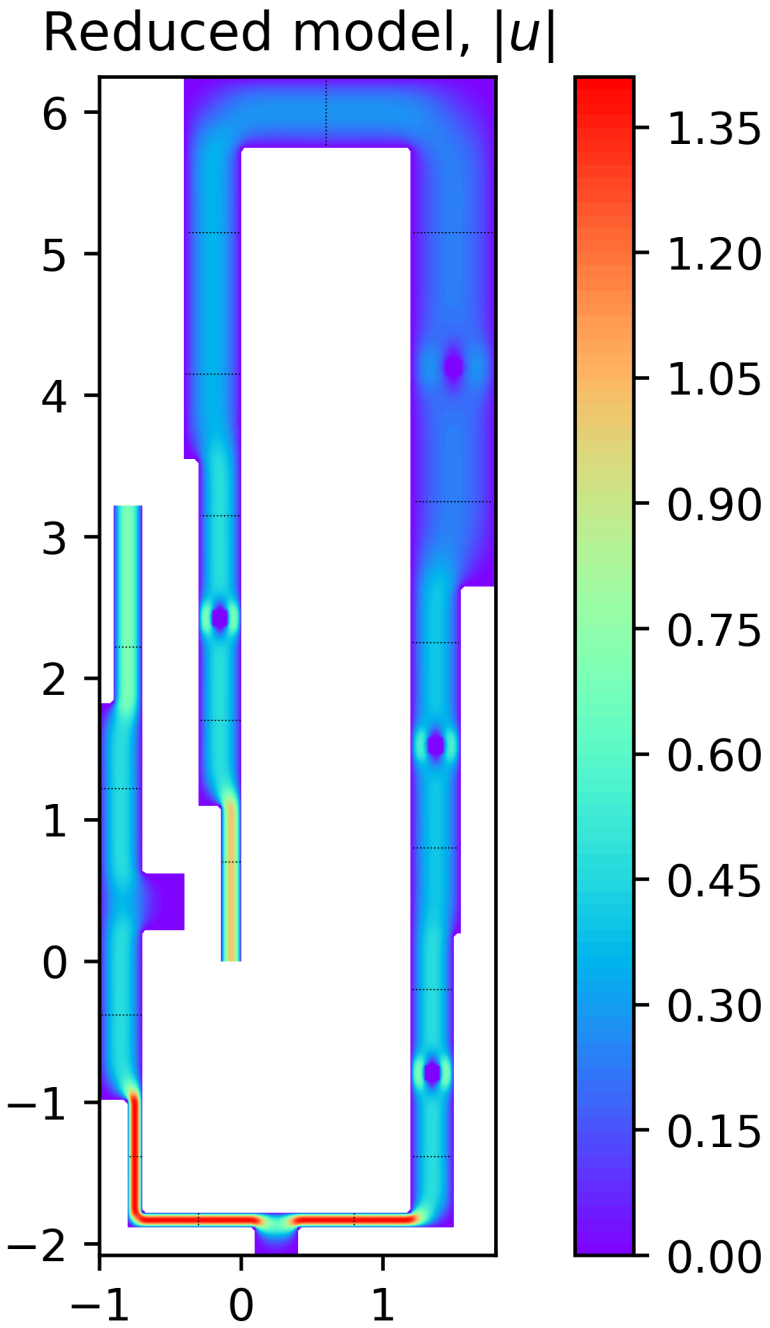

Figure 45: *The third system* : Absolute velocity of a complete system created from archetypes 0, 1, 3, 4, 5, 6 and 7. The dotted lines marks the intersections between the archetypes.

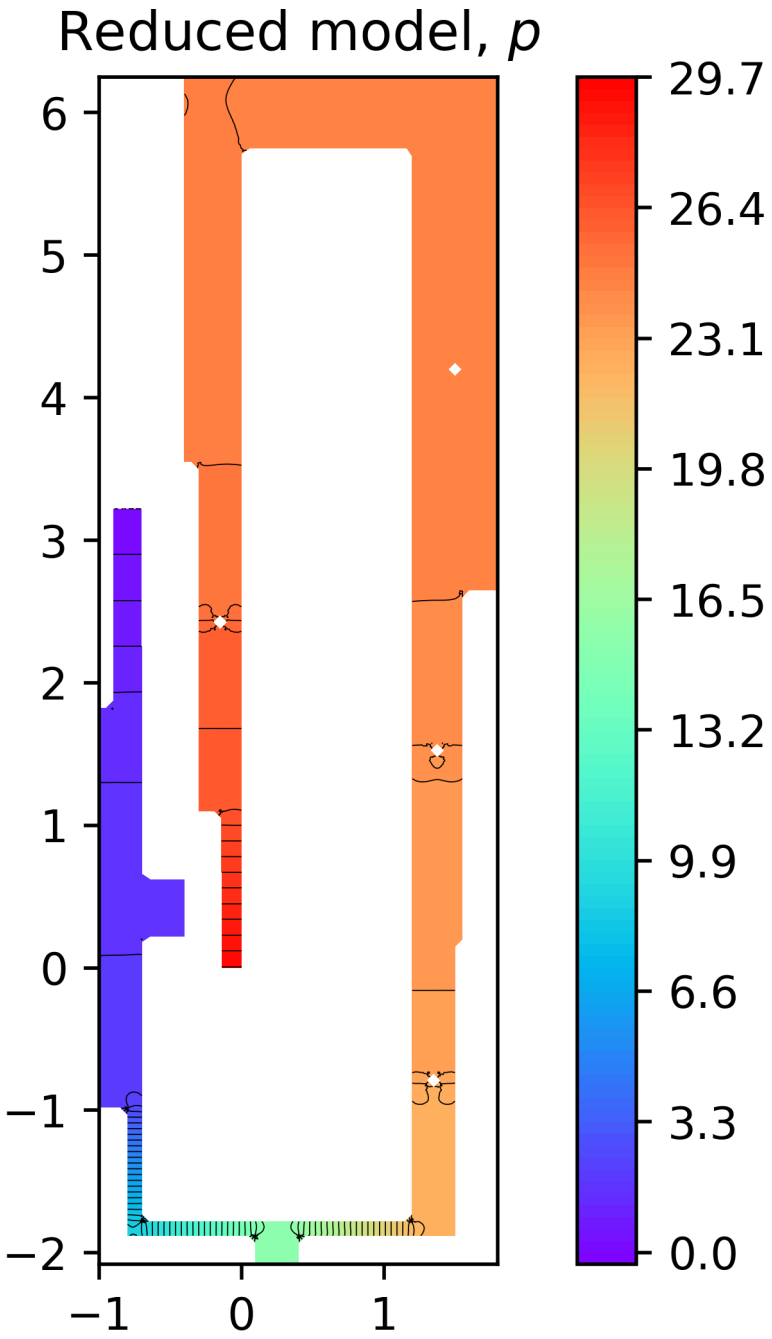

Figure 46: *The third system* : Pressure of a complete system created from archetypes 0, 1, 3, 4, 5, 6 and 7.

System:	Total components:	Time elapsed:	V_{in}	V_{out}	$\left\lvert\frac{V_{\text{in}} - V_{\text{out}}}{V_{\text{in}}}\right\rvert$
$\mathcal{A}_1$	13	$0.712s$	0.4	0.40153	$3.82 \cdot 10^{-3}$
$\mathcal{A}_2$	28	$1.893s$	0.13333	0.13349	$1.19 \cdot 10^{-3}$
$\mathcal{A}_3$	19	$1.402s$	0.09333	0.09339	$6.17 \cdot 10^{-4}$

Table 11: Computational details from the three example systems, as well as volume inflow, outflow, and relative volume flow error.

7 Conclusions

Through this thesis we have investigated component-based Reduced Order Model (ROM) to model the Stokes equation in an arbitrary system of pipes. The pipe-systems were created by combining predefined archetypes, where the geometry of each archetype could be altered by changing some geometrical parameters. Component-based ROM shows great promise when dealing with such large-structure problems where it is necessary to solve the system multiple times for different parameter values.

Breaking the problem into smaller sub-problems and solving them individually does reduce a lot of the complexity, while the ROM significantly improves the time spent both setting up and solving the individual problems. For the Stokes equation, this component-based approach proved to be very effective, although with some noteworthy drawbacks. In cases where the system had multiple outlets, both the pressure and the velocity of the Component-based ROM did not match its single domain, Full Order Model (FOM) equivalent. This could possibly be solved with some special boundary conditions allowing us to alter the pressure gradient when needed. For flow in a pipe-system with a singular inlet and outlet however, the results were satisfactory. For each individual component, the linear system were solved $300 - 1000$ times faster with the ROM than the FOM, with a typical relative error between the FOM and the ROM of 10^{-3}.

For the full pipe-systems, the relative difference in the inlet and outlet volume flow were found to be below 0.5%, even for the larger systems of multiple components. A completely new system could be generated in ~ 1 second, where an equivalent Full Order Model (FOM) with $\sim 10^5$ dofs would take ~ 300 seconds to compute. Thus we conclude that this approach, with some alteration to better handle bifurcations, definitely could be viable to model and monitor a wide range of pipe-systems.

References

[1] M. Salman Siddiqui, Trond Kvamsdal, and Adil Rasheed. "High Fidelity Computational Fluid Dynamics Assessment of Wind Tunnel Turbine Test". In: *Journal of Physics: Conference Series* 1356 (2019), p. 012044. DOI: 10.1088/1742-6596/1356/1/012044. URL: http://dx.doi.org/10.1088/1742-6596/1356/1/012044.

[2] M. Salman Siddiqui et al. "Finite-Volume High-Fidelity Simulation Combined with Finite-Element-Based Reduced-Order Modeling of Incompressible Flow Problems". In: *Energies* 12.7 (2019). ISSN: 1996-1073. DOI: 10.3390/en12071271.

[3] Alfio Quarteroni, Andrea Manzoni, and Federico Negri. *Reduced Basis Methods for Partial Differential Equations*. Springer International Publishing, 2016. DOI: 10.1007/978-3-319-15431-2.

[4] Shasha Xiao et al. "A reduced-order approach to analyze stability of genetic regulatory networks with discrete time delays". In: *Neurocomputing* 323 (2019), pp. 311–318. ISSN: 0925-2312. DOI: https://doi.org/10.1016/j.neucom.2018.10.005.

[5] Mandar Tabib et al. "A full-scale 3D Vs 2.5D Vs 2D analysis of flow pattern and forces for an industrial-scale 5MW NREL reference wind-turbine." In: *Energy Procedia* 137 (2017). 14th Deep Sea Offshore Wind R&D Conference, EERA DeepWind'2017, pp. 477–486. ISSN: 1876-6102. DOI: https://doi.org/10.1016/j.egypro.2017.10.372.

[6] Qian Wang, Nicolò Ripamonti, and Jan S. Hesthaven. "Recurrent neural network closure of parametric POD-Galerkin reduced-order models based on the Mori-Zwanzig formalism". In: *Journal of Computational Physics* 410 (2020), p. 109402. ISSN: 0021-9991. DOI: https://doi.org/10.1016/j.jcp.2020.109402.

[7] Suraj Pawar et al. "Model fusion with physics-guided machine learning: Projection-based reduced-order modeling". In: *Physics of Fluids* 33.6 (2021), p. 067123. DOI: 10.1063/5.0053349.

[8] Hui Wang, Zhenshan Li, and Ningsheng Cai. "Reduced-order model for redox kinetics of oxygen carrier in chemical looping combustion". In: *Proceedings of the Combustion Institute* (2020). ISSN: 1540-7489. DOI: https://doi.org/10.1016/j.proci.2020.08.002.

[9] A. Rasheed, O. San, and T. Kvamsdal. "Digital Twin: Values, Challenges and Enablers From a Modeling Perspective". In: *IEEE Access* 8 (2020), pp. 21980–22012. DOI: 10.1109/ACCESS.2020.2970143.

[10] Omer San, Adil Rasheed, and Trond Kvamsdal. "Hybrid analysis and modeling, eclecticism, and multifidelity computing toward digital twin revolution". In: *GAMM-Mitteilungen* 44.2 (2021), e202100007. DOI: https://doi.org/10.1002/gamm.202100007. eprint: https://onlinelibrary.wiley.com/doi/pdf/10.1002/gamm.202100007.

[11] Francisco Chinesta et al. "Virtual, Digital and Hybrid Twins: A New Paradigm in Data-Based Engineering and Engineered Data". In: *Archives of Computational Methods in Engineering* 27 (Nov. 2018). DOI: 10.1007/s11831-018-9301-4.

[12] Adil Rasheed, Omer San, and Trond Kvamsdal. "Digital Twin: Values, Challenges and Enablers From a Modeling Perspective". In: *IEEE Access* 8 (2020), pp. 21980–22012. DOI: 10.1109/access.2020.2970143.

[13] M.G. Kapteyn et al. "Data-driven physics-based digital twins via a library of component-based reduced-order models". In: *International Journal for Numerical Methods in Engineering* (2020). DOI: https://doi.org/10.1002/nme.6423.

[14] E Fonn et al. "Fast divergence-conforming reduced basis methods for stationary and transient flow problems". In: *Journal of Physics: Conference Series* 1669 (2020), p. 012031. DOI: 10.1088/1742-6596/1669/1/012031.

[15] Eivind Fonn et al. "Fast divergence-conforming reduced basis methods for steady Navier–Stokes flow". In: *Computer Methods in Applied Mechanics and Engineering* 346 (2019), pp. 486–512. ISSN: 0045-7825. DOI: https://doi.org/10.1016/j.cma.2018.11.038.

[16] M. Salman Siddiqui, Adil Rasheed, and Trond Kvamsdal. "Numerical assessment of RANS turbulence models for the development of data driven Reduced Order Models". In: *Ocean Engineering* 196 (2020), p. 106799. ISSN: 0029-8018. DOI: https://doi.org/10.1016/j.oceaneng.2019.106799.

[17] M. Salman Siddiqui, Adil Rasheed, and Trond Kvamsdal. "Validation of the numerical simulations of flow around a scaled-down turbine using experimental data from wind tunnel". In: *Wind and Structures* 29.6 (2019), pp. 405–416. DOI: 10.12989/WAS.2019.29.6.405.

[18] David Borthwick. "Function Spaces". In: *Introduction to Partial Differential Equations*. Cham: Springer International Publishing, 2016, pp. 111–130. ISBN: 978-3-319-48936-0. DOI: 10.1007/978-3-319-48936-0_7.

[19] Christopher Heil. "Norms and Banach Spaces". In: *Metrics, Norms, Inner Products, and Operator Theory*. Cham: Springer International Publishing, 2018, pp. 115–117. ISBN: 978-3-319-65322-8. DOI: 10.1007/978-3-319-65322-8_3.

[20] Christopher Heil. "Inner Products and Hilbert Spaces". In: *Metrics, Norms, Inner Products, and Operator Theory*. Cham: Springer International Publishing, 2018, p. 191. ISBN: 978-3-319-65322-8. DOI: 10.1007/978-3-319-65322-8_5.

[21] Alfio Quarteroni. *Numerical Models for Differential Problems*. Springer Milan, 2014. DOI: 10.1007/978-88-470-5522-3.

[22] Susanne C. Brenner and L. Ridgway Scott. *The Mathematical Theory of Finite Element Methods*. Springer New York, 2008. DOI: 10.1007/978-0-387-75934-0.

[23] David Borthwick. "Weak Solutions". In: *Introduction to Partial Differential Equations*. Cham: Springer International Publishing, 2016, pp. 177–204. ISBN: 978-3-319-48936-0. DOI: 10.1007/978-3-319-48936-0_10.

[24] "Chapter 2 - Introduction to the Finite Element Method". In: *The Finite Element Method for Elliptic Problems*. Ed. by Philippe G. Ciarlet. Vol. 4. Studies in Mathematics and Its Applications. Elsevier, 1978, pp. 36–109. DOI: https://doi.org/10.1016/S0168-2024(08)70181-4.

[25] Alfio Quarteroni, Andrea Manzoni, and Federico Negri. "RB Methods: Basic Principles, Basic Properties". In: *Reduced Basis Methods for Partial Differential Equations: An Introduction*. Cham: Springer International Publishing, 2016, pp. 39–72. ISBN: 978-3-319-15431-2. DOI: 10.1007/978-3-319-15431-2_3.

[26] "Chapter 1 - Reduced-Order Extrapolation Finite Difference Schemes Based on Proper Orthogonal Decomposition". In: *Proper Orthogonal Decomposition Methods for Partial Differential Equations*. Ed. by Goong Chen, Zhendong Luo, and Goong Chen. Mathematics in Science and Engineering. Academic Press, 2019, pp. 1–56. ISBN: 978-0-12-816798-4. DOI: https://doi.org/10.1016/B978-0-12-816798-4.00006-1.

[27] Alfio Quarteroni. "Reduced basis approximation for parametrized partial differential equations". In: *Numerical Models for Differential Problems*. Cham: Springer International Publishing, 2017, pp. 613–661. ISBN: 978-3-319-49316-9. DOI: 10.1007/978-3-319-49316-9_20.

[28] Alfio Quarteroni, Andrea Manzoni, and Federico Negri. "Construction of RB Spaces by SVD-POD". In: *Reduced Basis Methods for Partial Differential Equations: An Introduction*. Cham: Springer International Publishing, 2016, pp. 115–140. ISBN: 978-3-319-15431-2. DOI: 10.1007/978-3-319-15431-2_6.

[29] "Singular Value Decomposition". In: *Encyclopedia of Social Network Analysis and Mining*. Ed. by Reda Alhajj and Jon Rokne. New York, NY: Springer New York, 2014, pp. 1749–1749. ISBN: 978-1-4614-6170-8. DOI: 10.1007/978-1-4614-6170-8_100696.

[30] Elizabeth H. Krath et al. "An efficient proper orthogonal decomposition based reduced-order model for compressible flows". In: *Journal of Computational Physics* 426 (2021), p. 109959. ISSN: 0021-9991. DOI: https://doi.org/10.1016/j.jcp.2020.109959.

[31] Jens L. Eftang, Martin A. Grepl, and Anthony T. Patera. "A posteriori error bounds for the empirical interpolation method". In: *Comptes Rendus Mathematique* 348.9 (2010), pp. 575–579. ISSN: 1631-073X. DOI: https://doi.org/10.1016/j.crma.2010.03.004.

[32] M. Siddiqui et al. "Finite-Volume High-Fidelity Simulation Combined with Finite-Element-Based Reduced Order Modeling of Incompressible Flow Problems". In: *Energies* 12.7 (2019), p. 1271. ISSN: 1996-1073. DOI: 10.3390/en12071271.

[33] Kjetil André Johannessen, Mukesh Kumar, and Trond Kvamsdal. "Divergence-conforming discretization for Stokes problem on locally refined meshes using LR B-splines". In: *Computer Methods in Applied Mechanics and Engineering* 293 (2015), pp. 38–70. ISSN: 0045-7825. DOI: https://doi.org/10.1016/j.cma.2015.03.028.

[34] A. Buffa, C. de Falco, and G. Sangalli. "IsoGeometric Analysis: Stable elements for the 2D Stokes equation". In: *International Journal for Numerical Methods in Fluids* 65.11-12 (2011), pp. 1407–1422. DOI: https://doi.org/10.1002/fld.2337.

[35] Rolf Stenberg. "Analysis of mixed finite element methods for the stokes problem: A unified approach". In: *Mathematics of Computation - Math. Comput.* 42 (Jan. 1984), pp. 9–9. DOI: 10.1090/S0025-5718-1984-0725982-9.

[36] Abdullah Abdulhaque. "Isogeometric analysis of Poisson's and Stokes' equations using B-splines". In: (2016). Specialization project at NTNU, 2016, Department of Mathematical Sciences.

[37] Daniele Boffi, Franco Brezzi, and Michel Fortin. *Mixed Finite Element Methods and Applications*. Springer Berlin Heidelberg, 2013. DOI: 10.1007/978-3-642-36519-5.

[38] Gabriel R Barrenechea and Andreas Wachtel. "The inf-sup stability of the lowest order Taylor–Hood pair on affine anisotropic meshes". In: *IMA Journal of Numerical Analysis* 40.4 (2019), pp. 2377–2398. DOI: 10.1093/imanum/drz028.

[39] Alf Emil Løvgren. "Reduced basis modeling of hierarchical flow systems". In: (2005). Doctoral thesis at NTNU, 2005:212, Department of Mathematical Sciences.

[40] Sylvain Vallaghé et al. "Component-based reduced basis for parametrized symmetric eigenproblems". In: *Advanced Modeling and Simulation in Engineering Sciences* 2.1 (2015). DOI: 10.1186/s40323-015-0021-0.

[41] Jens L. Eftang, Anthony T. Patera, and Einar M. Rønquist. "An "hp" Certified Reduced Basis Method for Parametrized Elliptic Partial Differential Equations". In: *SIAM Journal on Scientific Computing* 32.6 (2010), pp. 3170–3200. DOI: 10.1137/090780122.

[42] Jens L. Eftang, David J. Knezevic, and Anthony T. Patera. "An hp certified reduced basis method for parametrized parabolic partial differential equations". In: *Mathematical and Computer Modelling of Dynamical Systems* 17.4 (2011), pp. 395–422. DOI: 10.1080/13873954.2011.547670.

[43] Jens L. Eftang and Anthony T. Patera. "Port reduction in parametrized component static condensation: approximation and a posteriori error estimation". In: *International Journal for Numerical Methods in Engineering* 96.5 (2013), pp. 269–302. DOI: https://doi.org/10.1002/nme.4543.

[44] Jens L Eftang and Anthony T Patera. "A port-reduced static condensation reduced basis element method for large component-synthesized structures: approximation and A Posteriori error estimation". In: *Advanced Modeling and Simulation in Engineering Sciences* 1.1 (2014), p. 3. DOI: 10.1186/2213-7467-1-3.

[45] JL Eftang et al. "Adaptive Port Reduction in Static Condensation". In: *IFAC Proceedings Volumes* 45.2 (2012). 7th Vienna International Conference on Mathematical Modelling, pp. 695–699. ISSN: 1474-6670. DOI: https://doi.org/10.3182/20120215-3-AT-3016.00123.

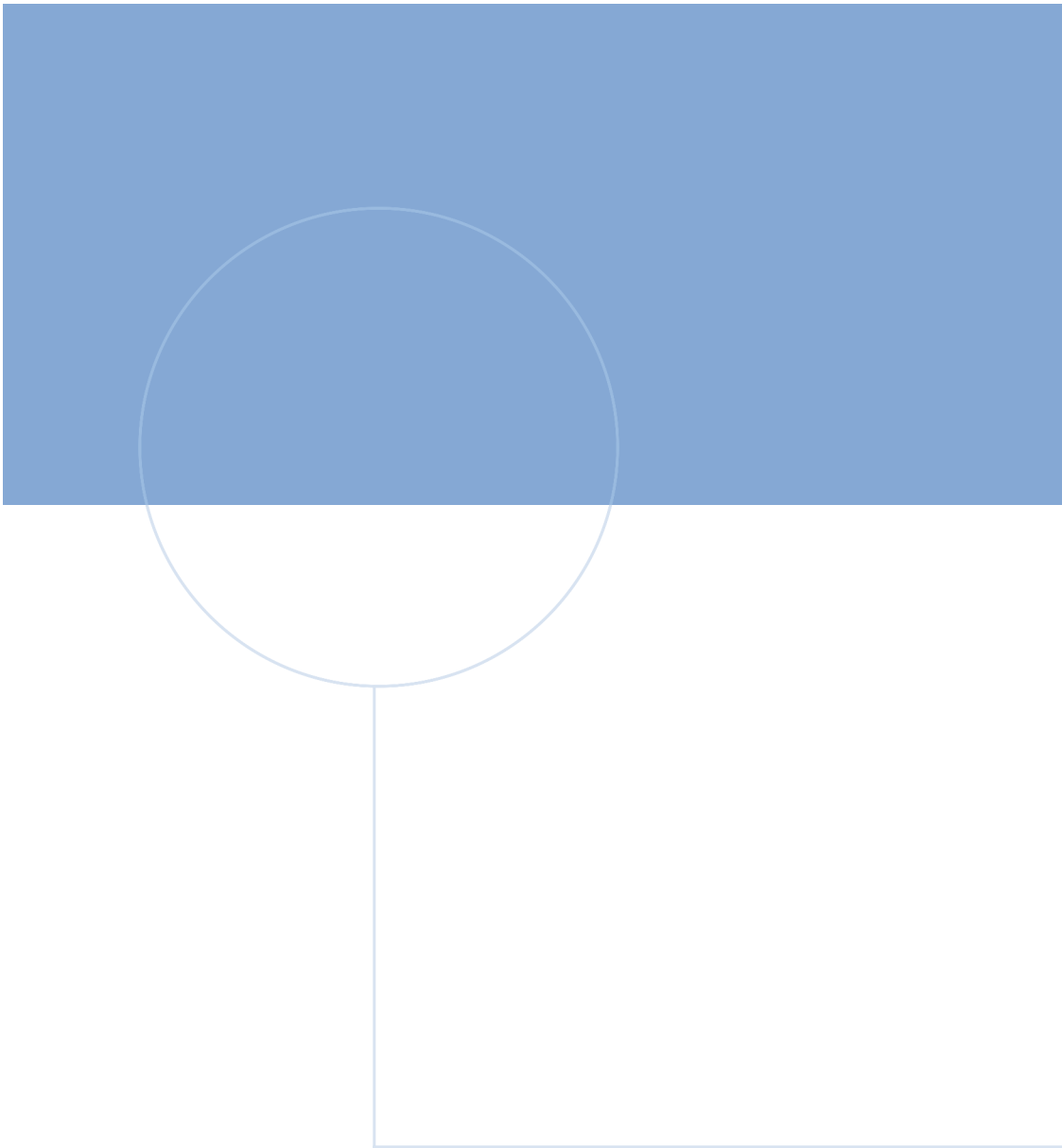

NTNU

Norwegian University of
Science and Technology